

EDITORIAL BOARD

Editor-in-Chief

I.V. Krivtsun E.O. Paton Electric Welding Institute, Kyiv, Ukraine

Deputy Editor-in-Chief

S.V. Akhonin E.O. Paton Electric Welding Institute, Kyiv, Ukraine

Deputy Editor-in-Chief

L.M. Lobanov E.O. Paton Electric Welding Institute, Kyiv, Ukraine

Editorial Board Members

O.M. Berdnikova E.O. Paton Electric Welding Institute, Kyiv, Ukraine
Chang Yunlong School of Materials Science and Engineering,
Shenyang University of Technology, Shenyang, China
V.V. Dmitrik NTUU «Kharkiv Polytechnic Institute», Kharkiv, Ukraine
Dong Chunlin China-Ukraine Institute of Welding of Guangdong Academy of Sciences, Guangzhou, China
A. Gumenyuk Bundesanstalt für Materialforschung und –prüfung (BAM), Berlin, Germany
V.V. Knysh E.O. Paton Electric Welding Institute, Kyiv, Ukraine
V.M. Korzhyk E.O. Paton Electric Welding Institute, Kyiv, Ukraine
V.V. Kvasnytskyi NTUU «Igor Sikorsky Kyiv Polytechnic Institute», Kyiv, Ukraine
Yu.M. Lankin E.O. Paton Electric Welding Institute, Kyiv, Ukraine
S.Yu. Maksymov E.O. Paton Electric Welding Institute, Kyiv, Ukraine
M.O. Pashchin E.O. Paton Electric Welding Institute, Kyiv, Ukraine
Ya. Pilarczyk Welding Institute, Gliwice, Poland
V.D. Poznyakov E.O. Paton Electric Welding Institute, Kyiv, Ukraine
U. Reisgen Welding and Joining Institute, Aachen, Germany
I.O. Ryabtsev E.O. Paton Electric Welding Institute, Kyiv, Ukraine
V.M. Uchanin Karpenko Physico-Mechanical Institute, Lviv, Ukraine
Yang Yongqiang South China University of Technology, Guangzhou, China

Managing Editor

O.T. Zelnichenko International Association «Welding», Kyiv, Ukraine

Address of Editorial Board

E.O. Paton Electric Welding Institute, 11 Kazymyr Malevych Str. (former Bozhenko), 03150, Kyiv, Ukraine
Tel./Fax: (38044) 200 82 77, E-mail: journal@paton.kiev.ua
<https://patonpublishinghouse.com/eng/journals/tpwj>

State Registration Certificate 24933-14873 ПП from 13.08.2021

ISSN 0957-798X, DOI: <http://dx.doi.org/10.37434/tpwj>

Subscriptions, 12 issues per year:

\$384 — annual subscription for the printed (hard copy) version, air postage and packaging included;

\$312 — annual subscription for the electronic version

(sending issues in pdf format or providing access to IP addresses).

The content of the journal includes articles received from authors from around the world in the field of welding, metallurgy, material science and selectively includes translations into English of articles from the following journals, published by PWI in Ukrainian:

- Automatic Welding (<https://patonpublishinghouse.com/eng/journals/as>);
- Technical Diagnostics & Nondestructive Testing (<https://patonpublishinghouse.com/eng/journals/tdnk>);
- Electrometallurgy Today (<https://patonpublishinghouse.com/eng/journals/sem>).

CONTENTS

ORIGINAL ARTICLES

M.G. Korab, M.V. Iurzhenko, A.V. Vashchuk, I.K. Senchenkov MODELING OF THERMAL PROCESSES IN LASER WELDING OF POLYMERS*	3
V.S. Kachinskyi, Yupiter HP Manurung INVESTIGATIONS OF THE QUALITY OF WELDED JOINTS OF PIPES FROM STEEL OF ASTM A106/API 5L GRADE, USING MAGNETICALLY IMPELLED ARC BUTT WELDING*	9
S.V. Adjamskyi, G.A. Kononenko, R.V. Podolskyi APPLICATION OF SLM-TECHNOLOGY FOR MANUFACTURE OF DENTAL IMPLANTS FROM Ti-6Al-4V ALLOY*	15
Yu.M. Lankin, V.G. Soloviov, V.G. Tyukalov, I.Yu. Romanova COMPARISON OF THE PROCESSES OF ELECTROSLAG WELDING AT POWER CONNECTION BY MONO- AND BIFILAR CIRCUITS*	22
E. Turyk, I.O. Ryabtsev, M. Lomozik, K. Krasnovskyi INVESTIGATION OF THE CAUSES FOR APPEARANCE OF DEFECTS IN WELDED BUTT JOINTS OF TRAM RAILS MADE BY THERMIT WELDING*	29
Yu.M. Lankin REQUIREMENTS TO TECHNICAL CHARACTERISTICS OF RESISTANCE MICROWELDING MACHINES*	34
Yu.S. Borysov, A.L. Borysova, O.M. Burlachenko, T.V. Tsymbalista, M.A. Vasykivska, E.G. Byba COMPOSITE POWDERS BASED ON FeMoNiCrB AMORPHIZING ALLOY WITH ADDITIVES OF REFRACTORY COMPOUNDS FOR THERMAL SPRAYING OF COATINGS*	38
O.S. Milenin, O.A. Velykoivanenko, G.P. Rozyinka, N.I. Pivtorak MULTISCALE PROCEDURE OF NUMERICAL EVALUATION OF DAMAGE AND TECHNICAL STATE OF STRUCTURES FROM FIBER COMPOSITE MATERIALS**	48

*Translated Article(s) from «Automatic Welding», No. 11, 2021.

**Translated Article(s) from «Technical Diagnostics & Nondestructive Testing», No. 4, 2021.

<https://doi.org/10.37434/tpwj2021.11.01>

MODELING OF THERMAL PROCESSES IN LASER WELDING OF POLYMERS

M.G. Korab¹, M.V. Iurzhenko¹, A.V. Vashchuk¹, I.K. Senchenkov²

¹E.O. Paton Electric Welding Institute of the NASU

11 Kazymyr Malevych Str., 03150, Kyiv, Ukraine

²S.P. Timoshenko Institute of Mechanics of the NASU

3 Nesterov Str., 03057, Kyiv, Ukraine

ABSTRACT

In the work, a mathematical description of thermal processes in laser welding with the use of the classical theory of thermal conductivity was performed. The thermal cycle under the action of radiation on the surface was analyzed using the models of overall heat balance, distributed surface, point, circular and linear heat sources. The modeling of welding process consisted in solving the problem of forming thermal fields in viscoelastic polymer materials at a moving inner heat source. It was assumed that the upper part is transparent to laser radiation and the lower one has a set coefficient of light beam absorption, and their thermophysical characteristics depend on temperature. The equations of thermal conductivity and defining equations were formulated, supplemented by the boundary conditions of convective heat transfer and the initial temperature distribution. For the numerical implementation of certain equations the finite element method was used, which is based on an alternative formulation of the problem. The results of mathematical modeling showed the peculiarities of the formation of thermal fields in the transmission laser welding of polymer films at different parameters of welding mode.

KEY WORDS: laser welding, polymer films, mathematical modeling, thermal processes, temperature fields, isotherms

INTRODUCTION

The general term “radiation welding” combines methods for welding plastics with heating of the joint zone due to the conversion of the electromagnetic radiation energy of visible and infrared (IR) spectrum regions into heat [1, 2]. Light radiation occupies the range of electromagnetic wave length in the range of 0.2–1.0 μm , and infrared — from 1 to 2000 μm . The laser source creates radiation of a narrow wavelength range in visible or infrared spectrum regions, depending on type of laser. Depending on type of radiation source, three methods of welding are distinguished: infrared radiation, light welding and laser welding.

Nowadays, the most common technology of laser welding of polymer materials is welding of overlapped joints using transmission (penetrating) method. The essence of this method consists in the fact that a short-wave laser radiation of the optical or near IR region passes through a part of the welded joint which is transparent for it and absorbed with the release of heat on the contact surface of parts. A variant is also possible when laser radiation is partially absorbed by both billets by heating the welding zone.

The main feature of laser transmission welding of plastics is the need to select materials with such properties that provide absorption of laser radiation on a certain surface of the welded joint. The most widespread use belongs to that transmission overlap laser welding of sheet polymer materials when radiation passes through the upper transparent sheet and is absorbed by the lower non-transparent one. As a result, heating of nontransparent

material is observed and due to heat transfer, the whole welding zone is heated up. In such a way, polymer films or thin plates are usually welded [3].

Technologically, laser welding is more complex as compared to other methods. Sometimes it is quite difficult to determine the optimal parameters of the transmission laser welding process, in particular for thin films. Therefore, the mathematical modeling of thermal processes is relevant during this method of welding for theoretical substantiation of optimal parameters of the mode [4–6].

The properties of laser radiation significantly distinguish it from radiation of any other incoherent sources. Therefore, it is necessary to separately consider the problem of interaction of laser radiation with a substance [7]. Polymers have a complex molecular structure, so they interact differently with radiation of different wavelengths [8]. Most polymers in a pure form without dyes and impurities are transparent in the visible and near infrared range of the spectrum. For transmission laser welding, the most versatile is diode (semiconductor) lasers. These lasers are produced with many values of length of the visible and near infrared radiation ranges (from 0.4 to 1.45 μm). They have a relatively low cost and efficiency coefficient at the level of 60 %.

It is known [9] that when absorbing the radiation by a substance, the quanta power is converted into heat, whose distribution in the material occurs due to the thermal conductivity. In most cases, it can be assumed that light energy instantly converts into heat in the point where radiation is absorbed. Based on this assumption, the description of thermal processes for

laser welding can be carried out using a classical theory of heat conductivity [10].

An analytical description of the thermal cycle under the action of radiation on the surface is possible in the analysis of the following models: overall thermal balance; distributed surface source (one-dimensional case); point thermal source; circular source; linear source.

OVERALL HEAT BALANCE

If we assume that all radiation energy is spent on melting a polymer that is then removed, then in this case

$$P(1-R) = vbh\rho(c\Delta\theta + L_{ie}), \quad (1)$$

where P is the power of radiation acting on the material; b is the width of a cut zone; L_{ie} is the latent melting heat; h is the depth of notches; c is the heat capacity, ρ is the density of material.

DISTRIBUTED SURFACE SOURCE (ONE-DIMENSIONAL THERMAL FLOW)

For polymers with a high absorption index (filled with a technical carbon) and for which the ratio $\delta = \alpha^{-1} \ll (at)^{1/2}$ is performed, where δ is the penetration depth of the beam; α is the index of absorption of radiation by medium; α is the temperature conductivity; t is the radiation time, the heat source can be considered superficial [7]. In this case, the temperature distribution in the polymer and its change in time are determined by the thermal conductivity of the medium and described by the following equation:

$$\theta(z, t) = \frac{2q(at)^{1/2}}{\lambda_T} \text{ierfc} \frac{z}{2(at)^{1/2}}, \quad (2)$$

where $q = E(1-R)$, ierfc is an integral of errors; λ is the coefficient of thermal conductivity.

Temperature on the surface of material

$$\theta(0, t) = \frac{2q}{\lambda_T} \left(\frac{at}{\pi} \right)^{1/2}. \quad (3)$$

This model can be used on the condition that the radius of the laser beam is much larger than the size of the surface irradiated during the time t .

POINT HEAT SOURCE

The solution of the heat conductivity equation on the condition of absence of convection and radiation losses, and in the assumption that the heat source is instantaneously acting at the point with the coordinates (x', y', z') can be provided in the form:

$$\theta(x, y, z, t) = \frac{Q(x', y', z')}{8(\pi at)^{3/2}} \times \exp\left(-\frac{(x-x')^2 + (y-y')^2 + (z-z')^2}{4at}\right), \quad (4)$$

where Q is the amount of heat released in the volume of material.

In case of symmetrical heat distribution for a thin plate $H/4at \ll 1$, the following ratio is fair:

$$\theta(r, t) = \frac{Q}{4\pi\lambda_T H t} \exp\left(-\frac{r^2}{4at}\right). \quad (5)$$

For a moving source in a thin plate, the following ratio is fair:

$$\theta = \frac{P(1-R)}{2\pi\lambda_T H} K_0\left(\frac{rv}{2a}\right) \exp\left(-\frac{vx}{2a}\right), \quad (6)$$

where K_0 is the Bessel function of the second type of zero order.

CIRCULAR SOURCE

For most lasers, the pulse normalized by a unit in a maximum, has approximately one and the same shape if it is considered as a function of time related to the pulse duration and can be characterized in time by the function $P(t) = E(t)/E_m$. As a spatial profile of the beam, for which temperature curves will be built, it is rational to select beams with the Gaussian distribution of power density $E(r) = E_0 \exp(-r^2/r_0^2)$.

Accordingly, the density of the flow absorbed by the surface is described by the equation:

$$q(r) = q_0 \exp(-r^2/r_0^2). \quad (7)$$

Integrating the expression in time, it is possible to obtain a solution for an instantaneous point source with a Gaussian profile. It is possible to simplify the expression for the temperature by comparing the process of heat saturation and the time when the beam passes a distance equal to its radius in time (r_0/v) . If $vr_0/a < 1$, then the heat source can be considered such that slowly moves. In this case, the maximum temperature of the material is achieved in the center of the moving zone of irradiation and its value differs little from the largest one, which corresponds to a stationary heat source:

$$\theta \approx \frac{E(1-R)}{\lambda_T} \left(1 - \frac{vr_0}{4a}\right). \quad (8)$$

The given expression is fair, if $\dot{a} \sim 10^{-1} \tilde{n}^2 / \tilde{n}$ at the speeds lower than 1 cm/s and if the diameter of the beam on the surface of the polymer is not larger than 0.5 mm.

If the time r_0/v is longer than the time of heating the plate (sheet) H^2/a , then the temperature on the surface can significantly depend on the thickness of a product:

$$\theta \approx \frac{E(1-R)r_0^2}{2\lambda_T H} \ln \frac{2.25a}{r_0 v}. \quad (9)$$

From the last expression it follows that the threshold power density required to achieve the set temperature in the stationary mode, linearly grows with an increase in

the thickness of the sheet H and weakly (logarithmically) depends on the speed of the source movement.

With an increase in the speed of the source movement, the thermal effect of radiation action decreases and the maximum temperature shifts to the periphery of a moving light spot in the opposite direction to the speed vector. In this case, during transition to high speeds, when $vr_0/a \gg 1$, the value of the maximum temperature on the axis of the source movement is determined by the formula

$$\theta \approx \left(\frac{8}{\pi}\right)^{1/2} \frac{E(1-R)}{\lambda_T} \left(\frac{ar_0}{v}\right)^{1/2}. \quad (10)$$

The maximum temperature, to which the polymer is heated, corresponds to a surface temperature of semispace under the action of a pulsed heat source with the duration $2r_0/v$, which corresponds to the time passage of a moving source of its diameter. Therefore, for the polymers $\dot{\alpha} < 10^{-2} \tilde{n} \dot{\alpha} / \tilde{n}$, a condition of a fast moving source $vr_0/a \gg 1$ is provided.

Modeling of thermal processes in transmission laser welding of sheet polymer materials consisted in solving the problem of the formation of thermal fields in viscoelastic polymer materials at a stationary and a moving inner source of heat energy. It is accepted that the upper part is transparent for laser radiation, the lower part has a set absorption coefficient of a light beam, and their thermophysical characteristics depend on temperature. For some polymer materials, this dependence may be established experimentally. The thermal conductivity equation and defining equations are supplemented by the boundary conditions of a convective heat transfer and the initial temperature distribution.

FORMULATION OF THE PROBLEM

Polymer films are modeled as plates in the form of rectangular parallelepipeds of different thickness located one on one. The axis of the laser beam is directed perpendicularly to the surface of the plates and a circular heat source is located in the plane of their contact.

The beginning of the Cartesian coordinate system is located on crossing the axis of the laser beam with the upper surface of the plates. The axis z is directed along the axis of the beam, the axis x is in the plane of the plates butt and is aimed in the direction, the opposite to the direction of moving the laser beam, and the axis y is perpendicular to the butt. In the chosen system of coordinates moving together with the beam, the plates are moved at the speed of welding v , and the beam is immovable.

In the mathematical model, the processes of heat transfer during welding are described by a quasi-stationary equation of heat conductivity, and heat exchange with the environment and between the subregions of the polymer material in different phases — by nonlinear boundary conditions of thermal balance. The coefficient

of temperature conductivity is a constant having values in different subregions of the calculated region, which are equal to some of its average values for a particular phase of the metal in the appropriate subregion.

To simplify the problem, let us average the three-dimensional quasi-stationary heat equation along the coordinate y , as a result of which we obtain:

$$c_{ei} v \frac{\partial \theta}{\partial x} = \lambda_i \left(\frac{\partial^2 \theta}{\partial x^2} + \frac{\partial^2 \theta}{\partial z^2} \right) - \frac{\lambda_i}{l_Q^2} (\theta - \theta_a), \quad (11)$$

where effective heat capacity is calculated by the formula:

$$c_{ei} = \begin{cases} c_1 \rho_1 & \theta < \theta_e \\ c_2 \rho_2 \left(1 + \frac{k}{c_2} \frac{\partial f_1(\theta)}{\partial \theta} \right) & \theta_e \leq \theta \leq \theta_{i0} \\ c_3 \rho_3 & \theta_{i0} < \theta \end{cases}. \quad (12)$$

In this equation, the index $i = 1, 2, 3$ determines the parameters of the solid, liquid-solid and liquid phases, respectively; c_i, ρ_i, λ_i is the heat capacity, density and thermal conductivity of the i -phase, respectively; κ is the specific heat of melting; θ_{i0}, θ_e are the temperatures of the beginning and end of solidification; $l_Q = 2\sqrt{a_i \tau}$ is the length of distribution of the thermal wave over the time $\tau = 2r_F/v$, r_F is the radius of the beam in the focal plane; a_i is the temperature conductivity of the i -th medium; θ_a is the characteristic temperature of the plate outside the averaging region.

The boundary conditions of the problem come from the conditions of heat balance. On the surface $z = 0$ in the regions of solid, glass-like as well as a liquid and two-phase state, the condition has the form:

$$\lambda_i \left. \frac{\partial \theta}{\partial z} \right|_{z=0} = (\alpha_k + \alpha_{ri}) (\theta|_{z=0} - \theta_{gi}), \quad (13)$$

$i = 1, 2, 3 \dots$

Here α_k is the convective coefficient of heat transfer; θ_g is the gas temperature; α_{ri} is the radiation coefficient of heat transfer that satisfies the ratio

$$\alpha_{ri} = \varepsilon_i \sigma_0 (\theta|_{z=0}^2 + \theta_g^2) (\theta|_{z=0} + \theta_g), \quad (14)$$

where ε_i, σ_0 is the set emissivity factor and Stephan-Boltzman constant, respectively.

For the intensity of laser radiation, we accept the normal Gaussian distribution law, and it depends on the change of z radius of the beam

$$r_z = \left(r_F^2 + \left(\frac{z - Z_F}{\pi r_F \lambda_0} \right)^2 \right)^{1/2}. \quad (15)$$

Here Z_F is the coordinate along z of the focal plane; r_F is the radius of laser beam in the focal plane; λ_0 is the laser radiation wavelength.

For the convenience of software realization of the calculating algorithm and its presentation, all the mul-

tifold of iterations in the external cycle is divided into stages. The calculated region G at the first stage of calculations is a rectangle in the plane of the plate joint. Its sides $z = 0, z = h, x = -l_1, x = l_2$, where l_1 and l_2 are distances respectively from the left and right boundaries of the rectangle to the axis of the laser beam. The choice of values l_1 and l_2 depends on the power of the laser and the speed of welding.

APPROXIMATION OF THE EQUATION

The region of solving the problem is covered with an irregular differential grid G_h with the nodes (ih_1, ih_2) , $i = 0.1, \dots, n_1, j = 0.1, \dots, n_2$, where h_1 and h_2 are grid steps. For numerical solution of the problem, the variants of the scheme of the installation method were used. One of them for equation (11) has a form

$$\frac{\theta_{i,j}^{n+1} - \theta_{i,j}^n}{\tau} + v \frac{\theta_{i+1,j}^{n+1} - \theta_{i-1,j}^{n+1}}{2h_1} = \alpha_i \left(\frac{\theta_{i+1,j}^{n+1} - 2\theta_{i,j}^{n+1} + \theta_{i-1,j}^{n+1}}{h_1^2} + \frac{\theta_{i,j+1}^n - 2\theta_{i,j}^n + \theta_{i,j-1}^n}{h_2^2} \right) - \frac{\alpha_i}{l_0^2} (\theta_{i,j}^{n+1} - \theta_\alpha). \tag{16}$$

Except of it, the scheme of conditional approximation was also tested. We should note that in the calculated region, the convergence of a numerical solution was observed on the convergence of the value

$$\max_{i,j} |\theta_{i,j}^{n+1} - \theta_{i,j}^n|.$$

When using the second scheme, the value of the closing error from the substitution of the difference solution was additionally observed in the difference equation of thermal conductivity and difference conditions on the boundaries. In this case, naturally, in them fictitious derivatives in time were removed, and derivatives of spatial variables and nonhomogeneous terms were all copied on the last time layer. Iterations stopped as soon as these values became lower than some of the set values.

APPROXIMATION OF BOUNDARY CONDITIONS

The boundary conditions on the outer and inner boundaries (fronts between the phases of product material) are approximated with the first order. To record the boundary conditions at a specific point, it is necessary

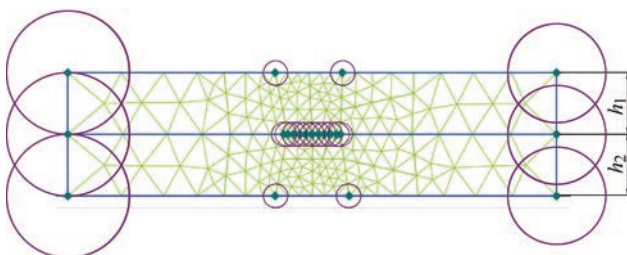


Figure 1. Finite-element grid for calculation of thermal field in polymer films during their laser welding

to have numerical values of the normal component and curvature of the boundary. Since all inner boundaries in the considered problem are certain isotherms, then when it is necessary, based on the calculated grid values of the temperature, the corresponding boundaries are found by interpolation. Boundary conditions also take into account a mobile nature of the source.

To accelerate the iterative process in all differential boundary conditions, a fictitious differential derivative of time from temperature was artificially added. Similarly, as in the equation (16), the sign in it was chosen so that the element module on the diagonal increased in the corresponding line of the matrix of the system of linear algebraic equations of the differential problem.

In the process of conducting one current iteration in the entire calculated region (global iteration), the system (16) is successively solved by passes along the axis x in all subregions. In the middle of the subregion, all possible values of j index are successively changed in it. The values of solving on the boundaries of all subregions are taken from the previous iteration. After completion of iteration, the values of the solution in all nodes on the boundary of subregions are specified. In each node on the boundary, the boundary condition is solved relative to the temperature value in the selected node. Thus, its specified value is found through the value of temperature in the adjacent nodes obtained on the mentioned iteration. It is used on the next iteration as a value for solution on the boundary.

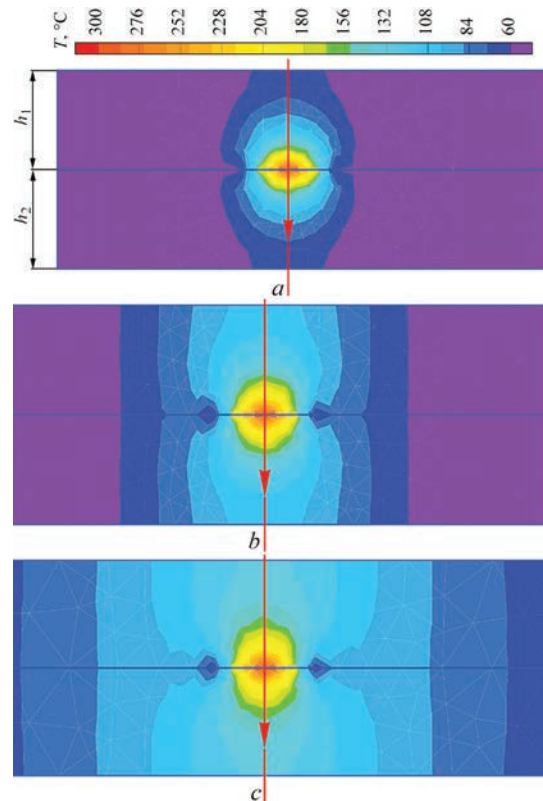


Figure 2. Evolution of temperature field in polymer films during their laser welding (static heating) $a - t = 1; b - 3; c - 10$ s. The arrow shows the direction of the laser beam (coordinate axis Y)

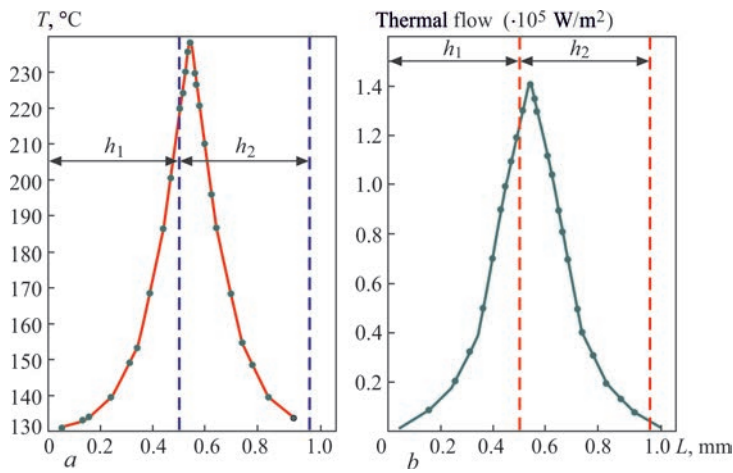


Figure 3. Distribution of temperature (a) and thermal flow (b) over thickness in the zone of joining films

In the mentioned calculations, such conditions considered to be satisfactory, when with a twice increase in the size of the region and independent refinement of the grid steps, the calculated values in the regions between the phases differed by not more than 3%. In this problem, the required size of the calculated region, of course, depends on the speed of welding. The higher it is, the greater asymmetry in the isotherm pattern relative to the axis of the laser beam.

In addition, considering the specifics of the temperature behavior of polymer materials, the thermal conditions in the welding zone should be strictly controlled and maintained at a set level. As the calculations show, the most critical parameters of the mode at a set laser power is speed of welding and width of the temperature interval of the viscous flow state $\Delta\theta_{AO}$.

For numerical realization of defined equations, the finite elements method was used, which is based on the alternative formulation of the problem. Figure 1 shows a scheme of transmission welding model and an irregular finite element grid for calculation of the thermal field. The beginning of the Cartesian coordinate system is located in the center, circumferences show different sizes of grid elements. Thermal fields

during welding of polyethylene films with a thickness of 0.2–0.5 mm by laser with a power of 10 W at a speed of 0.01–0.02 m/s were calculated.

Analysis of results from the diagrams of mathematical modeling (Figures 2–5) shows that in transmission laser welding, temperature distribution across the width of the weld is nonuniform, which is predetermined by the Gaussian distribution of power density in a laser beam. At a set laser power, more favorable conditions for the formation of a welded joint occur in the case of welding films, the upper of which has a lower thermal conductivity. The zone of maximum temperatures can be shifted due to conditions of heat transfer from the joint zone. The optimal conditions for the formation of a high-quality welded joint are the conditions under which the zone of maximum temperatures is localized in the contact area of welded films. Comparison of the results of theoretical and experimental studies shows that at set parameters of continuous welding mode, an optimum speed is a relative speed, at which heating is achieved at a depth of not less than 2/3 of the thickness of each part, counting from the plane of their physical contact.

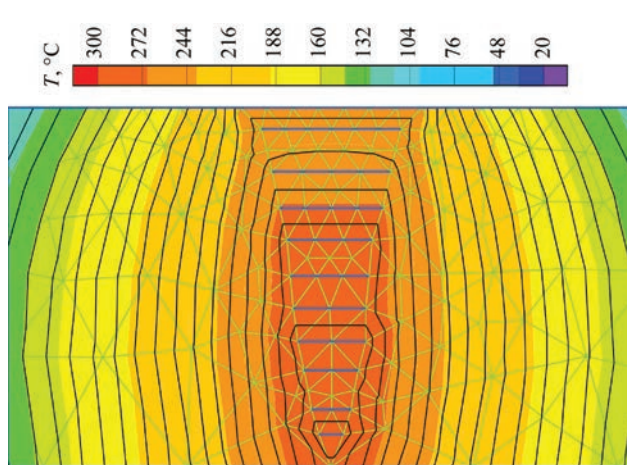


Figure 4. Cross-section of the calculated region of the plane perpendicular to the axis x at the point with the maximum width of the HAZ (Gaussian distribution in the laser beam)

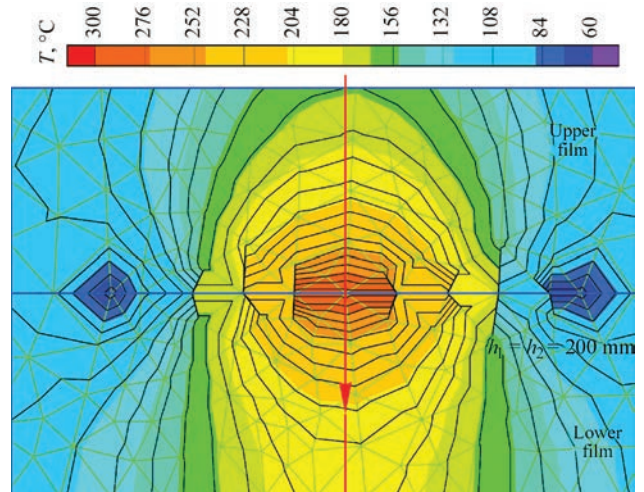


Figure 5. Temperature field and isotherms in the calculated region. The arrow shows the direction of the laser beam (coordinate axis Y)

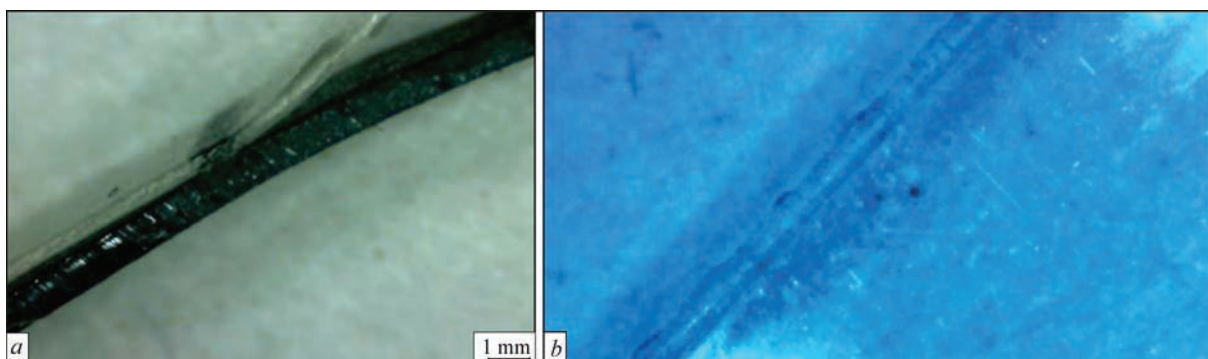


Figure 6. Appearance of welds produced using laser welding: *a* — weld of a transparent polyethylene film with a thickness of 0.5 mm, equal strength with the base material; *b* — sealed weld of a modified medical film with a thickness of 0.2 mm

Figure 6 shows the appearance of welds produced by laser welding taking into account the results of mathematical modeling of thermomechanical processes.

CONCLUSIONS

Modeling of thermal processes in transmission laser welding of sheet polymer materials was carried out. The main equations were formulated to describe heat release under the action of radiation to the surface for possible models of overall heat balance; point heat source; circular source; linear source. The mathematical model of heat transfer process during welding, described by the quasi-stationary equation of heat conductivity and non-linear boundary conditions of thermal balance, was proposed. For numerical solutions of defined equations, the finite element method was used.

The results of mathematical modeling allowed investigating the features of the formation of thermal fields in transmission laser welding of polymer films at different parameters of welding mode. It was shown how depending on power and speed of the movement of radiation source, it is possible to adjust the thermal conditions in the zone of polymer joints taking into account their absorbing properties, temperature of transition to viscous flow state, thermophysical properties of the material, heat transfer conditions and other parameters.

REFERENCES

1. Klein, R. (2011) *Laser welding of plastics*. Wiley-VCH, Verlag GmbH & Co.
2. Buketov, A., Brailo, M., Yakushchenko, S., Saprionova, A. (2018) Development of epoxy-polyester composite with improved thermophysical properties for restoration of details of sea and river transport. *Advances in Mater. Sci. and Engin.*, 6378782. <https://doi.org/10.1155/2018/6378782>.
3. Acherjee, B., Kuar, A.S., Misra, D., Mitra, S. (2011) Laser transmission welding of thermoplastics: An overview of experimental findings — process, development and applications. *J. of Manufacturing Technology Research.*, 3, 211–236.
4. Kneip, J.C., Martin, B., Loreda, A. et al. (2004) Heat transfer in semitransparent materials during laser interaction. *J. Ma-*

terials Proc. Technology, 155–156, 1805–1809. <https://doi.org/10.1016/J.JMATPROTEC.2004.04.380>

5. Ruotsalainen, S., Laakso, P., Kujanpa, V. (2015) Laser welding of transparent polymers by using quasi-simultaneous beam off-setting scanning technique. *Physics Procedia*, 78, 272–284.
6. Majumdar, A., D'Alvise, L. (2016) Simulation of the laser transmission welding of thermoplastics — Sensitivity to process parameters. In: *Proc. of NAFEMS Nordic Conf.* <https://www.researchgate.net/publication/304308496>
7. Delone, N.B. (1989) *Interaction of laser radiation with substance*. Moscow, Nauka [in Russian].
8. Vedenov, A.A., Gladush, G.G. (1985) *Physical processes in laser treatment of materials*. Moscow, Energoatomizdat [in Russian].
9. Kutateladze, S.S. (1979) *Fundamentals of the theory of heat exchange*. Moscow, Atomizdat [in Russian].
10. Lykov, A.V. (1967) *Theory of heat conductivity*. Moscow, Vysshaya Shkola [in Russian].

ORCID

M.G. Korab: 0000-0001-8030-1468,
M.V. Iurzhenko: 0000-0002-5535-731X,
A.V. Vashchuk: 0000-0002-4524-4311

CONFLICT OF INTEREST

The Authors declare no conflict of interest

CORRESPONDING AUTHOR

M.V. Iurzhenko
E.O. Paton Electric Welding Institute of the NASU
11 Kazymyr Malevych Str., 03150, Kyiv, Ukraine
E-mail: 4chewip@gmail.com

SUGGESTED CITATION

M.G. Korab, M.V. Iurzhenko, A.V. Vashchuk, I.K. Senchenkov (2021) Modeling of thermal processes in laser welding of polymers. *The Paton Welding J.*, 11, 3–8. <https://doi.org/10.37434/tpwj2021.11.01>

JOURNAL HOME PAGE

<https://pwj.com.ua/en>

Received 20.09.2021
Accepted: 29.11.2021

<https://doi.org/10.37434/tpwj2021.11.02>

INVESTIGATIONS OF THE QUALITY OF WELDED JOINTS OF PIPES FROM STEEL OF ASTM A106/API 5L GRADE, USING MAGNETICALLY IMPELLED ARC BUTT WELDING

V.S. Kachinskyi¹, Yupiter HP Manurung²

¹E.O. Paton Electric Welding Institute of the NASU
11 Kazymyr Malevych Str., 03150, Kyiv, Ukraine

²Smart Manufacturing Research Institute (SMRI) and School of Mechanical Engineering,
UiTM Shah Alam, Malaysia

ABSTRACT

Magnetically impelled arc butt welding (MIAB) is a welding process applied for joining pipes with an external magnetic field, which influences the arc displacement in a narrow gap between the pipe ends. This welding process consists of a complex interaction between the electric arc, external magnetic field and upset value. In this work, investigations were performed on MIAB welding of seamless pipes from carbon steel of ASTM A106/API 5L grade, which is used in electric power plants, boilers, petrochemical plants, petroleum processing plants and ships, where the pipeline should transport fluids and gases under high pressure and temperature. The experimental procedure includes a range of tests for development and assessment of the knowledge base on MIAB welding of seamless pipes. Then mechanical testing of MIAB welded joints of ASTM A106/API 5L sample was performed to assess its strength and weld integrity in keeping with API 1104 standard. In addition to investigations, a conceptual specification of MIAB welding procedure and protocol of welding procedure qualification for welding pipes and their further application were developed and presented. The experimental results emphasized that the MIAB welded joints demonstrate the high strength and good integrity of the weld on the level of the pipe base metal. Thus, MIAB welding can be regarded as the future fast and cost-effective welding process without expensive use of filler materials and shielding gas.

KEY WORDS: pressure welding, magnetically impelled arc, seamless pipes, carbon steel, welded joints, mechanical properties

INTRODUCTION

Magnetically impelled arc butt welding (MIAB) is an improved welding process, which is an alternative to such processes as friction, resistance and flash-butt welding. MIAB is a solid-state process of pressure butt welding of steel pipes and tubular parts [1–3]. In this process, the axes of the pipes clamped in the machine are aligned, and their ends are heated by the arc, rotating in the gap between the two pipes. Arc formation and its rotation speed are controlled by the magnetic force of the radial component of induction of the controlling magnetic field as a result of interaction of the arc current and the magnetic field in the gap. A scheme of magnetic control of the welding arc movement in the narrow gap of the pipes being welded was developed. The arc heats the pipe ends, causing a localized small band of melting and neighbouring softening in the HAZ, and then the pipes are upset to form a welded joint [4].

At MIAB welding the controlled magnetic field moves the arc in the gap between the pipe edges, as shown in Figure 1. Two pipes, ready for welding, are mounted coaxially. The magnetic systems, installed one opposite the other, form magnetic flows in the arc gap. The welding arc is excited by a short-circuit. The pipes to be welded are separated to create a certain arc

gap (from 1.5 to 2.1 mm). The interaction between the axial component of welding arc current and the radial magnetic component, directed normal to the welding arc current, generates a force. This force moves the welding arc along the pipe ends. MIAB welding uses preprogrammed control of the arc current with arc movement, which may reach the linear speed of 270 m/s. This allows achieving uniform heating of the pipe ends, thus ensuring a sound welded joint. In this study, a model of MD 101 and MD 205 machine, developed at PWI, as shown in Figure 2, was used for welding seamless pipes, operating at high temperatures.

Determination of the respective welding parameter combinations for weld quality and strength, can be a lengthy process, associated with the essential trial-and-error method, starting from analysis of the preliminary specification of the welding procedure, and then making a test welded joint for performance of nondestructive and destructive testing, such as mac-

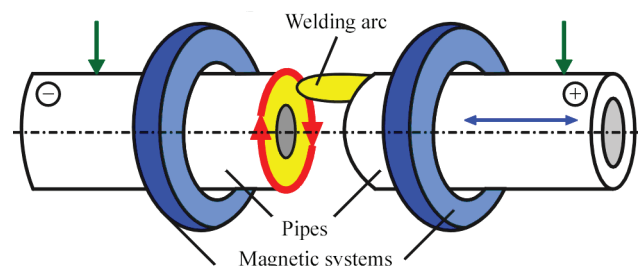


Figure 1. Scheme of MIAB welding process



Figure 2. MD-101 machine for MIAB welding of pipes

ro- and microetching for metallographic studies and tensile tests. Welding procedure specification (WPS) for MIAB is established on the base of a certificate of welding procedure approval, signed by an authorized person, such as a welding engineer, and appended to the qualification record of the welding procedure for the material to be welded [5]. In welded joint production, a written specification of the welding procedure is the “recipe” for achieving a certain weld quality, which corresponds to standard manufacturing requirements, such as API 1104.

Some studies on MIAB welding were performed. As this process is considered to be relatively new, there are very few publications on MIAB welding application in power plants, boilers, petrochemical plants, oil-and-gas plants and ships, where the pipeline should transport fluids and gases at high pressure and temperature. Taneko A., et al. [6] used voltage detector in different points inside the pipe from alloyed steel, an oscillograph and a high-speed video camera to measure the arc speeds and angles. In particular,

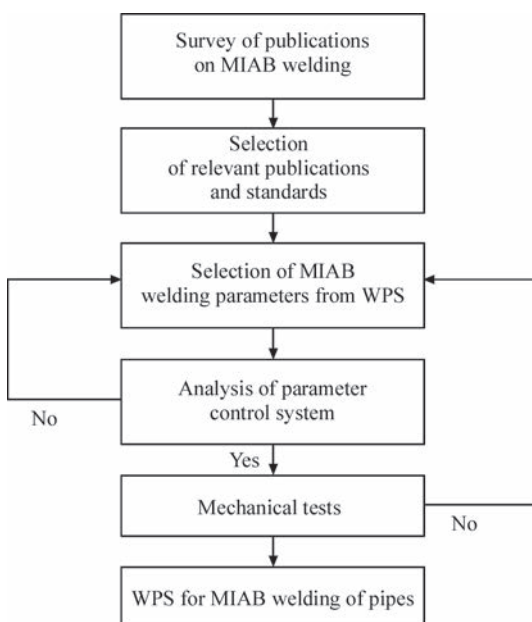


Figure 3. Block diagram of the study

they studied the interaction between the arc speed, its angle and the position, in which power is fed to the pipes. They came to the conclusion that because of the arc impact and the low electric resistance of the pipe, the arc current rises closer to the fastening connector on the pipe. Leigh F., et al. [7] presented a new perspective opened by the project of development of this technology introduction in the sector of new pipeline construction in Australia. In this study a prototype of MIAB welding machine was designed and built, which is capable of welding natural gas pipelines of 150 mm diameter, meeting the requirements of Australian oil pipeline standard AS2885.2. The results of investigations, conducted by Kachinskyi V.S., et al. [8], demonstrated the rationality of practical application of MIAB process for welding pipes and pipelines from steel X70. Edson D. [9] outlined the typical industrial applications in the automotive industry — MIAB welding for joining parts in the rear axle cover of Ford Transit car, which has two circular and two square butt welds. In works by Kachinskyi V.S., et al. [10] the results on weldability of car parts are given. The possibility of welding compact hollow car parts was studied, such as steering rod of the diameter of 22×2.2 mm, shock-absorber of the diameter of 40×2.2 mm. Beginning from 1994, MIAB-welded pneumatic springs and shock-absorbers, were manufactured in automobile plants, where more than 7.4 mln welded joints were made.

MIAB welding application in manufacture of components for truck cabs of Thyssen Krupp Automotive Systems Company was described by Hiller F., et al. [11]. Jenicek A., et al. [12] demonstrated that tubular hollow bodies, such as nuts, sleeves and bushings, can be fastened to sheets using this process with particularly high cost-effectiveness. Expanded devices for welding by arc-like pins were used to weld aluminium components with internal thread between M8 and M24 to perforated sheets. Mori S., et al. [13] evaluated the rationality of the process of MIAB welding with aluminium and aluminium-copper joints. In this structure it was difficult to achieve the required density of the magnetic flow in the butt with nonferrous materials, compared to ferrous materials. Therefore, a ferromagnetic rod was often placed inside the tube. In the study, information about the MIAB welding method developed for welding nonferromagnetic metals, is given, and the conditions and methods of butt welding of tubes from aluminium to aluminium (Al–Al) and to copper (Al–Cu) are investigated.

The work presents the results of the performed studies on MIAB welding of seamless pipes of 42 to 200 mm diameter from ASTM A106/API 5L carbon steel for high-temperature service and production,

Table 1. Mechanical properties of ASTM A106/API 5L steel

Diameter, mm	Wall thickness, mm	Ultimate strength, MPa	Yield limit, MPa	Elongation, %
42.7	3.83	415	294	31
114.3	6.02	423	305	37
168.3	10.00	429	309	39

Table 2. Chemical composition of ASTM A106/API 5L, wt. %

C	Si	Mn	P	S	Cr	Ni	Cu	Mo
0.28	0.25	1.20	0.030	0.030	0.50	0.50	0.50	0.15

which were aimed at development of a specification of MIAB welding parameters for high-temperature seamless pipes. Figure 3 shows the block diagram of the study.

IDENTIFICATION OF THE PARAMETERS OF MIAB WELDING PROCESS FOR ASTM A106/API 5L MATERIAL

SEAMLESS PIPES FROM ASTM A106/API 5L CLASS B, OPERATING UNDER PRESSURE

In this study ASTM A106/API class B material was used. It was specially developed for application in electric power plants, boilers, petrochemical plants, oil-and-gas plants and ships, where the pipelines should transport fluids and gases, having high pressure and temperature. This material lends itself to bending, flanging and similar forming operations. Mechanical properties and chemical composition of this material are given in Tables 1 and 2, respectively.

PRELIMINARY SPECIFICATION OF THE WELDING PROCEDURE

Preliminary specification of the welding procedure is an important step in WPS. This is a document, which includes the required variables of welding procedure, which must be qualified, in order to create a qualified welding procedure specification. At this stage, selection of current, time, upset pressure and arc gap is, mainly, performed by trial-and-error method in the welding machine. The research engineer also refers to the manufacturer recommendations as to the parameters. First visual examination of the welded joint is



Figure 4. Uniform formation of the welded joint

Table 4. Results of rupture testing of the welded joint of pipes of ASTM A106/API 5L grade

Outer diameter, mm	Thickness, mm	Cross-sectional area, mm ²	Yield limit, MPa	Ultimate strength, MPa
42.7	3.83	467	344.93	459.88
114.3	6.02	2048	351.28	448.93
168.3	10.00	4971	354.37	461.84

Table 5. Results of bend tests of the inner and outer surfaces of ASTM A106/API 5L grade material

Width, mm	Thickness, mm	Test results	Remarks
25.0	3.83	Satisfactory	No crack in the butt joint
12.0	10.00	Same	Same

performed for five sets of process parameters. General comments for each test are given in Table 3.

The result shows that a good weld with uniform penetration is produced in the case of weld 5, as shown in Figure 4.

MECHANICAL TESTING RESULTS

Mechanical tests, such as stretching, bending, rupture, hardness and macroetching, were conducted to API 1104 standard [14]. The rupture nsile testing results are given in Table 4. They show that the sample strength is equal to 459.88 MPa, which corresponds to that of the pipe base metal of 415 MPa, and the sample failed in the base metal, as shown in Figure 5. Absolutely acceptable results proved that the parameters of MIAB process, used for welding of ASTM A106/API 5L material, were correctly selected in terms of technology.

Table 3. Trial observation of welded joints on pipes of ASTM A106/API 5L grade

Test number	Current, A			Welding time, s				Upset pressure, bar	Arc gap, mm	Visual inspection
	I_1	I_2	I_3	T_1	T_2	T_3	T_4			
1	230	170	500	1	2.75	10.5	0.18	4.5	1.4–1.6	Nonuniform welded joint reinforcement
2	230	180	520	1	2.6	10.5	0.2	4.4	1.4–1.6	Excessive pressed-out metal in the weld
3	230	190	550	1	2.6	9.0	0.2	4.3	1.4–1.6	Same
4	230	210	570	1	2.5	8.5	0.3	4.3	1.4–1.6	”
5	230	215	600	1	2.5	8.0	0.3	4.2	1.4–1.6	Sound weld, uniform reinforcement



Figure 5. Rupture testing of a welded pipe sample



Figure 6. Inner and outer bend testing of a welded sample: *a* — pipe of the diameter of 42.7×3.83 mm; *b* — 168.3×10.00 mm

Results of side bend tests for determination of the strength of pipe welded joint are given in Table 5. As one can see from Figure 6, the sample is in an excellent state, without any signs of cracks or defects in the bending zone.

Fracture tests were performed to assess ruptures and defects of the welded sample. As one can see in Figure 7, the sample is in good condition, without porosity or lacks-of fusion on the open surface of the weld.

Hardness was checked in keeping with ASTM E92. Measurement was taken in the weld, HAZ and base metal, using Vickers *HV* 10 method, as shown in Figure 8. The measured values in the test samples were as follows:



Figure 7. Fracture testing of welded pipe sample

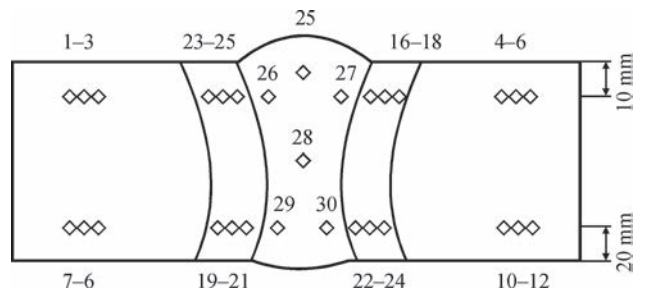


Figure 8. Results of Vickers hardness testing of a welded sample: 1 — weld; 2 — HAZ; 3 — base metal

- weld — *HV* 10–183–232;
- HAZ — *HV* 10–153–170;
- base metal — *HV* 10–145–169.

These measurement results proved that the welded joint is made using the optimum selected parameters of MIAB welding [15].

For metallographic testing the sample was prepared and etched from one side to API 1104. Examination revealed that the sample was completely fused and free from cracks, as shown in Figure 9.

RESULTS AND DISCUSSION

Recording of the welding procedure was performed for actual registration of MIAB process parameters, used for test purposes. Based on visual and mechanical testing, the recording of the welding procedure was further developed into welding procedure specification. In the working environment these parameters change, depending on many factors. So, in WPS the parameters were indicated in the range, which still would have ensured the best welding for this material. Figure 10 shows the parameters of WPS, developed for pipes from ASTM A106/API 5L material.

This information is useful in pipeline design, when engineers often face difficulties in selection of the welding process. It will help determine MIAB welding applicability for pipe industry. The given welding parameters and production data will be useful for application of pipe welding methods in a practical situation. Move over, it will help engineers to avoid mistakes, which may be costly, or to overcome problems, when a welding defect arises in production.

Welding current at MIAB welding can be divided into three stages, and welding time — into four stages. For welding ASTM A106/API 5L pipes of 42.2 mm

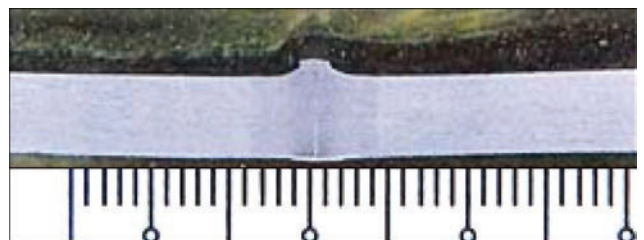


Figure 9. Welded joint macrosection

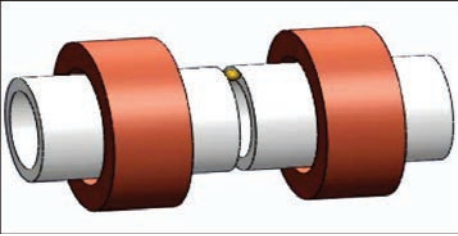
E.O. Paton Electric Welding Institute of the NAS of Ukraine					
Specification of MIAB welding procedure					
Specification: API 1104 Welding process: Magnetically-impelled arc butt welding (MIAB) Steel grade: ASTM A106/API 5L Group: class B MIAB welding machine model: MD-101; MD-205			MIAB welding WPS No.: PWI WPS/MIAB – 001 Process method: Automatic WPS purpose: Procedure for carbon steels Pipe diameter: 40–200 mm Wall thickness: 325–10 mm		
Joint configuration			Joint parts		
					
Joint characteristic			Shielding gases and materials		
Joint type: butt joint			Shielding gases: not used External blowing – not used Inner blowing: not used Welding wire: not used		
Welding parameters for pipes of 42.7 mm diameter					
Stage number	Welding current, A	Welding time t , s	Arc voltage, V	Arc gap, mm	Upset force, kN
1	220–240	2.5–2.7	24–27	1.6–1.8	41–44
2	180–190	10–12			
3	570–610	0.2–0.4			
Prepared by: _____			Certified by: _____		
Date: _____			Date: _____		

Figure 10. WPS for MIAB welding

diameter and 3.56 mm wall thickness current I1 is used for approximately 1 s, during which the welded pipes are briefly compressed up to a short-circuit and the welding rectifier is switched on. T2 (2.4–2.6 s) is the time period during which the short-circuited pipe ends are moved back for the width of the arc gap, which is followed by arc excitation between them. More over, at this time stage the arc starts accelerating in the gap along the pipe ends. During this time period, current I1 (220–240 A) is used. At T3 stage (7–9 s) the arc accelerates and rotates at a relatively high speed along the pipe ends, while heating the pipe end surfaces up to the temperature of plastic deformation to the depth of 4–7 mm. During T3 stage a current of 180–190 A (I2 current) is supplied. The welding cycle is completed by upsetting, which proceeds during time T4 (0.2–0.4 s), with feeding of higher current of 590–610 A. The general time of MIAB welding for this sample is equal to approximately 10–12 s.

From the results of mechanical tests and metallurgical examination of a MIAB welded joint (process

parameter is keeping with the fifth test in Table 3) one can understand that quality, strength and hardness are within the admissible limits, as applied in the industry of Ukraine and other countries. These results clearly emphasize that MIAB process is suitable for welding high-temperature seamless pipes.

CONCLUSIONS

In this study a steel pipe of ASTM A106/API 5L grade was welded by MIAB process, which is usually used under high-temperature conditions. Quality was checked visually and by mechanical testing, to make sure that the weld is sound. The welding process specification was developed for application in the working environment, in compliance with the standard of Ukraine and other countries. The following conclusions were made from this research:

- using MIAB process the welding time can be shortened by 80 %, compared to the conventional welding process;
- MIAB welding requires simple surface preparation and does not require any treatment;

- arc rotation during heating in air provides cleaning of the surface to be welded, thus ensuring the welding quality;

- WPS was developed for MIAB welding;
- MIAB welding complies with API 1104 standard, which is used in welding pipelines in different countries.

REFERENCES

1. Ganovski, F.J. (1974) The magnetarc welding process. *Welding and Metal Fabrication*, 206–213.
2. Kachinskyi, V. (2012) Magnetically-impelled arc butt welding for manufacture of hollow parts of mass production. *Welding Technology J. Japan*, **60**.
3. Kuchuk-Yatsenko, S.I., Ignatenko, V.Yu., Kachinskyi, V.S. (1998) Investigation of the quality of joints of pipes from heat resistant and hardening steels made by pressure welding with arc heating controlled by a magnetic field. *Avtomatich. Svarka*, **6** [in Russian].
4. Kachinskyi, V.S., Krivenko, V.G., Ignatenko, V.Yu. (2002) Magnetically impelled arc butt welding of hollow and solid parts. IIW, III-1208–02. *Welding in the World*, **46(7–8)**.
5. Dahia, A., Muhd, F., Norridzwan, N., Yupiter, HPM (2018) Parameters identification for weld quality, strength and fatigue life enhancement on HSLA (S460G2+M) using manual GMAW followed by HFMI/PIT. *J. of Mechanical Engineering*, **SI 5(4)**, 205–222.
6. Taneko, A., Fumiho, A., Kenji, T. (1986) Analysis of arc rotation velocity in magnetically impelled arc butt welding. *Welding Int. J.*, **4**, 247–253.
7. Leigh, F., Cec, S., Gabriel, S. (2003) MIAB welding: breakthrough technology for high productivity field welding of pipelines. *APIA National Convention Pipelines — Yesterday, Today and Tomorrow Convened by the Australian Pipeline Industry Association*.
8. Kachinskyi, V.S., Kuchuk-Yatsenko, S.I., Ignatenko, V.Yu., Koval, M.P. (2010) Magnetically-impelled arc butt welding of pipes of steel X70. *Australasian Welding J.*, **55**, Second Quarter.
9. Edson, D.A. (1982) *Magnetically impelled arc faying surfaces welding of thick wall tubes*. IIW, IM-726–82.
10. Kachinskyi, V.S., Kuchuk-Yatsenko, S.I., Ignatenko, V.Yu. (2010) Magnetically-impelled arc butt welding of automobile parts. *Australasian Welding J.*, **55**, Second Quarter.
11. Hiller, F., Schmidt, M., Breiksch, J. (2003) Use of the magnetarc welding process in the production of truck cab suspension systems. *ThyssenKrupp Techforum*, 40–43.
12. Jenicek, Cramer, Bush, H. (2005) Weld on aluminium materials: A further development for joining of small hollow bodies using a magnetically impelled arc. *Welding and Cutting*, **4**, 10–14.
13. Mori, S., Yasuda, K. (1990) Magnetically impelled arc butt welding of aluminum pipes. *Transact. Japan Weld Society*, **21**, 3–10.
14. API STANDARD 1104 (2013) *Welding of pipelines and related facilities*. American Petroleum Institute.
15. Cvetkovski, S., Slavkov, D., Magdeski, J. (2003) Welding procedure specification for arc welding of St 52-3N steel plates with covered electrodes. In: *Proc. of 3rd BMC*, 152–160.

ORCID

V.S. Kachinskyi: 0000-0001-9695-6434

CONFLICT OF INTEREST

The Authors declare no conflict of interest

CORRESPONDING AUTHOR

V.S. Kachinskyi

E.O. Paton Electric Welding Institute of the NASU

11 Kazymyr Malevych Str., 03150, Kyiv, Ukraine

E-mail: 4chewip@gmail.com

SUGGESTED CITATION

V.S. Kachinskyi, Yupiter HP Manurung (2021)

Investigations of the quality of welded joints of pipes from steel of ASTM A106/API 5L grade, using magnetically impelled arc butt welding. *The Paton Welding J.*, **11**, 9–14. <https://doi.org/10.37434/tpwj2021.11.02>

JOURNAL HOME PAGE

<https://pwj.com.ua/en>

Received 21.09.2021

Accepted: 29.11.2021

<https://doi.org/10.37434/tpwj2021.11.03>

APPLICATION OF SLM-TECHNOLOGY FOR MANUFACTURE OF DENTAL IMPLANTS FROM Ti–6Al–4V ALLOY

S.V. Adjamskyi¹, G.A. Kononenko^{1,2}, R.V. Podolskyi^{1,2}

¹LLC “Additive Laser Technology of Ukraine”

144 Rybinska Str., 49000, Dnipro, Ukraine

²Z.I. Nekrasov Iron & Steel Institute of the NASU

1 Sq. Academician Starodubov, 49000, Dnipro, Ukraine

ABSTRACT

Nowadays, SLM-technology has found application in various fields, including dental. The manufacture of dental implants by SLM has significant advantages. The aim of the work was the development and manufacture of equipment, practicing printing conditions by SLM technology and electrochemical polishing of dental implants with Ti–6Al–4V. The titanium Ti–6Al–4V alloy of the chemical composition, wt.%: 6.21 Al; 4.03 V; 0.04 Fe; 0.1 C; 0.7 O; 0.02 N; Ti – base, was used. The source material was examined using a scanning electron microscope REM-106 and microstructure was examined by CarlZeiss AxioVert 200M mat. The mass control was performed by the analytical scales ADV-2000. Electrochemical polishing was performed in a solution of hydrofluoric acid (HF), nitric acid (HNO₃) with glycerol (C₃H₈O₃). The ultra-compact 3D printer Alfa-150D with a working field size of 150×150×180 mm was designed and manufactured. The printer is equipped with a high-precision ytterbium laser with air cooling of 200 W power. The positioning accuracy of the laser beam is 0.15 μm. The thickness of the working layer is 20–100 μm. The samples of implants from Ti–6Al–4V were made according to experimental technological conditions: constant laser power — 195 W, laser beam scanning speed — 1000–1200 mm/s with a step of 50 mm/s, distance between beam passes — 0.09–0.12 mm with a step of 0.01 mm at a constant scanning speed. The set conditions: laser power — 195 W, scanning speed — 1000 mm/s and distance between tracks — 0.12 mm provide the density of metal samples of more than 99.99 %. On the implants manufactured according to the recommended conditions, the effect of current (0.5–2.5 A), voltage (12–20 V) and duration (3–6 min) on mass loss during electrochemical polishing was investigated. Rational conditions of posttreatment were established with the use of visual analysis. Rational conditions (current — 2 A, voltage — 17 V) of electrochemical polishing of dental implants for reduction of roughness and during maintenance of accuracy of geometry in the field of a thread were established. The dependence of mass loss of dental implants during electrochemical polishing depending on the duration of treatment was established.

KEY WORDS: selective laser melting, titanium alloy, dental implant, equipment development

INTRODUCTION

Selective Laser Melting (SLM) has found a wide application in recent years due to the possibility of manufacturing of high-density complex profile products based on a computer model with almost any metal powders (zinc, bronze, steel, titanium and titanium alloys, aluminium and aluminium alloys, precious metals, etc.)

Using selective laser melting, it is possible to create unique products of a complex profile without the use of a large amount of expensive fixture and almost without material wastes. Nowadays, the technology of selective laser melting has found its application in different industries, including dental.

Traditional manufacture of dental prostheses, crowns, bridges, which is performed on a cast model from teeth, becomes a thing of the past. It takes a lot of time associated with unpleasant senses and discomfort while removing cast models in a traditional way. The work of dental technicians is very labour-intensive and takes a lot of time to get a good result. A unique shape of each

tooth according to the individual needs of a patient is very difficult to reproduce using manual manufacture or milling machine. In addition, in the milling technology in the course of treatment of a monolithic block of a material, up to 90 % goes to chips.

Modern clinics gradually transfer to 3D technologies, which become irreplaceable in dentistry and prosthetics. To produce the model of the implant in a digital variant, it is only necessary to carry out 3D scanning of patient's tooth cavity. And the creation of the product itself in additive manufacturing proceeds layer-by-layer by adding a portion of the material according to the set model. The used materials represent not a monolithic block as during milling, but a metallic powder. At the same time, 98 % of the powder, which was not used in building, is used for the second time during manufacture of new batches of products. Therefore, it is actually a nonwaste production. The use of modern technologies allows increasing the production volumes without increasing the number of staff.

But most important thing is that except of saving time and costs, modern 3D printers guarantee a high

Table 1. Mechanical properties of titanium alloy and bone [10]

Material	$\sigma_{0.2}$, MPa	σ_r , MPa	σ_{-1} , MPa	$E \cdot 10^{-4}$, MPa	δ , %	ψ , %
Ti-6Al-4V	795	860	400	11.5	10	25
Bone	250	–	200	2.5	0.5	–

accuracy and quality of finished products. Metal additive manufacturing technologies such as SLM and DMLS, are especially effective when creating unique metal parts that are not produced serially, but which are fully functional and produced in a short time. For printing in dentistry, mainly selective laser melting (SLM) is used, which provides the smallest porosity of metal products by a successive fusion of layers of metallic powder using laser. When filling the working chamber by inert gas, a nonoxidable environment is created, which allows using all types of materials, including cobalt-chromium alloys, titanium and many other.

The Company LLC “ALT Ukraine” has an experience in creating 3D-printers that allow creating parts by SLM technology used in such highly critical industries as aircraft and rocket building and precision machine building [1–3].

The production of implants from titanium alloys of medical purpose with the use of additive technologies has the following advantages: providing optimal surface porosity in the form of a spongy structure with recommended parameters for intensive osteosynthesis and osteointegration; formation of transitional surfaces with a set geometry and roughness, creating all conditions in such a way that impede the penetration of infection in the contact zone with soft tissues and skin of a patient; formation of channels of a complex shape inside the implant for inner supply of medicines as well as thin-walled elements; formation of a thread with any profile, including a variable diameter and a step; creation of joining surfaces for quick-replaceable abutments [4].

Thus, designing of equipment and its domestic production, practicing conditions of SLM-technology for manufacture of high-quality products of dental purpose is a relevant task.

STATE-OF-THE-ART OF ISSUE DEVELOPMENT

The Ti-6Al-4V alloy (the known analogues is VT6, Grade 5) is widely used in the field of additive technologies for the manufacture of implants. This alloy is inert in relation to the biological environment [5, 6]. The titanium matrix of a part enters into a comprehensive interaction with tissues, including mechanical, electrochemical, thermal and hydrodynamic [7, 8].

This alloy has low values of the elastic modulus (Table 1), which allows producing porous, spongy,

mesh structures of materials close to the properties of human osseous tissue [9].

The parts manufactured by the method of additive manufacturing may have other mechanical properties as compared to a part manufactured by a traditional manufacturing method. Different behaviour can be explained by differences in microstructure [11].

One of the common methods of posttreatment of parts manufactured according to SLM technology is electrochemical polishing [12, 13]. By means of electrochemical polishing, the precision of a part is achieved, which in this case is a thread for placing implant in a jaw bone.

For the manufacture of dental products, small 3D-printers are used, which have a platform size for building of less than 150×150×150 mm. Usually small machines have a relatively small laser power of <200 W and a low speed of build-up. However, the machines of this category have a relatively small area of beam in focus (35–50 μm), and due to this fact, they have a better resolution, smaller deviations from the sizes, higher surface quality and detailing of parts. In [14, 15] a list of investigating and scientific machines and models for realization of selective laser melting technology is given.

The aim of the work was to design and manufacture equipment, practicing printing conditions using SLM technology and electrochemical polishing of dental implants with Ti-6Al-4V.

MATERIAL AND RESEARCH METHODOLOGY

For materials of medical purpose, an important issue is the ratio of biocompatibility, resistance to corrosion and strength. To manufacture dental implants in the work titanium Ti-6Al-4V alloy with the chemical composition, wt.%: 6.21 Al; 4.03 V; 0.04 Fe; 0.1 C; 0.7 O; 0.02 N; Ti — base, was used. The source material was examined by means of a scanning electron microscope REM-106 (Figure 1, *a*) to determine the shape and sizes of particles. Figure 1, *b* shows the results of the analysis.

Examination of microstructure was carried out in optical microscopes Olympus Tokyo and Carlzeiss Axio Vert 200M mat. Study of the samples density was carried out by the microstructural method using the Atlas software and its standard Threshold module with the determination of the area percent occupied by defects.

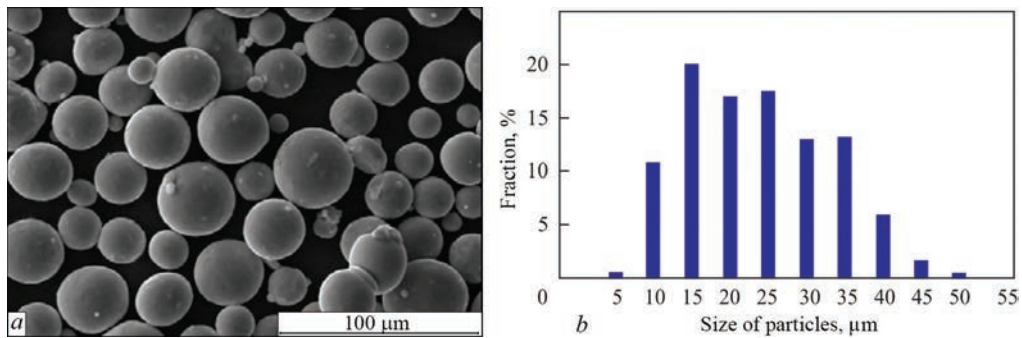


Figure 1. Particles of the source material Ti-6Al-4V ($\times 500$) (a) and results of granulometric analysis (b)

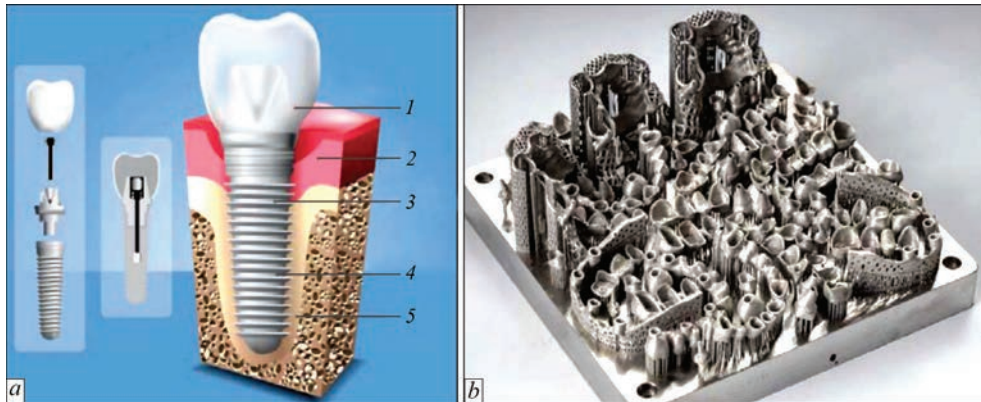


Figure 2. Schematic image of dental implant (a): 1 — crown; 2 — gum; 3 — dental implant; 4 — tooth root; 5 — jaw bone [16], implants simultaneously manufactured on the platform (b)

Application of modern technologies of additive manufacturing allows not only manufacturing implants as close as possible to the individual parameters of a patient (Figure 2, a), simultaneously producing a large number of implants with a different geometry (Figure 2, b), achieving high values of mechanical properties due to a unique structure, which is formed at high cooling rates in small melt pools, but also improving osteointegration due to the developed surface between the apices of a thread.

Printing of samples was carried out in the 3D-printer Alfa-150D of the LLC “Alt Ukraine” production. Electrochemical polishing was carried out in the solution of hydrofluoric acid (HF), nitric acid (HNO_3) with glycerol ($\text{C}_3\text{H}_8\text{O}_3$). Mass control was carried out using analytical scales ADV-2000.

RESULTS OF INVESTIGATIONS

Ultracompact 3D-printer (overall dimensions: $730 \times 700 \times 1818$ mm; mass: 450 kg) of the updated Alfa-150D model with a size of the camera of the working field $150 \times 150 \times 180$ mm was designed and manufactured (Figure 3). This allows placing it even in a small-sized room. The printer is equipped with a single optical system, a high-precision fiber (ytterbium) laser with continuous radiation and air cooling with a rated optical capacity of 200 W and the diameter of the focal spot of $45 \mu\text{m}$ was used. The thickness of the layer ranges from 20 to $100 \mu\text{m}$, the accuracy of

positioning of the laser beam is $0.15 \mu\text{m}$, the inert gas consumption (argon) during printing is up to 3 l/min.

Also, among the advantages of the 3D-printer Alfa-150D the following can be noted:

- build-up chamber with the ability to prepare printing process and unpacking of finished products without the use of additional tools for individual protection;
- system of filters regeneration, which allows carrying out the procedure of self-cleaning of filtering



Figure 3. Appearance of 3D-printer Alfa-150 D

Table 2. Experimental conditions of SLM-technology during printing from the powder of titanium Ti-6Al-4V alloy and density of sample metal

Number of sample	Scanning speed, mm/s	Interval between beam passes, mm	Metal density, %
1	1000	0.09	99.85
2		0.10	99.92
3		0.11	99.95
4		0.12	99.99
5	1050	0.09	99.88
6		0.10	99.93
7		0.11	99.98
8		0.12	99.95
9	1100	0.09	99.91
10		0.10	99.95
11		0.11	99.99
12		0.12	99.93
13	1150	0.09	99.92
14		0.10	99.98
15		0.11	99.95
16		0.12	99.88
17	1200	0.09	99.94
18		0.10	99.99
19		0.11	99.3
20		0.12	99.82

elements, significantly reduces the costs and the need to replace gas filters;

- support of inert medium and minimum oxygen content in the build-up chamber, insulation of powder in the feeding hopper from the outer environment to prevent oxidation is particularly important for manufacture of medical devices;

- built-in industrial video camera for continuous monitoring of the process of building and archiving data with a high resolution of shots.

Samples of implants were manufactured by the SLM-technology with the use of titanium Ti-6Al-4V alloy powder on the following experimental technological conditions: constant laser power — 195 W, scanning speed of the laser beam changed from 1000 to 1200 mm/s with a step of 50 mm/s, distance between the beam passes changed from 0.09 to 0.12 mm with a step of 0.01 mm at a constant scanning speed (Table 2), shielding gas — argon was used.

The examination of microsections of main body of samples showed that their average density amounts to 99.9 % (Tables 2, 3).

The rational conditions were selected so, that allow manufacturing parts of Ti-6Al-4V alloy by SLM

Table 3. Microstructure ($\times 100$) of Ti-6Al-4V alloy during manufacture by SLM-technology with the use of the following experimental conditions

Table 4. Conditions of electrochemical polishing of samples

Marking of samples	Current, A	Voltage, V
4	2.5	19
4-2	1.0	15
3-1	1.0	12
6-1	2.0	17
2-2	0.5	12
5-2	1.5	17
3-2	2.0	19
4-1	2.5	20

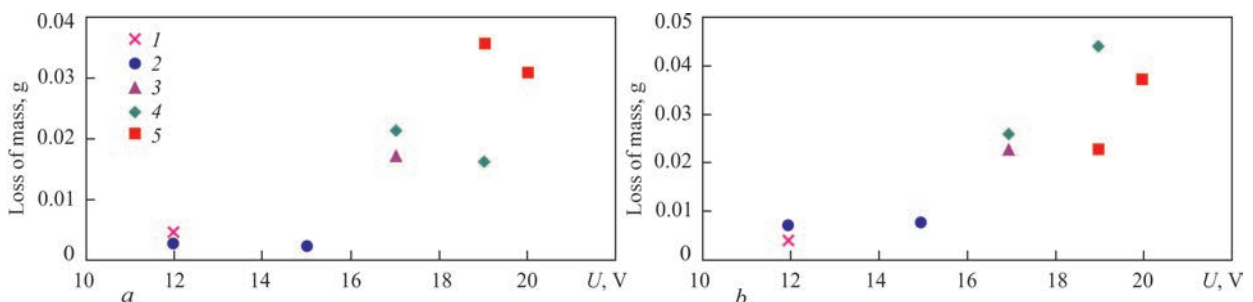
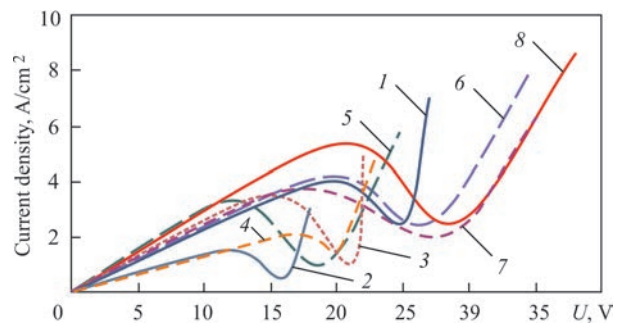
technology with a high metal density, based on which implants were manufactured with a developed surface between the apexes of a thread according to the model provided by a customer.

An important stage in the manufacture of dental implants is the posttreatment of their surface. Usually, sandblast treatment and electrochemical etching or polishing are used. In the study of implants of world manufacturers [17, 18], it was established that the use of sandblasting leads to the presence of silicon oxide residues on the implant surface, which can negatively affect osteointegration and the formation of osseous tissue.

In the work practicing of conditions of electrochemical polishing of products from Ti-6Al-4V alloy was carried out. Experimental conditions are presented on the ideal volt-ampere curve (Figure 4) and in Table 4.

Based on the results of the analysis of the volt-ampere curve, it was found that zones with optimal polishing conditions were on the samples 6-1, 4-1 and 3-2. According to these conditions, a stable zone of optimal conditions of electrochemical polishing was obtained, this zone was formed in the voltage range from 25 to 30 V, with a current range from 2.0 to 2.5 A. Samples that were subjected to electrochemical polishing with current parameters from 0.5 to 1.0 A have a small zone of stability with a rapid transition to the zone of bubble boiling, which resulted in a point corrosion of the material, followed by a small destruction of the implant thread.

The feature of SLM-technology is the presence of a powder that contacts tracks of a product contour. As a result, powder particles are fused-in into the limiting volumes of metal near the outer surface. In this work,


Figure 5. Loss of mass of dental implants under the following experimental conditions of electrochemical polishing: *a* — after 3; *b* — after 6 min: 1 — current — 0.5; 2 — 1.0; 3 — 1.5; 4 — 2.0; 5 — 2.5 A

Figure 4. Volt-ampere curves of studied samples: 1 — 4; 2 — 2-2; 4 — 5-2; 6 — 3-2; 7 — 6-1; 8 — 4-1

the control of the mass loss was carried out in order to determine the rational conditions of electrochemical polishing to remove particles without destroying the main part (Figures 5–7).

Based on the received data of mass loss from voltage at a variable current, the diagrams were constructed, from which the highest mass loss intensity occurs after 3 min of electrochemical polishing at a current of 2.5 A and a voltage of 20 V, and during 6 min it occurs in the range of current of 2.0–2.5 A and voltage of 19–21 V (Figure 5).

It was established that an increase in the duration of polishing from 3 to 6 min leads to some increase in the mass loss (Figure 6). At a small voltage of 12 V with an increase in the duration of the process, a slight change in the mass of an implant occurs, indicating that the polishing process occurs according to nonrational conditions, the oxide film on the surface becomes an obstacle to the course of the polishing process. With an increase in voltage, the difference in mass loss after 3 and after 6 min increases. The applied current corresponds to the conditions given in Table 4.

A visual analysis of implant data was performed (Figure 7). It can be seen that at the conditions: current — 1 A and voltage — 12 V (sample 3-1) after 3 min of polishing, on the surface a significant amount of fused-in particles remained, a metallic luster is absent, indicating a high roughness. After polishing during 6 min, the roughness decreased, but it still remained high enough. At the same time, the oxide film of blue colour was formed.

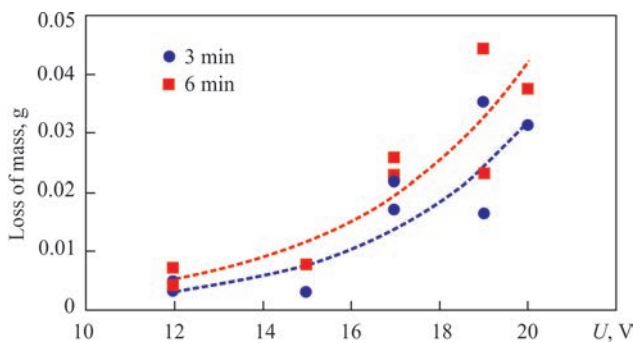


Figure 6. Loss of mass of dental implants in electrochemical polishing depending on duration of treatment

During polishing on the conditions of 2 A and 17 V (for example, sample 6–1) after 3 min of treatment, the implant has a moderate metallic luster, the surface of the thread does not contain a great amount of fused-in particles, the product geometry has a high accuracy. With an increase in the duration of polishing, an excessive etching of the thread near the apex of the implant occurs. As far as this area has a smaller surface area, then all the processes occur most intensively near it.

Application of conditions 2.5 A and 20 V (for example, sample 4–1) already after 3 min of polishing leads to the loss of the thread geometry, and after 6 min, this effect is intensified.

Based on the results of the analysis of the obtained data, rational conditions of electrochemical polishing of dental implants were established, in which the process occurs stably and effectively: current — 2 A, voltage — 17 V, duration — 3 min.

CONCLUSIONS

1. Modern progressive equipment was designed and manufactured by the domestic manufacturer to realize the technology of selective laser melting for using in the dentistry: 3D-printer Alfa-150D manufactured by LLC “ALT Ukraine”.

2. Technological conditions of manufacturing dental implants from Ti–6Al–4V alloy by the technology of selective laser melting were experimentally determined, allowing achieving a density of 99.99 %: laser power — 195 W, speed of scanning – 1000 mm/s, distance between tracks — 0.12 mm.

3. Based on the constructed actual volt-ampere curves and experimental studies, rational conditions (current — 2 A, voltage — 17 V) of electrochemical polishing of dental implants were established to reduce roughness when providing the accuracy of geometry in the region of the thread.

4. The dependence of the mass loss of dental implants was established during electrochemical polishing depending on treatment conditions. It was shown that the pattern of mass loss with an increase in voltage has a nonlinear character. For different exposure

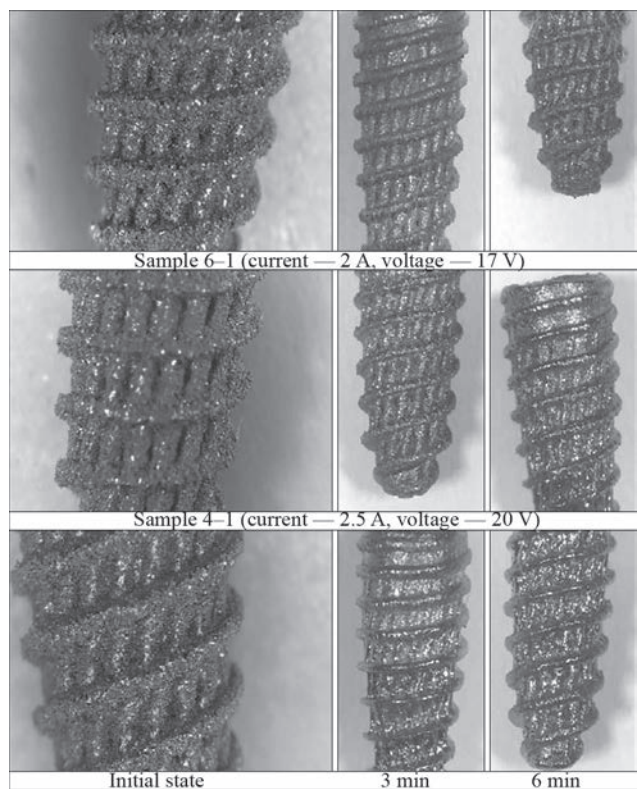


Figure 7. Change in the appearance of samples after electrochemical polishing on the experimental conditions

time in the electrolyte of experimental samples, this pattern has a close character. Moreover, an increased duration leads to a greater mass loss.

REFERENCES

- Adjamskiy, S.V., Kononenko, G.A., Podolskiy, R.V. (2020) Influence of technological parameters of SLM-process on porosity of metal products. *The Paton Welding J.*, **10**, 13–18. DOI: <https://doi.org/10.37434/as2020.10.03>
- Adjamskiy, S.V., Kononenko, G.A., Podolskiy, R.V. (2020) Prospects for application of additives technologies in aircraft and rocket production. *Aviats.-Kosmich. Tekhnika i Tekhnologiya*, **7**(167), 59–65 [in Russian]. DOI: <https://doi.org/10.32620/akt.2020.7.09>
- Adzhamskiy, S.V., Kononenko, H.A., Podolskiy, R.V. (2021) Analysis of structure after heat treatment of Inconel 718 heat-resistant alloys made by SLM-technology. *Metallofiz. Noveishie Tekhnol.*, **43**(7), 909–924 [in Ukrainian]. DOI: <https://doi.org/10.15407/mfint.43.07.0909>
- (2021) *Additive Laser Technology*. <https://alt-print.com/uk/medicine>
- Lukyanchenko, V.V., Malyasova, M.G. (2010) Metals in implantology. *Ortopediya, Travmatologiya i Protezirovaniye*, **3**, 130–132 [in Russian].
- Rozenberg, O.A., Shejkin, S.E., Sokhan, S.V. (2010) Prospects of application of commercially pure titanium for implants of osseous surgery. *Novi Materialy i Tekhnologii v Mashynobuduvanni*, **2**, 50–54 [in Russian].
- Dolgalev, A.A., Svyatoslavov, D.S., Put, V.A. et al. (2019) Morphological assessment of osteointegration at substitution of defect of lower jaw by implants made using additive technologies: Experimental study. *Meditinskii Alfavit. Seriya Stomatologiya*, Vol. 1, **380**(5), 63–68 [in Russian].

8. Vasilyuk, V.P., Shtraube, G.I., Chetvertnykh, V.A. (2013) Application of additive technologies in restoration of defects of facial skeleton. *Permskij Meditsinskij Zhurnal*, 30(3), 60–65 [in Russian].
9. Khrapov, D., Surmeneva, M.A. (2019) Study of mechanical properties of composite based on mash scaffold made of Ti–6Al–4V alloy using the method of additive technologies and polycaprolactone. In: *Proc. of 16th Int. Conf. of Students, Graduate Students and Young Scientists on Prospects of Fundamental Sciences Development (Tomsk, 23–26 April, 2019)*. Tomsk, TPU, Vol. 1: Physics, 346–248.
10. Topolsky, V.F., Akhonorin, S.V., Grigorenko, G.M., Petrichenko, I.K. (2012) Development of new titanium bio-compatible alloys for medical application. *Sovrem. Elektrometall.*, 106(1), 22–25 [in Russian].
11. Kahlin, M. (2017) *Fatigue performance of additive manufactured Ti6Al4V in aerospace applications. 15: Licentiate Thesis*, 1775, 71.
12. Adjamskiy, S.V., Kononenko, G.A., Podolskiy, R.V., Badyuk, S.I. (2021) Examination of efficiency of electrochemical polishing of variable cross-section samples with different roughness from AISI 316L steel made using SLM-technology. *Aviats.- Kosmich. Tekhnika i Tekhnologiya*, 170(2), 66–73 [in Ukrainian]. DOI: <https://doi.org/10.32620/akt.2021.2.08>
13. Łyczkowska-Widłak, E., Lochyński, P., Nawrat, G. (2020) Electrochemical polishing of austenitic stainless steels. *Materials*, 13(11), Article id: 2557, DOI: <https://doi.org/10.3390/ma13112557>
14. Adjamskiy, S.V., Kononenko, G.A., Podolskiy, R.V. (2021) Improving the efficiency of the SLM-process by adjusting the focal spot diameter of the laser beam. *The Paton Welding J.*, 5, 18–23. DOI: <https://doi.org/10.37434/as2021.05.01>
15. Khorasani, A., Gibson, I., Kozhuthala, J. Veetil, Ghasemi, A.H. (2020) A review of technological improvements in laser-based powder bed fusion of metal printers. *Int. J. Adv. Manuf. Technol.*, 108, 191–209.
16. (2019) Periodontal Associate LLC. *Same-Day Dental Implants*. <https://www.periodontalassociatesnj.com/dentistry/dental-implants/same-day-dental-implants>
17. Gurin, P.A., Skorik, N.A. (2018) Comparative morphological and chemical analysis of surface of helical dental implants of *AnyOne system (South Korea)*, *Biohorizons (USA)* and *INO (Israel)*, *Radix-Oston (Belarus)* and *Radix-Balance (Belarus)*. *Transact. of NMAPO, Ukraine*. Ed. by Yu.V. Voronenkov. Kyiv, 133–156 [in Ukrainian].
18. Edwards, P., Ramulu, M. (2014) Fatigue performance evaluation of selective laser melted Ti–6Al–4V. *Mater. Sci. and Engineering*, A 598, 327–337.

ORCID

S.V. Adjamskiy: 0000-0002-6095-8646,
 G.A. Kononenko: 0000-0001-7446-4105,
 R.V. Podolskiy: 0000-0002-0288-0641

CONFLICT OF INTEREST

The Authors declare no conflict of interest

CORRESPONDING AUTHOR

G.A. Kononenko
 LLC “Additive Laser Technology of Ukraine”
 144 Rybinska Str., 49000, Dnipro, Ukraine
 E-mail: perlit@ua.fm

SUGGESTED CITATION

S.V. Adjamskiy, G.A. Kononenko, R.V. Podolskiy (2021) Application of SLM-technology for manufacture of dental implants from Ti–6Al–4V alloy. *The Paton Welding J.*, 11, 15–21. <https://doi.org/10.37434/tpwj2021.11.03>

JOURNAL HOME PAGE

<https://pwj.com.ua/en>

Received 17.09.2021

Accepted: 29.11.2021

<https://doi.org/10.37434/tpwj2021.11.04>

COMPARISON OF THE PROCESSES OF ELECTROSLAG WELDING AT POWER CONNECTION BY MONO- AND BIFILAR CIRCUITS

Yu.M. Lankin, V.G. Soloviov, V.G. Tyukalov, I.Yu. Romanova

E.O. Paton Electric Welding Institute of the NASU
11 Kazymyr Malevych Str., 03150, Kyiv, Ukraine

ABSTRACT

Electroslag welding (ESW) with wire electrodes with a bifilar circuit of power connection is not applied now. There is every reason to believe that such a connection circuit has even more advantages over the monofilar ESW. Therefore, additional special investigations of the process of bifilar ESW are required. A comparison is given of the process of electroslag welding at power connection by the monofilar circuit and by the bifilar circuit with equalizing wire and doubling of secondary voltage. The results of comparison of both the ESW circuits by energy consumption are given; regularities of heat evolution in the slag pool at the change of its geometrical parameters, coordinates of the points and depth of immersion of the electrodes, value of voltage applied to the electrodes and electrode feed rate were studied.

KEY WORDS: electroslag welding, bifilar circuit, slag pool, metal pool, electric conductivity

INTRODUCTION

Automatic electroslag welding (ESW) is performed with application of one, two, three and more electrode wires. In two-electrode units the electrode wires are connected to the power source in parallel by the electrode–welded item circuit. In 1960ties PWI developed a new process of electroslag remelting (ESR), so-called bifilar electroslag remelting [1–6]. The essence of the method consists in that in a bifilar furnace two consumable electrodes are connected in series to the secondary winding of a single-phase transformer. However, alongside its advantages (such as favourable location of the zones of the main heat evolution in the slag pool, reduction of reactive resistance of the furnace load), the two-electrode furnace turned out to be operational only in a certain range of remelting modes, as a result of ineffective self-regulation, that is electrode melting became unstable at disturbances, acting on the process. To eliminate this drawback with preservation of the advantages of the bifilar circuit, the secondary winding of the power transformer is made with a midpoint, connected to the product being welded by an equalizing wire.

Bifilar ESW with wire electrodes is currently not applied. There is every ground to believe that it has even more advantages over monofilar ESW than in the case of ESR. As the cross-sectional area of consumable electrodes at ESW and ESR differs considerably, the thermophysical processes, causing their melting, also differ essentially. Therefore, additional specialized research of the process of bifilar ESW is required. Such investigations were conducted by

mathematical modeling of the processes of two-electrode ESW with the monofilar and bifilar circuit of welding unit connection to ac power source. A circuit of bifilar ESW with an equalizing wire was selected for comparison with the monofilar ESW with the circuit as in Figure 1, *a*. This wire connects the midpoint of the welding transformer secondary winding with the item being welded (Figure 1, *b*).

The objective of this work is comparison of the separate influence of different factors on ESW thermal processes at power connection by the monofilar circuit and by the bifilar circuit with an equalizing wire and doubling the secondary voltage of the power source, by conducting a mathematical experiment.

Figure 1 gives the variants of ESW power circuits.

AD-381Sh unit [7], developed at PWI, was used for physical experiments. Modeling was based on experimental data on ESW with the monofilar power circuit, which were obtained under the laboratory conditions at PWI.

Technological parameters of experimental ESW were as follows: item thickness $S = 80$ mm; distance between the first electrode and the closest water-cooled shoe $L_1 = 10$ mm (at symmetrical arrangement of the electrodes relative to each other); slag pool depth $h_{sl} = 50$ mm; electrode wire diameter $d_{el} = 3$ mm; electrode number $n = 2$, item from 09G2S; electrode wire from Sv08G2S steel; AN-8 flux; forming shoes from copper. Table 1 gives the data on ESW technological mode.

Results of experimental two-electrode ESW, conducted with the monofilar power circuit, were used for validation of ESW mathematical model. Mathe-

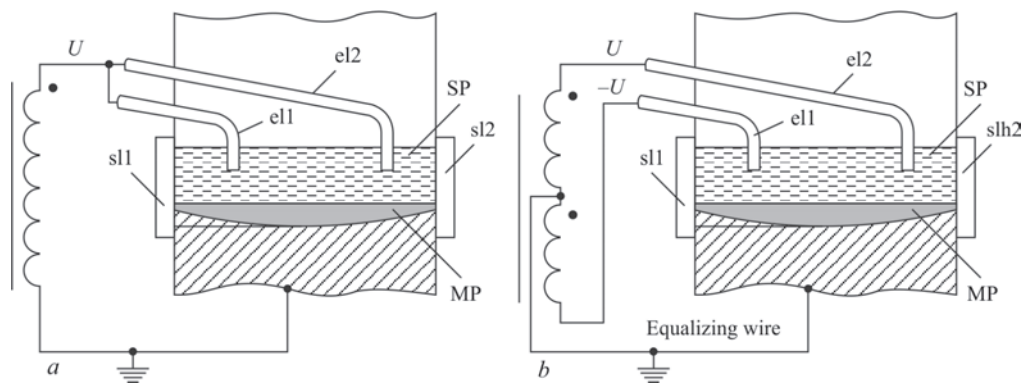


Figure 1. Two-electrode ESW power circuits: *a* — monofilar power circuit; *b* — bifilar power circuit; U — power source voltage; $el1$ and $el2$ — consumable electrodes; $sh1$ and $sh2$ — water-cooled shoes; SP and MP — the slag and metal pool

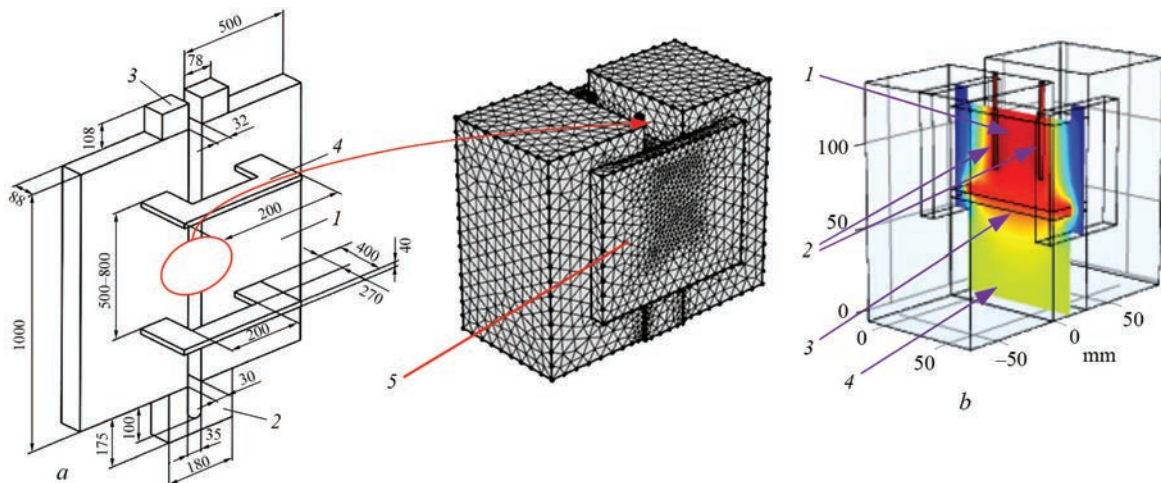


Figure 2. Scheme of assembly of a vertical weld for ESW and finite element model of a fragment of the welding zone (*a*): 1 — item; 2 — inlet pocket; 3 — run-off tap; 4 — cramp; 5 — shoe. Fragment of a graphical model in a section (*b*): 1 — slag pool; 2 — electrodes; 3 — metal pool; 4 — weld

mathematical modeling was performed on graphical 3D model of a zone of the item region (Figure 2, *a*), which includes the edges of the metal being welded at the depth of 70 mm from both sides, at ~140 mm height, which is adjustable (depending on the specified depth of the slag pool, calculated depth of the metal pool and weld height) and item thickness which is assigned, ~80 mm.

Proceeding from the postulates of the theory of similarity [8], a geometrical model was constructed, which allows for the similarity of its geometrical parameters to those of the physical model. The main condition for modeling was such as to ensure the best correspondence of the geometrical part of the model to the geometrical parameters of the physical experiment, at application of the physical properties of the

materials of the slag, item being welded and electrodes [9] (Table 2).

$C_p[T]$, $\rho[T]$, $k[T]$, $\alpha[T]$, $\sigma_{st}[T]$, $\sigma_{sh}[T]$, parameters were assigned by the respective approximating dependencies (not given in the paper) on temperature T , K. Graphical parameters of the model taken as the base were as follows: $S = 80$ mm, $b = 30$ mm, $h_m = 50$ mm, $d_{el} = 3$ mm, $L1 = 10$ mm.

Slag pool heating occurs due to resistive heat of electric current evolving at current flowing through it. The distribution of the electric field, current and potential in the slag pool, item being welded, and the shoes, as well as heat distribution in the volume of the examined zone was studied using its finite element model (Figure 2), consisting of the slag and metal pools, two shoes, two electrodes immersed into the slag pool, as well as fragments of the item and the weld.

Table 1. Data on ESW technological mode

Pass	Welding process	Welding current I , A	Power source voltage U , V	Kind of current	Welding speed v_w , m/h	Electrode wire feed rate v_p , m/h
1	ESW	880–960	38–40	Alt.	1.0	190–210

Table 2. Physical properties of materials used in the model

Parameter	Item	Electrodes	Slag	Shoes	Weld
Heat capacity C_p , J/(kg·K)	$C_p[T]$	$C_p[T]$	1400	385	$C_p[T]$
Relative dielectric permeability ε	1	1	2.5	1	1
Density ρ , kg/m ³	$\rho[T]$	$\rho[T]$	2600	8960	$\rho[T]$
Heat conductivity k , W/(m·K)	$k[T]$	$k[T]$	295	400	$k[T]$
Coefficient of thermal expansion α , 1/K	$\alpha[T]$	$\alpha[T]$	–	17E-6	$\alpha[T]$
Specific electric conductivity σ , S	$\sigma_{st}[T]$	$\sigma_{st}[T]$	$\sigma_{sh}[T]$	6E7	$\sigma_{st}[T]$

The model solves the following equations:

$$\rho(T)C_p \frac{\partial T}{\partial t} + \nabla q = Q$$

where $q = -k(T)\nabla T$; Q is the additional heat source (a heated metal pool can be an additional heat source).

When working with stationary electric currents in a medium, which is a conductor, the stationary equation of continuity should be taken into account. In a stationary system of coordinates the point form of Ohm's law indicates that:

$$J = \sigma(T)E,$$

where J is the current density; E is the electric field intensity.

The static form of the continuity equation requires that:

$$\nabla J = -\nabla \sigma(T)\nabla U = 0,$$

where U is the voltage.

After model validation by the results of experimental ESW, the following computation data were obtained at $U = 40$ V; $v_f = 200$ m/h:

- total electrode current $I = 922$ A;
- SP conductivity $\sigma = 11.82$ S;
- welding speed of 1.07 m/h.

Such a result practically confirms the correctness of the selected physical and graphical parameters of the model, and enables its application in the planned mathematical experiments. In connection with the fact that model switching from the monofilar to the bifilar power circuit does not change either the physical, or the graphical parameters of the model proper, but changes only the outer power circuits, we assume that the obtained model parameters are also applicable to the model of ESW with a bifilar power circuit.

In the model a stationary problem is solved, and the results of a steady-state process are derived. The model allows determination of the potential, current density and temperature in each point of the studied zone volume at different variations (within ± 20 %) of electrode diameter, item thickness, gap width, slag pool depth, as well as electrode immersion depth (within 5–95 % of h_{sl}) and electrode location relative to the shoes (within 10–90 % of $S/2$).

Mathematical experiment results were used to derive the dependence of specific conductivity of the slag on temperature for each elementary volume of SP. Calculation of the depth of electrode immersion l_{im} in SP (at $h_{sl} = 50$ mm), as well as average temperature of metal pool surface T_{MP} , depending on U and v_f , was performed. Electrode immersion was determined by the results of calculation of the temperature of the electrode lower edge, which reached that of electrode melting (1500 °C).

Figure 3, *a* shows the dependence of SP conductivity σ on U at unchanged $v_f = 280$ m/h and $L1 = 20$ mm. SP conductivity at bifilar EBW and equality of consumed power with the monofilar ESW, is always approximately 4 times smaller than that for monofilar variant. The dependence is of an extreme nature. σ maximum is observed at $U = 50$ V for bifilar ESW and at $U = 25$ V for the monofilar ESW, respectively.

Figure 3, *b* gives the dependence of I on U . At bifilar ESW the current is always lower, compared to its value with the monofilar circuit, in connection with doubled value of voltage for ESW bifilar circuit. This factor ensures a reduction of energy losses in a short power circuit. Both the dependencies are of an extreme type with a maximum of approximately 480 A at 80 V for bifilar circuit and of approximately 940 A at 40 V for the monofilar circuit.

Figure 3, *c* gives the dependence of ESW consumed power, reduced to a unit of SP volume, on source voltage, U . Both the dependencies are extreme. At the same productivity of ESW for both the power source connection circuits, the consumed power of the process is practically identical.

Presence of extremums of $\sigma(U)$, $I(U)$ and $P_f(U)$ functions should be used, allowing for optimization of welded joint quality characteristics.

Figure 4 shows the dependencies of SP conductivity, power source current and the reduced consumed power on v_f at $U = 100$ V for the bifilar circuit and $U = 50$ V for ESW monofilar power circuit. For all the three dependencies an increase of their values with higher feed rate is observed. The given consumed power of the process is practically the same.

At unchanged low welding voltage and increasing electrode feed rate, the electrode tip moving closer

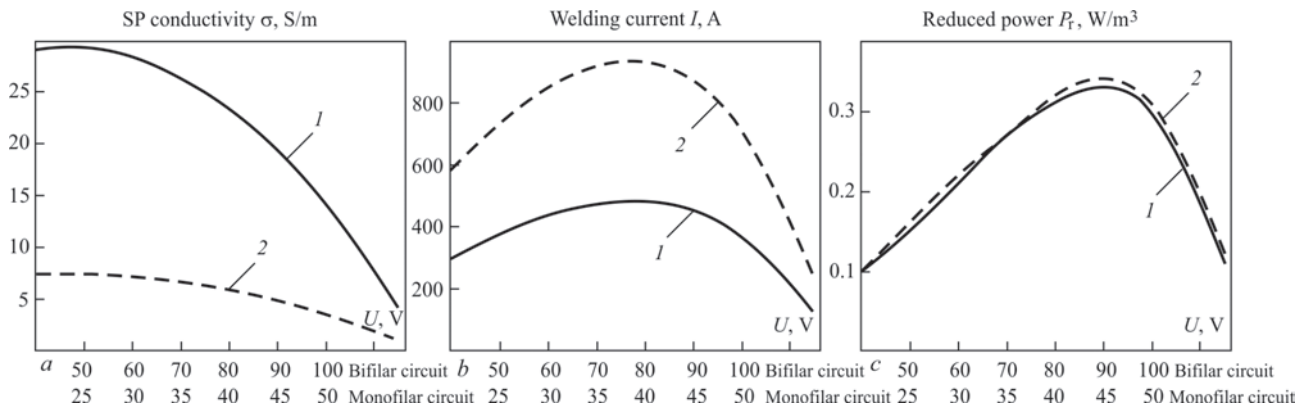


Figure 3. Dependence on voltage U of: a — SP conductivity σ ; b — welding current I ; c — power P_r reduced to a unit of slag pool volume, for ESW bifilar and monofilar circuits at unchanged $v_f = 280$ m/h and $L1 = 20$ mm (1 — ESW bifilar circuit; 2 — monofilar circuit)

to the metal pool, increase of power source current and of the consumed power reduced to SP volume, are usually observed. A reverse process should be observed at lowering of the feed rate. At constant feed rate (for instance, $v_f = 280$ m/h) and lowering of voltage (for instance, from 80 to 60 V for ESW bifilar circuit or from 40 to 30 V for the monofilar circuit), this regularity becomes reversible (Figure 3, b).

Thus, to ensure the set feed rate, at voltage lowering the current should be increased due to deeper immersion of the electrode into SP and reduction of the resistance of the spacing between the electrode and the metal pool. At lowering of the electrodes closer to the metal pool, however, i.e. to the additional heat source, their melting rate becomes higher, while equalizing of the feed rate and linear melting rate occurs without any significant increase of current. This is related to superposition of heat from resistive heating and external heat from the metal pool. Current here decreases and input power is reduced, whereas the melting rate is temporarily stabilized. With time, the thermal level in this zone drops, in connection with reduction of input power (Figure 3, c) and electrode immersion becomes deeper. Further lowering of SP temperature may lead to disturbance of ESW stability.

Figure 5 gives the dependencies of SP conductivity, power source current and reduced consumed power on the change of the width of the item gap at unchanged values $S = 80$ mm, $h_{sl} = 50$ mm, $v_f = 280$ m/h, $L1 = 20$ mm, $d_{el} = 3$ mm, $U = 80$ V for ESW bifilar circuit and $U = 40$ V for ESW monofilar power circuit.

At increase of the gap width from 20 up to 45 mm, a reduction of SP conductivity (Figure 5, a), lowering of power source current (Figure 5, b) and decrease of power (Figure 5, c), reduced to a unit of SP volume is observed for both ESW power circuits. This is related to the electrodes moving away from the item. Power (Figure 5, c), reduced to a unit of SP volume, practically does not differ for both the power circuits under other equal and unchanged conditions.

Figure 6 gives the dependence of conductivity (Figure 6, a), power source current (Figure 6, b) and reduced power (Figure 6, c) on $L1$. These conditions of the computational experiment are identical to those for Figure 5. At $L1$ increase from 5 to 15 mm a slight decrease in conductivity is observed for both the connection circuits, because of the electrode moving farther from the shoes, which are in direct contact with the item. At $L1$ increase from 15 to 25 mm, a slight increase of conductivity is noted for both the connection circuits, due to electrodes of different polarity moving

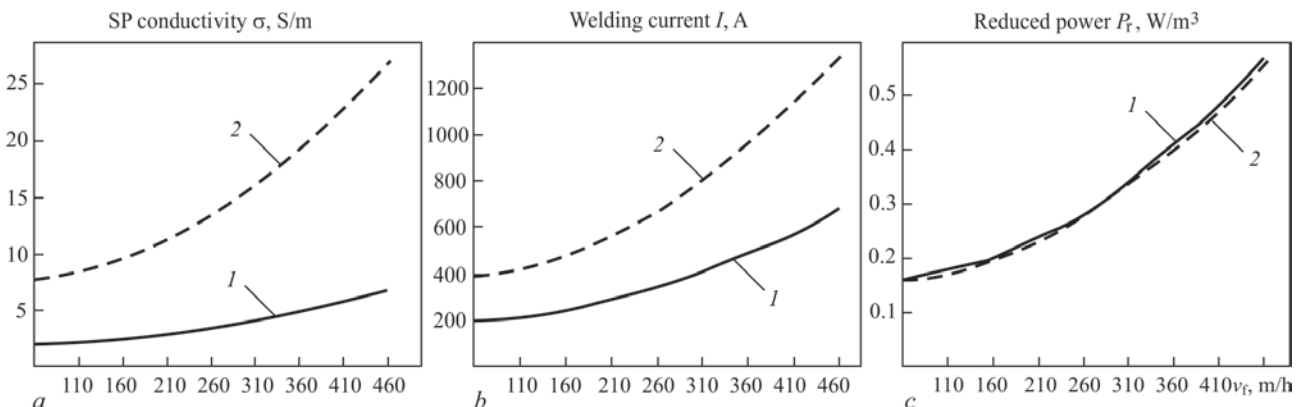


Figure 4. Dependence on electrode feed rate v_f of: a — SP conductivity σ ; b — welding current I ; c — power P_r reduced to a unit of slag pool volume for ESW bifilar (1) and monofilar circuits (2)

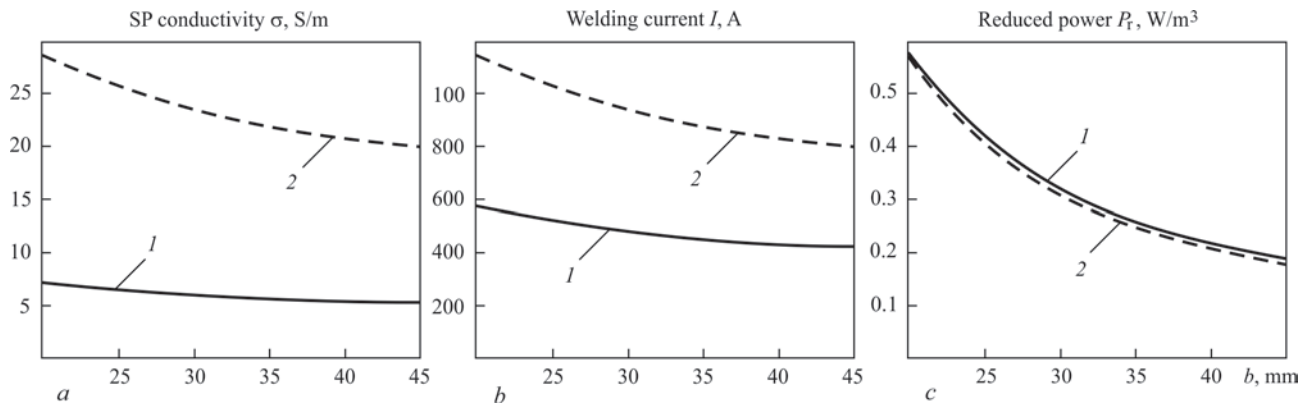


Figure 5. Dependence on welding gap b of: a — SP conductivity σ ; b — welding current I ; c — power P_r reduced to a unit of slag pool volume, for ESW bifilar (1) and monofilar circuits (2)

closer to each other (bifilar circuit) and increase of the slag electrically conducting space (monofilar circuit). At L_1 increase from 25 to 38 mm, an abrupt increase of conductivity is observed for the bifilar circuit, due to reduction of the distance between electrodes of different polarity and an abrupt lowering of conductivity for the monofilar connection circuit. The latter is related to the fact that the thermal level of SP between the electrodes is increased due to superposition of thermal fields of each of the electrodes. Here the radial component of electrode melting rates becomes greater, electrode immersion becomes smaller to equalize the electrode feed and melting rates, and this, in its turn, leads to current lowering. With bifilar power circuit the electrodes drawing closer together leads to lowering of the resistance between them. The current rises abruptly, thus increasing the radial melting rate, which leads to reduction of electrode immersion. Such a mode may result in one of the electrodes moving out of the slag space. Current changes (Figure 6, b) for both the source connection circuits, are of a similar nature. The reduced powers (Figure 6, c) for both the circuits practically do not differ at L_1 increase from 5 to 20 mm. At L_1 increase from 20 to 38 mm the reduced power in bifilar circuit rises abruptly, and in monofilar circuit it drops abruptly. It is obvious that the electrodes should not be

removed from the shoes for more than 20 mm distance, probably $L_1 = L/4$.

Figure 7 gives the dependencies of temperature distribution in SP between the middles of the wet portions of both the electrodes at different values of distance L_{el} between them. A comparison of these distributions for both the power circuits was made. One can see from these dependencies that at distance $L_{el} > 27$ mm the SP thermal level between the electrodes is practically the same for both the circuits, i.e. the advantage associated with controlling the item edge penetration by just the voltage in bifilar circuit compared to the monofilar power circuit [1], at ESW is confirmed only at certain electrode spacings.

One of the parameters at ESW modeling, required for controlling the process, which is difficult to measure in real time, is the electrode immersion depth. SP heat, which is the main source for melting at ESW, should be used in the most rational way, both for electrode melting, surface melting of item edges, required interaction of the molten filler metal with the heated slag on the path from the electrodes to the metal pool, and for maintaining the required thermal level and uniformity of metal pool heating. In this connection, for bifilar power circuit particularly important is maintaining the electrode immersion depth at the required level, considering that the heat is mainly concentrated between the electrodes (provided

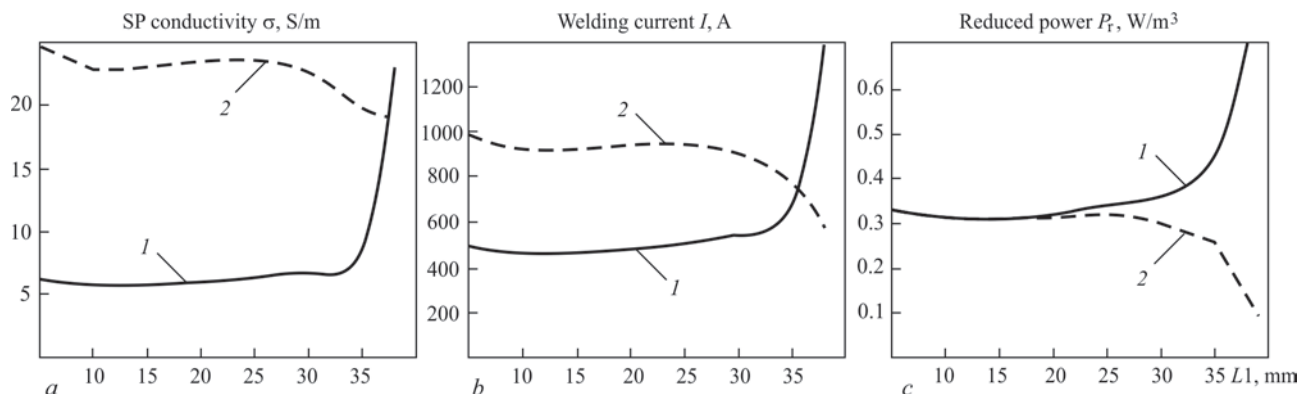


Figure 6. Dependence on the distance between the electrode and shoe L_1 of: a — SP conductivity σ ; b — welding current I ; c — power P_r reduced to a unit of slag pool volume, for ESW bifilar and monofilar circuits

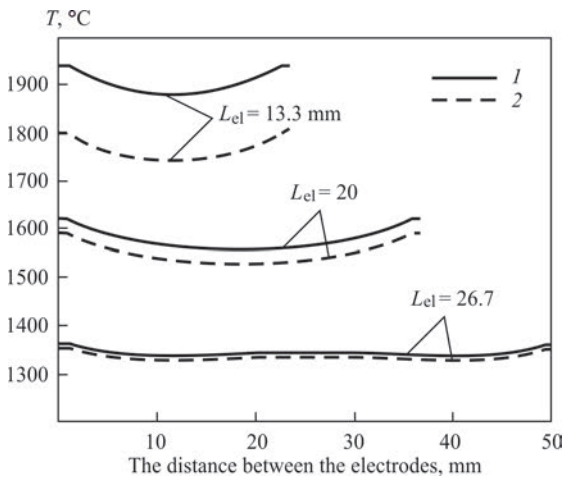


Figure 7. Temperature distribution between the middles of electrode wet parts for both the ESW power connection circuits: 1 — bifilar; 2 — monofilar

the distance between them is sufficient). Figure 8 gives the nomogram of distribution of electrode immersion depth l_{im} , depending on U and v_f , plotted by the results of mathematical experiment on the model and calculation of the temperature of the electrode lower edge until its specified melting temperature has been reached.

The metal pool thermal level is maintained owing to heat and mass exchange between the molten filler metal and the slag pool. Due to convection, the hotter slag conglomerates float upwards, driving the colder ones downwards. As a result of the impact of the gravitational forces the heavier higher-density conglomerates sink to the bottom. As the slag conglomerates move in the magnetic field of electric current, flowing in the electrodes and in SP, through charged ion particles in a certain direction, as well as molten metal drops, moving downwards under the action of gravitational forces, the Ampere electrodynamic force is applied to them.

With the monofilar power circuit, if dc current sources are used, the descending metal drops under

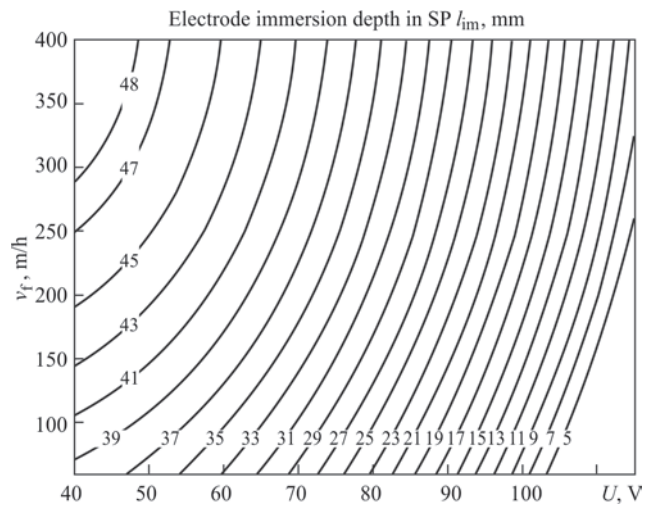


Figure 8. Nomogram of distribution of electrode immersion depth in SP l_{im} at different combinations of U and v_f values for ESW bifilar circuit

the impact of Ampere force will fall closer to the metal pool middle, or will shift to the sides from the metal pool middle, depending on the unit connection polarity. With the bifilar power circuit, if dc current sources are used, the drops will shift from each of the electrodes to the left or to the right, depending on the polarity of the connected power source. At application of ac power source, the drops will descend vertically down along the electrodes, irrespective of whether monofilar or bifilar power circuit is used.

In view the above, the electrode immersion depth with bifilar power circuit should be somewhat increased to ensure the heat balance between SP top and bottom.

Figure 9 shows the nomogram of distribution of the weld form factor ψ , depending on U and v_f . The mathematical experiment was conducted at $S = 80$ mm, $b = 30$ mm, $h_{sl} = 50$ mm, $L1 = 20$ mm, $d_{el} = 3$ mm.

The best values of the weld form factor are derived at low electrode feed rates and high voltage of the

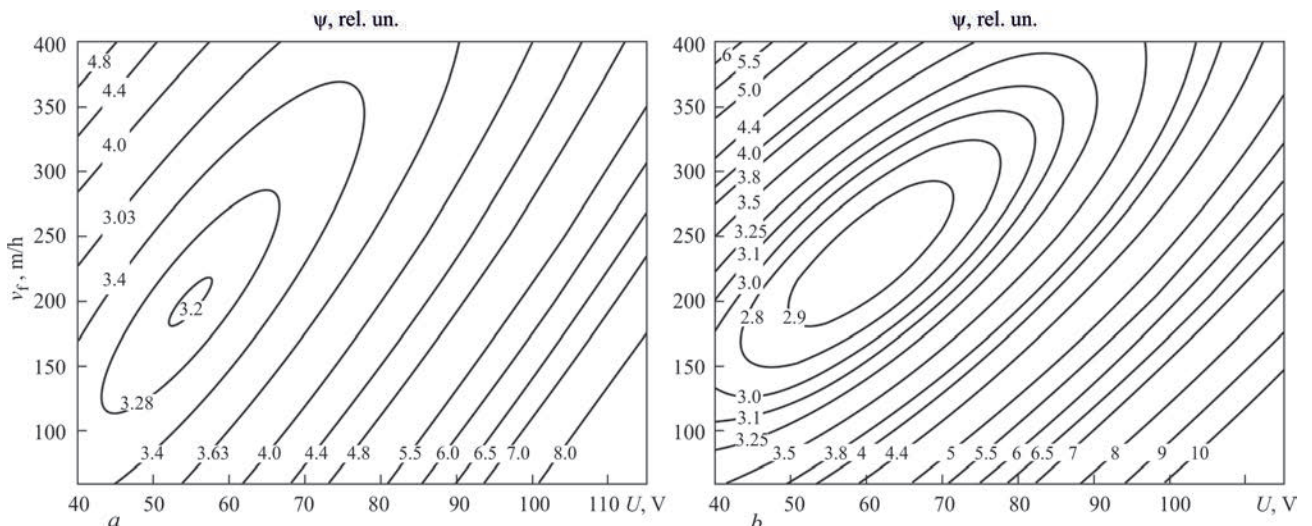


Figure 9. Distribution of values of weld form factor ψ , depending on common values of U and v_f for ESW bifilar (a) and monofilar (b) power circuits

power source. So, for instance, at $v_f = 300$ m/h and $U = 115$ V for bifilar power circuit $\psi = 6$ and for monofilar circuit $\psi = 5.7$, i.e. the zone of the modes with a high value of ψ factor is much wider for the bifilar circuit, which allows a more reliable maintenance of the mode with a high weld form factor, and directing the heat flows towards enhancement of the capability for weld surface formation and penetration of the edges being welded.

CONCLUSIONS

1. Searching for slag pool thermophysical parameters, as additional components of ESW model was performed, taking into account the nonuniform temperature distribution in the slag pool, as well as allowing for the influence of the temperature of water-cooled shoes on temperature distribution in the item, and slag and metal pool in the near-boundary regions.

2. Models of ESW with a bifilar and monofilar power circuits were used to perform preliminary comparative study of the regularity of conductivity change in the slag pool at the change of the slag pool geometrical parameters, as well as coordinates of the points and depths of electrode immersion.

3. The advantage associated with controlling the item edge penetration only by voltage with bifilar circuit compared to monofilar power circuit, is confirmed only at certain electrode spacings.

4. The regularity of the change of electrode immersion depth, depending on voltage and electrode feed rate, was studied. It is shown that at electrode edge location near the metal pool, a reduction of electrode immersion depth and of consumed electric power is observed due to superposition of the heat, generated by current flowing in SP, and the MP heat. The resulting heat is sufficient to ensure the required electrode melting rate. However, in connection with the reduction of heat, generated by electric power, in the specified mode, a gradual lowering of the thermal level of ESW process is observed, which may lead to its destabilization.

5. In the general case, the zone of the modes with a high value of weld form factor is much wider for the bifilar circuit than for the monofilar one, which allows a more reliable maintenance of the mode with a rather high weld form factor and directing the heat flows towards enhancement of the capability for weld surface formation and penetration of the edges of items being welded.

REFERENCES

1. Medovar, B.I., Stupak, L.M., Bojko, G.A. et al. (1976) Electroslag furnaces. Ed. by B.E. Paton, B.I. Medovar. Kiev, Naukova Dumka [in Russian].
2. Jing, Xie (2008) Structure advantage of a 5-t double pole series circuit electroslag furnace. *Heavy Casting and Forging*, 5(3), 43–45 [in Chinese].
3. Xi-min, Zang, Tian-yu, Qiu, Xin, Deng et al. (2015) Industrial test of a 6-m long bearing steel ingot by electroslag remelting with drawing process. *China Foundry*, 12(3), 202–207.
4. Tezuka, M., Yamamoto, S., Takahashi, F. et al. (2014) Internal quality of 2150 mm diameter ingot manufactured using new 150-ton ESR furnace. In: *Proc. of 19th Int. Forgemasters Meeting (IFM)*. (Tokyo, Japan, 29.09–03.10), 90–94.
5. Son, I., Lee, W., Sim, Kw. et al. (2014) Installation of 150-ton new ESR facility and production of 120-ton ESR ingot for 12Cr HIP rotor forgings. *Ibid.*, 333–337.
6. Kubin, M., Scheriau, A., Knabl, M. et al. (2013) Operational experience of large sized ESR plants and attainable quality of ESR ingots with diameter of up to 2600 mm. In: *Proc. of the Int. Symp. on Liquid Metal Processing & Casting (LMPC)* (Austin, Texas, USA, 22–25 September), 57–64.
7. Lankin, Yu.N., Moskalenko, A.A., Tyukalov, V.G. et al. (2008) Application of electroslag welding in construction and in repair of metallurgical assemblies. *Svarshchik*, 1, 6–9 [in Russian].
8. Gukhman, A.A. (1973) *Introduction to similarity theory*. 2nd Ed. Moscow, Vysshaya Shkola [in Russian].
9. Sorokin, V.G., Volosnikova, A.V., Vyatkin, S.S. et al. (1989) *Grades of steels and alloys*. Ed. by V.G. Sorokin. Moscow, Mashinostroenie [in Russian].

ORCID

Yu.M. Lankin: 0000-0001-6306-8086,
V.G. Soloviov: 0000-0002-1454-7520,
V.G. Tyukalov: 0000-0003-3491-193X,
I.Yu. Romanova: 0000-0001-7154-1830

CONFLICT OF INTEREST

The Authors declare no conflict of interest

CORRESPONDING AUTHOR

Yu.M. Lankin

E.O. Paton Electric Welding Institute of the NASU
11 Kazymyr Malevych Str., 03150, Kyiv, Ukraine
E-mail: lankin.y.n@gmail.com

SUGGESTED CITATION

Yu.M. Lankin, V.G. Soloviov, V.G. Tyukalov, I.Yu. Romanova (2021) Comparison of the processes of electroslag welding at power connection by mono- and bifilar circuits. *The Paton Welding J.*, 11, 22–28. <https://doi.org/10.37434/tpwj2021.11.04>

JOURNAL HOME PAGE

<https://pwj.com.ua/en>

Received 13.09.2021
Accepted: 29.11.2021

<https://doi.org/10.37434/tpwj2021.11.05>

INVESTIGATION OF THE CAUSES FOR APPEARANCE OF DEFECTS IN WELDED BUTT JOINTS OF TRAM RAILS MADE BY THERMIT WELDING

E. Turyk¹, I.O. Ryabtsev², M. Lomozik¹, K. Krasnovskyi¹

¹Lucasiewicz Research Network-Institute of Welding
44-100, Gliwice, 16-18 Bl. Czeslava, Poland. E-mail: is@is.gliwice.pl

²E.O. Paton Electric Welding Institute of the NASU
11 Kazymyr Malevych Str., 03150, Kyiv, Ukraine

ABSTRACT

The results of investigations of the causes for fatigue fracture of rail butt joints on two new tram tracks, made by thermit welding by two organizations are presented. Control analysis of the chemical composition and mechanical properties of the rail material; analysis of the chemical composition of the welds, macro- and microscopic investigations of the weld, HAZ and base metal, and hardness studies in these zones were performed. It was found that pore accumulation and isolated microcracks in the metal of welds are the potential cause for cracking. Violations of the technological process of thermit welding of the tram tracks were determined, which lead to appearance of these defects. The detected defects are the result of the following factors, associated with failure to meet the standard requirements on thermit welding of tram tracks and of the system of ensuring the quality of welding operations, namely violation of welding technology and insufficient control at the respective stages of the production process.

KEY WORDS: thermit welding, tram tracks, fatigue cracks, porosity; microcracks, quality assurance system

INTRODUCTION

Requirements for thermit welding of rails on tram routes and certification of the procedure of thermit welding of tram rails are regulated by the European standard PN-EN 16771:2017-01 [1], and requirements to the chemical composition of the metal of thermit welds are given in the standard PN-EN 14730-1:2017-06 [2]. Additionally, it is recommended that the performer of works complied with the requirements to the quality of welding performance according to the standard EN ISO 3834-2 [3]. Compliance with these requirements allows providing the required quality of butt joints and their life, which is confirmed by many years of experience of operation of the continuous railways, performed by thermit welding.

Recently, in Poland a problem of fatigue fracture of butt joints of new tram tracks, made by thermit welding, appeared which is confirmed by publications on different sites. In this article, two cases of break-

age of rails on the tram lines, built by two organizations were considered. On the tram route "A" after three months of operation, cracks of fatigue type in welded butt joints of grooved rails 60R2 (Tv-60) from steel R260, made by thermit welding, by the first organization were detected. On one section of the tram route from approximately 1000 welded butt joints, 32 were fractured. On the tram route "B", similar cracks were found in 90 welded butt joints from 150. Thermit welding of rails on this route was performed by a second organization.

Cracks that led to fracture of the rails, initially propagated across the welded butt joint approximately at a half of the height of the rail web (Figure 1, *a*). The length of the cracks reached 20 cm. Then the cracks changed the direction by 90° towards the head and the flange of the rail and a complete fracture of the butt joint occurred (Figure 1, *b*).

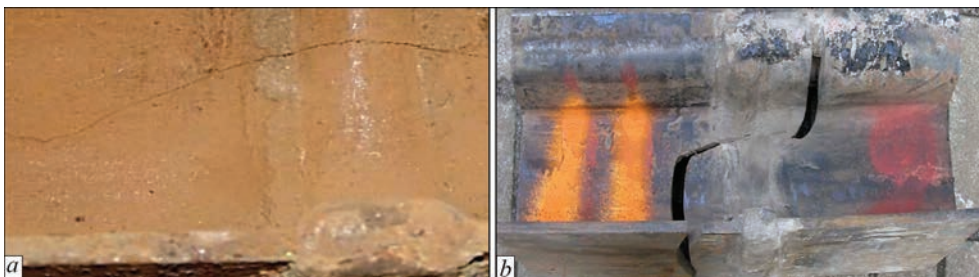


Figure 1. Initial crack (*a*) and nature of fracture of tram rails in the zone of welded butt joint (*b*)

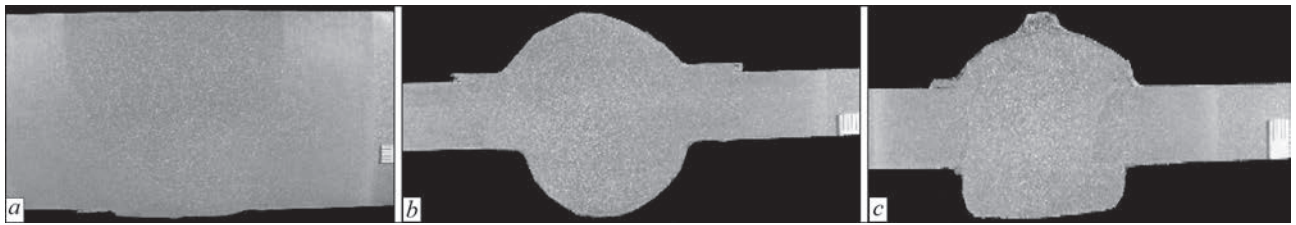


Figure 2. Macrostructure of welded butt joint in the zone of head (*a*), web (*b*) and flange (*c*) of rails

The aim of this work was to determine the defects of welding, which may be the cause of fatigue cracking in the welded butt joints of the tram rails and determine the technological operations, during which violation of the modes of thermit welding probably occurred.

INVESTIGATION OF THE CAUSES OF CRACKING IN WELDED BUTT JOINTS OF THE TRAM ROUTE “A”

The next volume of tests was agreed to determine welding defects that can be a potential cause of fatigue cracks in two welded butt joints C1 and C2 of the rails of the route “A”:

- control analysis of the chemical composition and mechanical properties of the material of rails — weld-

ed butt joints No. C1 (rails Nos 1 and 2) and No. C2 (rails Nos 3 and 4);

- control analysis of the chemical composition of welds, made by thermit welding;

- metallographic examinations and study of distribution of hardness of weld, HAZ and base metal;

- metallographic examinations and study of distribution of hardness outside the area of fracture in the area of the flange and head of rails.

The analysis of the chemical composition of the material of rails Nos 1–4 was carried out in an optical emission spectrometer Q4 Tasman of Bruker Company. It was established that the chemical composition of the rails meets the requirements of the standard EN 14811:2019 [4]. Tensile strength $\sigma_t = 911.3$ –

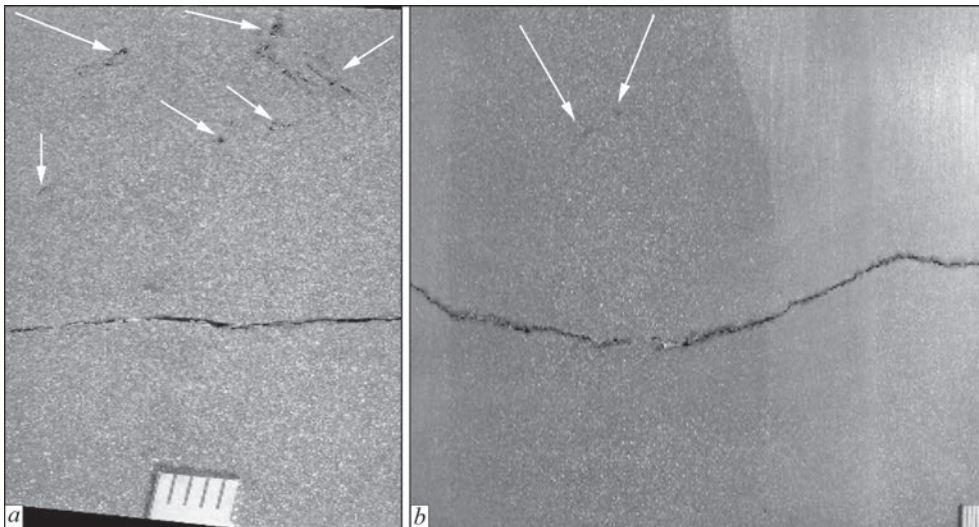


Figure 3. Macrostructure of welded butt joints C1 (*a*) and C2 (*b*) in the crack zone (arrows mark accumulation of gas pores)

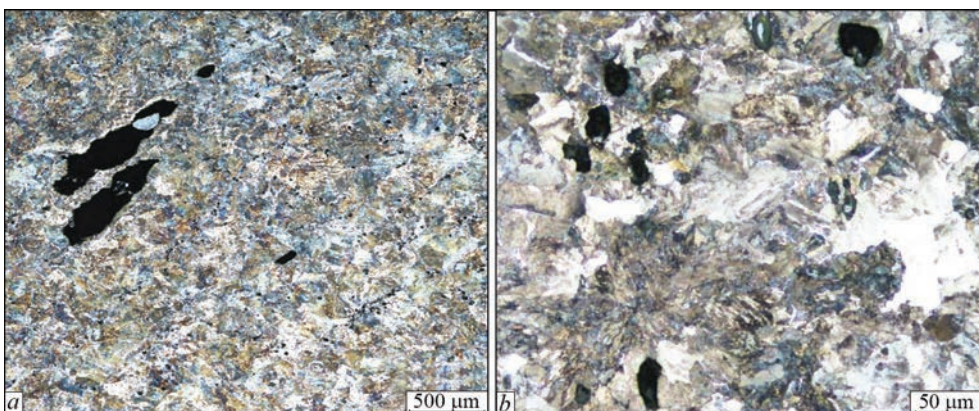


Figure 4. Microstructure of welded butt joints C1 (*a*) and C2 (*b*) in the crack zone. Pores in welds.



Figure 5. Microstructure of welded butt joint C1 in the crack zone 991.6 MPa and relative elongation $\delta_5 = 13.0\text{--}16.3\%$ of the material of the rails Nos 1–4 also meet the requirements of the standard for steel R260: $\sigma_t \geq 880$ MPa, $\delta_5 \geq 10\%$. Analysis of the chemical composition of welded butt joints C1 and C2, performed using thermit method, showed that the content of alloying elements in the welds also meets the requirements of the standard PN-EN 14730-1:2017-06 [2]. Examination of macrostructure of the welded butt joints in the area of the head, web and flange of the rails did not reveal defects of welding in the form of lacks of fusion, lacks of penetration and slag inclusions (Figure 2, *a–c*).

However, in the welded butt joints C1 and C2 in the fracture zone, the accumulation of tiny pores were detected (Figure 3).

Porosity of the welds was confirmed by microscopic examinations (Figure 4). The cause for pore formation is reduction in the solubility of gases at a decrease in temperature. Too fast cooling of the welded butt joint increases the probability, that bubbles of gases may not have time to come to the surface and pores will be formed.

Examinations of microstructure showed that the material of the rails has a pearlite-bainite structure with a small amount of ferrite. An unfavourable martensitic structure in HAZ was not detected. The study of hardness confirmed this fact: hardness of HAZ did not exceed *HV* 325.

In the weld of the butt joint C1 in the area of the rail web, single microcracks were detected throughout the grain boundaries, that occur at a considerable distance from the main crack (Figure 5).

Microcracks, apparently, are the result of the exposure to tensile stresses that cause plastic deformation of the weld metal. Microcracking is caused by the appearance of liquid films of easy-melting eutectic on grain boundaries, which have a solidification temperature much lower than the solidification temperature of iron.

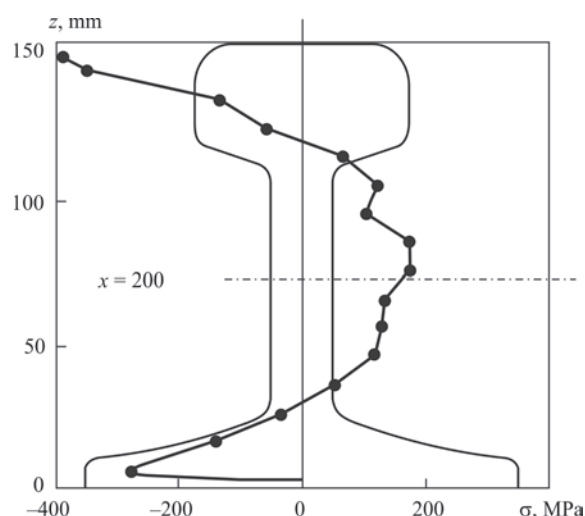


Figure 6. Distribution of residual stresses in the butt joint of rails made by thermit welding [5]

Gas pores and microcracks in the welded butt joints C1 and C2 of the tram route “A” contribute to arising of fatigue cracks that were formed in the web of the rails in the zone of the highest residual tensile stresses (Figure 6).

INVESTIGATION OF THE CAUSES OF CRACKING IN WELDED BUTT JOINTS OF THE TRAM ROUTE “B”

The subject of the study was two fractured butt joints No. I and No. II of the tram rails 60R2, made by the SRZ method [6]. The tests of mechanical properties showed that the material of the rails does not meet the requirements of PN-EN 14811:2019-06 concerning the minimum elongation for steel R260, and tensile strength, yield strength and relative elongation significantly differ from the data in the act on the results of the acceptance tests 3.1 according to EN 10204:2017. [7].

The use of a low-quality material of the rails with reduced plastic properties indicates insufficient control before welding, which does not meet the requirements of EN ISO 3834-2:2019, item 14.2.

Insufficient control before welding confirms also the lack of qualification certificates of welders of thermit welding of tram rails using SRZ method. The certificates of the qualification of welders of thermit welding of railway rails by the welding method SoWoS [9, 10] without reinforcement, with the upper preheating of remnants of rails and with the SkV method [11, 12] with a short preheating time were presented according to PN 14730-2:2006 [8]. This does not meet the requirements of EN ISO 3834-2:2019, item 7.2.

Metallographic examinations revealed accumulation of pores in the welds of the butt joints I and II in the area of head and flange of the rails (Figure 7).

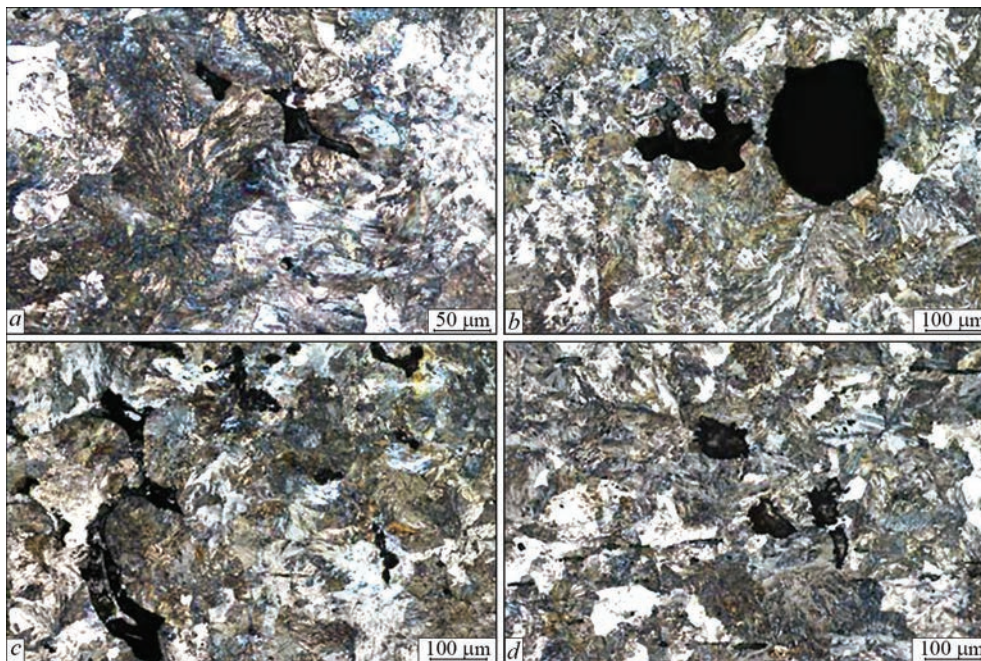


Figure 7. Gas pores in the head (*a, c*) and in the flange (*b, d*) of rails of welded butt joints I and II, respectively

As a result of examinations, the probable causes of premature fatigue fracture of welded butt joints of rails of the tram route “B” were established:

a) use of rails material, which does not correspond to the technical requirements of the standards, with reduced plastic properties;

b) violation of the technology of thermit welding, as a result of which in the metal of rail welds, microcracks and accumulation of gas pores in their zone were revealed;

c) insufficient technical supervision of the technology of rails welding, which is evidenced by:

- incomplete operating charts of welding WPS (temperature and time of preheating, height of the torch above the rail head, time from the end of pouring the thermit melt into the mould to chipping of the excess metal from the upper part of the rail head and over the radius parts are not indicated);
- lack of qualification certificates of welders of thermit welding of tram rails using SRZ method.

CONCLUSIONS

1. In the metal of the welded butt joints of the rails C1 and C2 of the route “A”, welding defects in the form of accumulations of gas pores were revealed, which are formed as a result of quite rapid cooling of weld metal. Porosity was also detected in the welded joints I and II of the route “B”.

2. In the welded butt joint C1 of the route “A” on the area of the rail web, inadmissible welding defects in the form of single microcracks throughout the grain boundaries were revealed.

3. The appearance of gas pores and microcracks is associated with the following violations of the technological process of thermit welding of tram rails:

- low temperature and short time of preheating of rail ends;
- nonuniform heating of welding ends of the rails; underestimated gap recommended between the ends of rails before welding;
- rapid cooling of weld metal as a result of preliminary removal of the forming device (too short time from the moment of metal tapping from the crucible to removal of the forming device).

4. The found defects are the result of two factors associated with noncompliance of the performers with the requirements of the standard on thermit welding of tram rails and systems of quality assurance of welding works:

- violations of welding technology;
- insufficient control at the corresponding stages of the production process: incomplete operating charts of welding WPS, absence of qualification certificates of welders of thermit welding of tram rails by the SRZ method, and in the case of a tram route “B”, also absence of material of rails, which does not corresponds to the specification.

5. The found defects of welding (gas pores and microcracks) are a potential cause of fatigue cracks in the welded butt joints of tram rails during operation.

REFERENCES

1. PN-EN 16771:2017-01: *Railway applications — Infrastructure — Aluminothermic welding of grooved rails.*
2. PN-EN 14730-1:2017-06: *Railway applications — Track — Aluminothermic welding of rails, Pt 1: Approval of welding processes.*

3. DSTU EN ISO 3834-2:2019: *Quality requirements for fusion welding of metallic materials*, Pt 2: Comprehensive quality requirements
4. PN-EN 14811:2019-06: *Railway applications. Track. Special purpose rail. Grooved rails and associated construction profiles*.
5. Lawrence, F.V., Chen, Y-R., Cyre, J.P. (2014) *Improving the fatigue resistance of thermit railroad rail weldments*. <http://fcp.mechse.illinois.edu/files/2014/07/Lawrence-presentation.pdf>
6. *Thermit SRZ/SRZ L50/SRE welding process for grooved rails*. https://www.elektro-thermit.de/fileadmin/et/user_upload/PDF/Produktbrosch%C3%BCren/SRZ_SRE_DEF.pdf
7. DSTU EN 10204:2017: *Metallic products — Types of inspection documents*.
8. PN-EN 14730-2:2006: *Railway applications — Track — Aluminothermic welding of rails*, Pt 2: Qualification of aluminothermic welders, approval of contractors and acceptance of welds.
9. (2010) *Code of Practice for the THERMIT — Quick Welding Procedure SoWoS*. Elektro-Thermit GmbH & Co KG.
10. (2019) *Instrukcja spawania szyn termitem Id-5*. PKP Polskie Linie Kolejowe S.A.
11. *Code of Practice for the THERMIT — Quick Welding Procedure SkV*. Elektro-Thermit GmbH & Co KG, 2010. https://www.thermit.com.au/media-centre/technical-information/PI_8.5.1-296_TA_TS-Code-of-Practice-SkV-Elite-Welding-Procedure.pdf.
12. *Elektro-Thermit. Technology of aluminothermic welding of rails with short time of heating (SkV, SkV-L 50, SkV-L 75)*. <https://docplayer.com/27763010-Elektro-thermit-tehnologiya-alyuminotermitnoy-svarki-relsov-s-korotkim-vremenem-podogreva-skv-skv-l-50-skv-l-75.html>.

ORCID

I.O. Ryabtsev: 0000-0001-7180-7782

CONFLICT OF INTEREST

The Authors declare no conflict of interest

CORRESPONDING AUTHOR

I.O. Ryabtsev

E.O. Paton Electric Welding Institute of the NASU

11 Kazymyr Malevych Str., 03150, Kyiv, Ukraine

E-mail: ryabtsev39@gmail.com

SUGGESTED CITATION

E. Turyk, I.O. Ryabtsev, M. Lomozik, K. Krasnovskyi (2021) Investigation of the causes for appearance of defects in welded butt joints of tram rails made by thermit welding. *The Paton Welding J.*, **11**, 29–33. <https://doi.org/10.37434/tpwj2021.11.05>

JOURNAL HOME PAGE

<https://pwj.com.ua/en>

Received 16.09.2021

Accepted: 29.11.2021

<https://doi.org/10.37434/tpwj2021.11.06>

REQUIREMENTS TO TECHNICAL CHARACTERISTICS OF RESISTANCE MICROWELDING MACHINES

Yu.M. Lankin

E.O. Paton Electric Welding Institute of the NASU
11 Kazymyr Malevych Str., 03150, Kyiv, Ukraine

ABSTRACT

Welding of up to 0.5 mm thick parts is usually called microwelding. Resistance microwelding is widely applied in electronics and instrument-making. Thermal inertia of welded parts at resistance welding is proportional to the square of their thickness. As a result of low thermal inertia of the parts at microwelding, the change of their temperature is close to the change in time of welding current of 50 Hz industrial frequency. In order to eliminate the temperature ripple, resistance microwelding should be conducted by direct current pulses or high-frequency welding current. At microwelding, the initial part-part contact resistance is tens of times higher than that of the parts being welded. To reduce the initial splashes of molten metal and to stabilize the welded joint quality, the welding current should increase smoothly at microwelding.

KEY WORDS: resistance microwelding, similarity theory, thermal inertia, welding current frequency, typical welding modes

INTRODUCTION

Resistance welding is the most productive welding process, which covers up to 50 % of welded products in the total volume of all the welding processes [1]. Welding of up to 0.5 mm parts is usually called microwelding. It is widely applied in electronics and instrument-making in manufacture of automotive electronics, sensors, medical instruments, batteries and battery modules, electronic components as well as in manufacture of jewelry [2–4]. Microwelding is often used in assembly of quartz resonators, piezoelectric instruments, capacitors, standard and solid-state resonators, thermocouples, different heating modules, miniature vibro motor, thermobatteries, fuel assembly spacer grills, which operate in the nuclear reactor core, as well as at sealing of the cases of miniature instruments, membrane boxes, and bellows and at installation of electric devices. There are data [4, 5] on replacement of the soldering process in manufacture of electronic instrumentation and jewelry by resistance microwelding, which has a number of serious advantages over it: absence of solders or fluxes, higher electric characteristics of the produced joint, thermal and vibration resistance, minimum impact of temperature on the parts being joined, cleaner manufacturing conditions, etc.

In the majority of the cases the requirements made of the produced welded joint, are limited to the required strength. In welding critical parts, however, in addition to high guaranteed quality and reliability of the joints, it is also necessary to ensure their high repeatability and absence of splashing of molten metal particles. High repeatability is required in manufacture of complex products, when a large number

of welds are made, and the finished product quality largely depends on the quality of each of them [7, 8].

FEATURES OF RESISTANCE MICROWELDING

Microwelding has several features, which create additional problems in the technology and design of the equipment. The small thickness of the parts being welded is the cause for low thermal inertia of the spot welds. From the theory of similarity, the thermal inertia of the parts being welded should be proportional to the square of the part thickness. Nobody has performed experimental determination of the magnitude of this inertia, but the analytical solution for nonstationary heating of the spot weld by a source of complex-shaped current is rather complicated, even with considerable simplifying assumptions. Therefore, the inertia was evaluated by mathematical modeling.

At resistance spot microwelding the electrode diameter is much larger than the welded part thickness. It allows assuming that the main portion of welding current flows through a metal column of the diameter equal to that of the electrodes and of the height which is equal to the total thickness of the parts being welded. This simplifying assumption was used when performing modeling of the dynamics of heating by 50 Hz current of spot welds on low-carbon steel of different thickness in an analog computer [9]. While in the first approximation the welded product can be presented as a first order inertia link, the results of modeling the thermal time constants Q of the parts being welded in the thickness range $\delta = 1\text{--}0.2$ mm are readily described by equation $Q = 0.0578\delta^2$ s.

Thus, the calculated thermal time constant of the spot weld is approximately proportional to the square

of thickness of the metal being welded. As a result, for low-carbon steel at 50 Hz frequency of welding current the temperature ripple, caused by periodical change of welding current in time, are negligibly small in welded thicknesses above 2.5–2.0 mm. At thickness $\delta = 1.0$ mm the temperature ripple in the spot center is equal to $< 10\%$. In welding of small thicknesses, the spot weld temperature during its formation follows the change of welding current with a slight delay, the rear front of the current pulse actually does not participate in welding, and spot heating (formation) essentially depends on the welding current pulse shape.

The role of contact resistances as heat sources grows at the beginning of welding due to relatively small internal resistance of the parts, and small welding forces. So, based on calculations and experiments of V.E. Moravskiy [3] at reduction of the thickness of sheets from low-carbon steel 40 times (from 2.0 to 0.05 mm), the values of initial part-part contact resistances differs 170 times. In the general case, the ratio of contact resistances to internal resistance of the parts being welded is inversely proportional to their linear dimensions. For this reason, at contact microwelding the probability of initial splashes rises abruptly, making it supersensitive to the shape of the leading front of the welding current pulse.

FEATURES OF THE MODES OF RESISTANCE SPOT MICROWELDING

In welding metals of medium and large thicknesses at industrial frequency of welding current, considerable experience has been accumulated on stabilization of spot weld parameters by program and automatic regulation of process parameters during welding. This experience is almost not used in resistance spot microwelding, which is inferior to resistance welding of usual thicknesses, in terms of diversity of the welding modes and stability of welded joint quality. This is caused by a lack of fast-response welding power sources.

Welding of medium and large thicknesses is conducted in welding machines with alternating current of 50 Hz industrial frequency. In keeping with similarity criteria [10], the welding pulse duration is proportional to the square of welded metal thickness. Therefore, while in welding, for instance, of low-carbon steel 1 mm thick welding current time of 0.188 s is set on average, for welding of the same material 0.2 mm thick in a similar mode welding duration should be 0.023 s, whereas for material of 0.1 mm thickness it should just 0.009 s. In this case, it is practically impossible to regulate the welding time at 50 Hz mains frequency. More over, the welding current is also very hard to control.

In welding metals of medium and large thicknesses at industrial frequency, current regulation proceeds by changing the angle of the thyristor switching on. Therefore, after 120° phase of welding current, the spot weld temperature begins to drop following the current and the molten nugget stops growing. The second half-cycle of welding current is ineffective, as it does not lead to further increase of the molten nugget dimensions. Hence it follows that welding of steel of less than $0.2 + 0.2$ mm thickness at alternating current of industrial frequency is only possible by one half-cycle of the mains voltage, while the range of phase regulation is equal to $0-90^\circ$, calculated from the phase angle of voltage and current of the welding circuit.

For one-half-wave welding, in addition to controlling the current by adjustment of thyristor switching angle, a method was developed to control the current by regulation of the duration of thyristor on state [10, 11]. This is performed by forced blanking of the thyristor, when current has reached the specified value in its rise range.

Both in the first, and in the second case, it is impossible to control the form of the current pulse leading front. Because of all these causes, the so-called capacitor welding machines are used for welding small thicknesses in most cases [3].

Alongside the indubitable advantages, the capacitor welding machines are greatly inferior to alternating current machines as regards welding mode control, for multicycle welding. In capacitor welding machines it is extremely difficult to control the welding current pulse shape, and it is totally impossible to adjust the welding current during welding. Known are rather clumsy attempts to at least somehow change the natural shape of the capacitor discharge current, but all of them lead to an abrupt complication of the welding source, while the possibilities of controlling the pulse shape are extremely limited [3, 11].

Known are power sources with linear transistor regulators [6–8, 12]. They have ideal regulation characteristics, which allow realizing any welding cycles and automatically adjusting the welding parameters. Unfortunately, because of their cost and bulkiness, they will hardly become more or less widely applied, similar to the case of arc welding.

In principle, the resistance microwelding machines will not in any way differ from those for welding medium and large thicknesses at alternating current, if the condition of similarity is met [9]: welding current frequency $f = k_0 \delta^{-2}$, welding circuit impedance $Z_k = k_5 \delta^{-1}$ and machine mobile part mass $m = k_7 \delta^5$. However, at resistance microwelding the influence of relatively high initial contact resistance of the parts being welded is still in place. And this, in particular, is ex-

Table 1. Averaged recommended modes of spot resistance microwelding of low-carbon steels

δ , mm	\bar{d}_{el} , mm	\bar{F}_w , kg	\bar{I}_w , kA	\bar{t}_w , s	f , kHz	\bar{P}_w , kW	I_w^{\min} , kA	t_w^{\max} , s
1	2	3	4	5	6	7	8	9
0.05	1.15	12.7	2.2	0.0036	20.0	2.2	1.50	0.01
0.10	1.66	25.6	3.08	0.0090	5.00	3.08	2.09	0.026
0.15	2.05	36.2	3.74	0.0150	2.20	3.74	2.50	0.043
0.20	2.46	47.7	4.29	0.0224	1.25	4.29	2.90	0.065
0.25	2.68	59.0	4.78	0.0300	0.80	4.78	3.25	0.87

actly why expansion of the possibilities for regulation of the welding machine is required.

REQUIRED TECHNICAL CHARACTERISTICS OF AC RESISTANCE MICROWELDING MACHINES

In electronics and instrument-making resistance microwelding is used for welding products in the thickness range of 0.05–0.25 mm. We will extrapolate the data by the modes of welding medium and large thicknesses. The modes of welding low-carbon steel as the most common one are the most fully studied. Statistical treatment of all the accessible data bases of the modes of resistance welding of low-carbon steel in the thickness range $\delta = 0.5\text{--}7.3$ mm yielded the following dependencies for averaged welding modes:

$$\left. \begin{aligned} \bar{d}_e &= 5.5\delta^{0.526} \\ \bar{F}_w &= 222\delta^{0.956} \\ \bar{I}_w &= 9.264\delta^{0.478} \\ \bar{t}_w &= 0.188\delta^{1.32} \end{aligned} \right\} \quad (1)$$

Welding modes, calculated by (1) for thickness range of 0.05–0.25 mm are given in Table 1.

Table 1 gives the welding current frequencies, required for welding small thicknesses, at which the ripple of the spot temperature will be the same as in welding 1.0 + 1.0 mm thicknesses at 50 Hz frequency.

Analysis of Table 1 shows that welding at averaged modes requires rather high currents and source power. The seventh column shows the power, evolving in the spot weld at 1 V voltage in the spot, which, as is known, almost does not change with the change of the welded part thickness.

In practice, large thicknesses are welded at soft modes to lower the power, medium ones — at rigid modes to increase the productivity. Small thicknesses are also welded in soft modes, so as not to use the difficult-to-ensure short welding time, at which, as shown above, flexible current adjustment is not possible either. At welding at higher frequencies, increase of welding time for small thicknesses is no longer relevant, as the number of welding current cycles, which is increased with increase of frequency, is quite suf-

ficient for current adjustment. However, reduction of the required power of the welding source is highly important, as it simplifies the transistor high-frequency power generator.

Formulas (1) are given for average mode parameters. A weld spot of the same size can be obtained at different combinations of I_w and t_w . Processing of experimental mode data showed that the interrelation of current with welding time can be described by the following complex dependence:

$$I_w^2 t_w^{0.7} = 25.7\delta^{1.8}. \quad (2)$$

Scatter of experimental data around this regression line is much smaller than that for each of the components taken separately. In keeping with this dependence, welding current I_w decreases with increase of t_w , and vice versa. The variation limits of these parameters are restricted by the following: welding current can be increased with the respective reduction of the welding time, until splashing from under the electrode begins at the start of the current pulse; welding time can be increased with the respective decrease of welding current, until the dent from the electrode does not exceed 15 % of the welded sheet thickness. In the first case, the welding mode is called extremely rigid, in the second case it is the extremely soft. Naturally, the soft modes require lower source power, than the rigid ones.

Processing of welding modes for low-carbon steel 0.9–1.0 mm thick shows that the variation range of admissible current from the average one is equal to ± 32 % for extremely modes. Thus, the data from Table 1 can be corrected for soft modes (columns 8 and 9). These data correspond to simply the recommended soft modes, and in no way to the extremely soft ones.

In reality 1–2 mm electrodes are used for microwelding [3], Table 2.

On the other hand, the following dependence is valid for the extremely soft modes:

$$j_w^{\min} = \frac{0.089\sqrt{p}}{\delta^{0.5}}, \quad (3)$$

where j_w^{\min} is the minimum current density; p is the specific pressure of the electrodes.

Table 2. Recommended soft modes of spot resistance microwelding of low-carbon steels

δ , mm	d_{ef} , mm	j_w^{max} , kA/mm ²	I_w^{min} , A
0.05	1.0	1.056	0.875
0.10	1.0	0.743	0.583
0.15	1.0	0.607	0.477
0.20	1.5	0.526	0.929
0.25	1.5 (2.0)	0.470	0.830 (1.476)

Table 2 gives I_w^{min} values, calculated by (3), which correspond to those of minimum welding current for electrodes used in practice and $p = 7 \text{ kg/mm}^2$. As a result, it turns out that the entire range of thicknesses of interest to us, can be welded at approximately 1 kA current.

CONCLUSIONS

The thermal time constant of the welded sheets, is proportional to the square of sheet thickness.

For low-carbon steel, the coefficient of proportionality of the thermal time constant to the square of welded sheet thickness is $\approx 0.06 \text{ s/mm}^2$.

In order for the temperature ripple in welding low-carbon steel of $0.1 + 0.1 \text{ mm}$ thickness, which is due to thermal inertia of the spot weld, to be the same as in welding steel of $1.0 + 1.0 \text{ mm}$ thickness at 50 Hz frequency, welding current frequency should be 5 kHz.

Low-carbon steel of 0.05–0.25 mm thickness can be welded in soft (as in welding of medium thicknesses) modes, using up to 1 kA welding currents.

REFERENCES

- Bannov, M.D. (2005) *Resistance welding technology and equipment*. Moscow, Akademiya [in Russian].
- Ataush, V.E., Leonov, V.P., Moskvina, E.G. (1996) *Microwelding in instrument engineering*. Riga, RTU [in Russian].
- Moravsky, V.E., Vorona, D.S. (1985) *Technology and equipment for spot and projection capacitor-discharge welding*. Kiev, Naukova Dumka [in Russian].
- Kolupaev, Yu.F., Privezentsev, V.I. (2003) Peculiarities of capacitor-discharge welding of nichrome in producing of jewelry. *Svarochn. Proizvodstvo*, **11**, 41–43 [in Russian].
- Paerand, Yu.E., Bondarenko, A.F. (2005) Peculiarities of formation of current pulses for small-size parts. *Tekhnichna Elektrodynamika. Tem. Issue: Power Electronics and Power Efficiency*, Pt 3, 28–31 [in Russian].
- Paerand, Yu.E., Bondarenko, A.F. (2006) Application of special shape pulses for resistance microwelding. In: *Proc. of 7th Int. Sci.-Pract. Conf. on Modern Information and Electronic Technologies (MIET-2006)*, Odessa, Vol. 2, SE Neptun, Tekhnologiya.
- Paerand, Yu.E., Bondarenko, A.F. (2006) Power supply for resistance microwelding with programmable shape of welding pulse. *Tekhnologiya i Konstruirovaniye v Elektronnoy Apparature*, **4**, 51–54 [in Russian].
- Lankin, Yu.N. (1967) Electromodeling of thermal processes in resistance spot welding. *Avtomatch. Svarka*, **7**, 23–26 [in Russian].
- Lebedev, V.K., Yavorskiy, Yu.D. (1960) Application of similarity criteria for determination of resistance welding modes. *Ibid.*, **8**, 37–44 [in Russian].
- Paton, B.E., Lebedev, V.K. (1969) *Electric equipment for resistance welding. Theory elements*. Moscow, Mashinostroenie [in Russian].
- Paton, B.E., Gavrish, V.S., Grodetsky, Yu.S. (1963) Inertialess diagrams of automatic regulation of resistance welding processes. *Avtomatch. Svarka*, **5**, 7–10 [in Russian].
- Leonov, V.P., Barabanshchikova, L.A., Grechenkova, A.A., Ataush, V.E. (1990) Controllable power supply SARM-1 for resistance microwelding. *Svarochn. Proizvodstvo*, **10**, 36–38 [in Russian].

ORCID

Yu.M. Lankin: 0000-0001-6306-8086

CORRESPONDING AUTHOR

Yu.M. Lankin: 0000-0001-6306-8086

E.O. Paton Electric Welding Institute of the NASU
11 Kazymyr Malevych Str., 03150, Kyiv, Ukraine
E-mail: lankin.y.n@gmail.com

SUGGESTED CITATION

Yu.M. Lankin (2021) Requirements to technical characteristics of resistance microwelding machines. *The Paton Welding J.*, **11**, 34–37. <https://doi.org/10.37434/tpwj2021.11.06>

JOURNAL HOME PAGE

<https://pwj.com.ua/en>

Received 01.09.2021
Accepted: 29.11.2021

<https://doi.org/10.37434/tpwj2021.11.07>

COMPOSITE POWDERS BASED ON FeMoNiCrB AMORPHIZING ALLOY WITH ADDITIVES OF REFRACTORY COMPOUNDS FOR THERMAL SPRAYING OF COATINGS

Yu.S. Borysov¹, A.L. Borysova¹, O.M. Burlachenko¹, T.V. Tsymbalista¹, M.A. Vasykivska², E.G. Byba³

¹E.O. Paton Electric Welding Institute of the NAS of Ukraine
11 Kazymyr Malevych Str., 03150, Kyiv, Ukraine. E-mail: office@paton.kiev.ua

²I.M. Frantsevich Institute for Problems of Materials Science of the NASU
3 Krzhizhanovskiy Str., 03142, Kyiv

³E.O. Paton Institute of Materials Science and Welding of "Igor Sikorsky Kyiv Polytechnic Institute"
37 Peremohy Ave., 03056, Kyiv, Ukraine

ABSTRACT

The process of producing by mechanical alloying method composite powders based on FeMoNiCrB amorphizing alloy with additives of refractory compounds (ZrB₂, (Ti,Cr)C and FeTiO₃) by processing a mixture of powder components in planetary mill "Activator 2SL" was studied. It was found that after 1.5 h of processing its products are homogeneous conglomerates with average particle size, depending on the composition of composite powders, which was 23 μm in the case of FeMoNiCrB + ZrB₂, 15 μm in the case of FeMoNiCrB+(Ti, Cr)C, and 25 μm in the case of FeMoNiCrB + FeTiO₃. XRD analysis results reveal formation of an amorphous-nanocrystalline structure in the produced composite powders, which consists of Fe(Ni, Cr), Mo₅FeB₂ solid solution and disperse phase of additives of refractory compounds (ZrB₂, (Ti, Cr)C and FeTiO₃) with indications of certain interphase interaction of FeMoNiCrB and (Ti, Cr)C. Here, the amorphous phase appears as a result of the process of mechanical alloying. The values of measured microhardness in the composite powders were as follows: FeMoNiCrB + ZrB₂ – 6.2±1.6 MPa, FeMoNiCrB + (Ti, Cr)C – 5.5±1.1 MPa, FeMoNiCrB–FeTiO₃ – 5.1±0.7 MPa. For application in thermal spraying of coatings with an amorphous structure, the produced composite powders from mechanical alloying products are used to form conglomerate powders with particle size and degree of flowability, meeting the requirements of thermal spray coating technology.

KEY WORDS: amorphizing alloy, refractory compounds, composite powder, mechanical alloying, structure, phase composition, granulometric composition

INTRODUCTION

Progress in creating thermal spray coatings (TSC) with improved functional characteristics is largely determined by development of new types of materials for their deposition, including composite powders (CP).

Promising materials for TSC include alloys with an amorphous structure, which are characterized by a combination of such complexes of properties, as high strength, wear resistance, corrosion resistance, high yield limit, high magnetic permeability and small coercive force, high electric resistance and superconductivity [1, 2].

Formation of material amorphous structure takes place as a result of suppression of the processes of nucleation and crystallization, which is achieved at ultrafast quenching or introducing defects into the metal crystalline structure [2]. Particle cooling at formation of the coating layer under the conditions of thermal spraying at the rate of ~ 10⁶ K/s, enables producing

coatings with a metastable amorphous structure on the part surface [3].

Among amorphous thermal spray coatings, which are promising for commercial application on parts, exposed to wear in operation, we should single out iron-based alloys, which are characterized by high values of mechanical strength and corrosion resistance, and low cost [4]. However, their low values of wear resistance at dry friction and poor impact resistance limit the range of possible applications of such coatings [5].

Improvement of mechanical properties of iron-based amorphous coatings can be achieved by adding dispersed particles to the amorphous matrix. So, application of WC/12Co as inclusions allowed improving the adhesion strength and increasing the friction/wear resistance four times, compared to iron-based coating, having a purely amorphous structure [5]. Increase of amorphous coating wear resistance is also observed at application of dispersed TiN and B₄C inclusions [6, 7].

An important factor, influencing the properties of TS coatings is the uniformity of their structure. In

Table 1. Characteristics of initial powders

Material	Chemical composition, wt. %	Production method	T_m , K	γ , g/cm ³	HV, GPa
FeMoNiCrB	Fe – 36.2; Mo – 29.9; Ni – 23.6; Cr – 7.6; B – 2.7	Melt atomization by nitrogen	1523	7.84	6.2±1.2
ZrB ₂	Zr – 79.5; B – 19.0	Carbon-thermal method of zirconia reduction TU 6-09-03-46-75	3323	6.1	15.0±2.5
(Ti, Cr)C (ICTYX)	Ti – 54; Cr – 25.5; C _{total} – 18.6; C _w – 0.7	Self-propagating high-temperature synthesis TU No.88 Ukr.SSR 147.040-87	~3023	5.35	14.1±2.5
FeTiO ₃	Fe – 36.8; O – 31.6; Ti – 31.6	Crushing and grinding of ilmenite ore	1638	4.72	6.1±0.98

work [8] it is shown that TS coatings produced from a mechanical powder mixture, do not have a homogeneous composition by the coating thickness that affects the strength of the bond between the strengthening phase with the matrix material. At the same time, CP coatings have a layered fine lamellar structure and feature higher degree of density and homogeneity [9].

The main methods of producing CP include cladding and conglomeration, as well as a combination of these methods [10]. Among the modern methods of producing CP those of mechanical alloying (MA) and mechanochemical synthesis (MCS) should be noted.

The process of CP manufacture by MA or MCS methods consists in processing powder components in the high-power ball mills with a high content of grinding balls. During mechanical processing, the balls collide with each other, resulting in energy evolution. Ball collision is of a pulsed nature occurring for a short period of time of 10^{-12} – 10^{-13} s, and at penetration of powder particles into the contact region the energy is partially consumed by their deformation and refinement, and partially leads to increase of their internal energy. Internal energy relaxation occurs in different ways: heat evolution; multiplication and migration of crystalline structure defects; formation of internal interfaces; excitation of chemical reactions. Appearance of juvenile surfaces, as well as linear and point defects coming to the surface promote “cold” welding of the particles to each other with formation of composite particles of a layered structure. With longer processing time, the particles acquire a homogeneous structure, and a balance is achieved between the processes of their refinement and “cold” welding, leading to stabilization of the average particle size [11, 12]. It should be also noted that when conducting the MA process formation of an amorphous structure in the powder particles promotes generation of crystalline structure defects in them during MA.

The objective of the work was producing composite powders for thermal spraying of coatings with an amorphous-crystalline structure by mechanical alloying of a mixture, consisting of an amorphizing

FeMoNiCrB alloy and additive of one of the refractory compounds (ZrB₂, (Ti,Cr)C and FeTiO₃).

INVESTIGATION MATERIALS AND PROCEDURES

PG-N4 analog (FeCrMoB) was selected as the amorphizing alloy, which contains approximately 24 wt.% nickel in its composition. The most widely applied representatives of ceramic refractory compounds: zirconium boride ZrB₂, double titanium-chromium carbide (Ti, Cr)C (solid solution of 24 vol.% Cr₃C₂ in TiC) and FeTiO₃ (ilmenite) were selected as CP alloying phases. Table 1 gives the initial material characteristics.

Particle distribution by sizes, both for initial powders and for MA products, was determined both using Mastersizer 2000 analyzer of Malvern Panalytical Company, Great Britain, and by sieving analysis in compliance with DSTU 2640-94.

CP was produced in planetary mill “Activator 2SL” at the speed of rotation of the central axle of 1000 rpm, and of the drums — of 1500 rpm. The drum body and the balls were made from ShKh15 steel. In order to prevent welding of the mixture to the walls of the drums and crushing bodies during material processing, a surfactant (SA) was added to the mixture: oleic acid (CH₃(CH₂)₇CH = CH(CH₂)₇COOH) in the quantity of 0.5 wt.%. The process was conducted in air with taking of intermediate samples every 0.5 h of processing.

Microdurometric analysis of the initial particles and obtained products was conducted in microhardness meter PMT-3 at 25 g load on the indenter with subsequent plotting of variation curves of microhardness values by the results of 30 measurements [13].

Chemical analysis of the produced CP was performed in electron microscope JSM-6390LV (JEOL, Japan) with energy-dispersive (EDS) attachment INCA ENERGY (Oxford Instrument, Great Britain), in secondary electron mode in low (10^{-4} Pa) vacuum, with 20 kV accelerating voltage.

X-ray structural phase (XRD) analysis of the produced CP was conducted in “DRON-UM-1” unit, in CuK_α radiation, monochromatized.

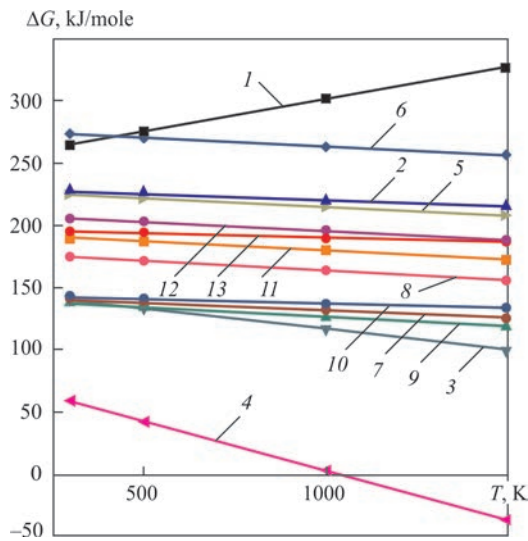


Figure 1. Temperature dependence of the change of Gibb's energy of $Me + ZrB_2$ reaction, where Me is Fe, Mo, Ni, Cr, B: 1 — $2Fe + ZrB_2 = 2FeB + Zr$; 2 — $Mo + ZrB_2 = MoB_2 + Zr$; 3 — $2Mo + ZrB_2 = 2MoB + Zr$; 4 — $4Mo + ZrB_2 = 2Mo_2B + Zr$; 5 — $Ni + ZrB_2 = NiZr + 2B$; 6 — $1/2Ni + ZrB_2 = 1/2NiZr_2 + 2B$; 7 — $7/2Ni + ZrB_2 = 1/2Ni_7Zr_2 + 2B$; 8 — $5Ni + ZrB_2 = Ni_5Zr + 2B$; 9 — $3Ni + ZrB_2 = 1Ni_3Zr + 2B$; 10 — $23/8Ni + ZrB_2 = 1/8Ni_{23}Zr_8 + 2B$; 11 — $10/7Ni + ZrB_2 = 1/7Ni_{10}Zr_7 + 2B$; 12 — $11/9Ni + ZrB_2 = 1/9Ni_{11}Zr_9 + 2B$; 13 — $Cr + ZrB_2 = CrB_2 + Zr$

THERMODYNAMIC EVALUATION OF THE REACTIONS AT AMORPHIZING ALLOY INTERACTION WITH REFRACTORY COMPOUNDS AND SELECTION OF COMPOSITE POWDER COMPOSITION

Thermodynamic calculations were performed to determine the probability of running of the reactions be-

tween metal matrix elements (Fe, Mo, Ni, Cr and B) and refractory compound inclusions (ZrB_2 (Ti, Cr)C and $FeTiO_3$) at heating up to 1500 K. In connection with absence of published data on heat of formation and entropy of double titanium-chromium carbide (Ti, Cr)C, thermodynamic data for Cr_3C_2 and TiC carbides were used for calculations. The results of thermodynamic calculations are given in Figures 1–3.

Analysis of the obtained data leads to the following conclusions.

1. Fe, Cr and Ni interaction with ZrB_2 is thermodynamically impossible below 1500 °C, Mo_2B only forms as a result of ZrB_2 interaction with Mo at more than 1000 °C temperature.

2. Thermodynamic calculations for TiC and Cr_3C_2 show that interaction with boron results in formation of titanium and chromium borides (TiB_2 and CrB_2), respectively. More over, in $Mo + Cr_3C_2$ system a reaction can proceed with formation of molybdenum carbide Mo_2C , and in $Ni + Cr_3C_2$ — a reaction with formation of nickel carbide (Ni_3C).

3. Thermodynamic calculations for $Me + FeTiO_3$ system show that oxides, namely TiO_2 , Cr_2O_3 and B_2O_3 can form in this system.

RESULTS OF EXPERIMENTAL STUDIES

At selection of the composition of powder mixture to produce composite particles in this study, the authors were guided by recommendations on production of wear-resistant composite materials by powder metal-

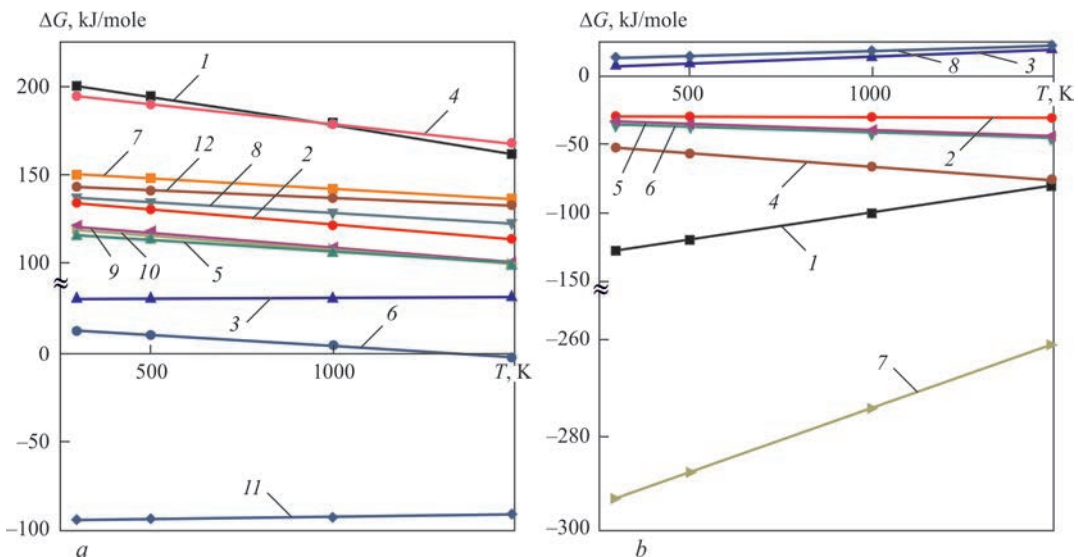


Figure 2. Temperature dependence of the change of Gibb's energy of the following reactions: a — $Me + TiC$; b — $Me + Cr_3C_2$, where Me — Fe, Mo, Ni, Cr, B; for a: — 1 — $3Fe + TiC = Fe_3C + Ti$; 2 — $2Mo + TiC = Mo_2C + Ti$; 3 — $3/2Mo + TiC = 1/2Mo_3C_2 + Ti$; 4 — $3Ni + TiC = Ni_3C + Ti$; 5 — $Ni + TiC = NiTi + C$; 6 — $3Ni + TiC = Ni_3Ti + C$; 7 — $1/2Ni + TiC = 1/2NiTi_2 + C$; 8 — $3/2Cr + TiC = 1/2Cr_3C_2 + Ti$; 9 — $7/3Cr + TiC = 1/3Cr_7C_3 + Ti$; 10 — $23/6Cr + TiC = 1/6Cr_{23}C_6 + Ti$; 11 — $2B + TiC = TiB_2 + C$; 12 — $4B + TiC = B_4C + Ti$; for b: — 1 — $6Fe + Cr_3C_2 = 2Fe_3C + 3Cr$; 2 — $3Mo + Cr_3C_2 = Mo_3C_2 + 3Cr$; 3 — $4Mo + Cr_3C_2 = 2Mo_2C + 3Cr$; 4 — $6Ni + Cr_3C_2 = 2Ni_3C + 3Cr$; 5 — $14/3Cr + Cr_3C_2 = 1/3Cr_{14}C_6$; 6 — $5/3Cr + Cr_3C_2 = 2/3Cr_5C_3$; 7 — $6B + Cr_3C_2 = 3CrB_2 + 2C$; 8 — $8B + Cr_3C_2 = 2B_4C + 3Cr$

lurgy methods, according to which the dispersed inclusion content is equal to 20–30 vol.% [14].

Figure 4 shows the appearance and microstructure of initial powder particles, and Figure 5 gives their distribution by size. As once can see, the particles of FeMoNiCrB powder are of a spherical shape, which is characteristic for powders produced by the method of melt atomization with nitrogen. Powders of ceramic compounds are of an angular shape, characteristic for hard and brittle materials. Average size of FeMoNiCrB alloy particles is equal to $\sim 110 \mu\text{m}$, that of ZrB_2 and (Ti, Cr)C refractory compounds is 65 and $55 \mu\text{m}$, respectively. Size of 96 % of FeTiO_3 particles is to the range of 40–100 μm .

XRD analysis of initial powders revealed that FeMoNiCrB alloy powder has a multiphase crystalline structure with a low degree of amorphization in the region of iron-based solid solution (Figure 6, *a*). ZrB_2 powder has no admixtures (Figure 6, *b*), a small quantity of TiO was found in (Ti, Cr)C powder (Figure 6, *c*), and Fe_2O_3 can be present in FeTiO_3 (Figure 6, *d*).

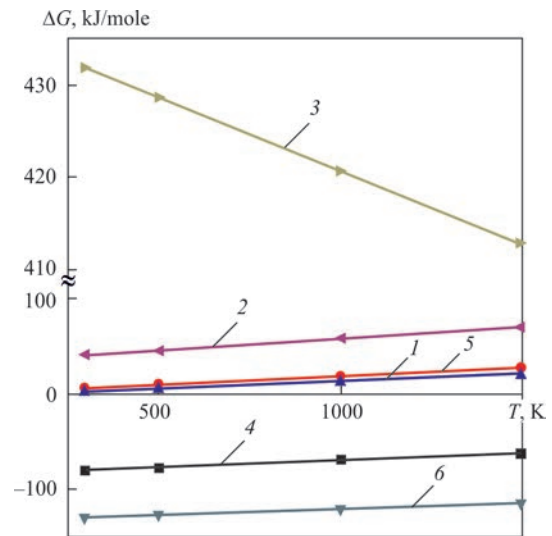


Figure 3. Temperature dependence of the change of Gibbs's energy for $\text{Me} + \text{FeTiO}_3$ reaction, where $\text{Me} = \text{Fe}, \text{Mo}, \text{Ni}, \text{Cr}, \text{B}$: 1 — $1/2\text{Mo} + \text{FeTiO}_3 = \text{Fe} + 1/2\text{MoO}_2 + \text{TiO}_2$; 2 — $\text{Ni} + \text{FeTiO}_3 = \text{NiTiO}_3 + \text{Fe}$; 3 — $3/4\text{Ni} + \text{FeTiO}_3 = 3/4\text{NiFe}_2\text{O}_4 + 1/2\text{Fe} + \text{Ti}$; 4 — $2/3\text{Cr} + \text{FeTiO}_3 = \text{Fe} + 1/3\text{Cr}_2\text{O}_3 + \text{TiO}_2$; 5 — $1/2\text{Cr} + \text{FeTiO}_3 = \text{Fe} + 1/2\text{CrO}_2 + \text{TiO}_2$; 6 — $2/3\text{B} + \text{FeTiO}_3 = \text{Fe} + 1/3\text{B}_2\text{O}_3 + \text{TiO}_2$

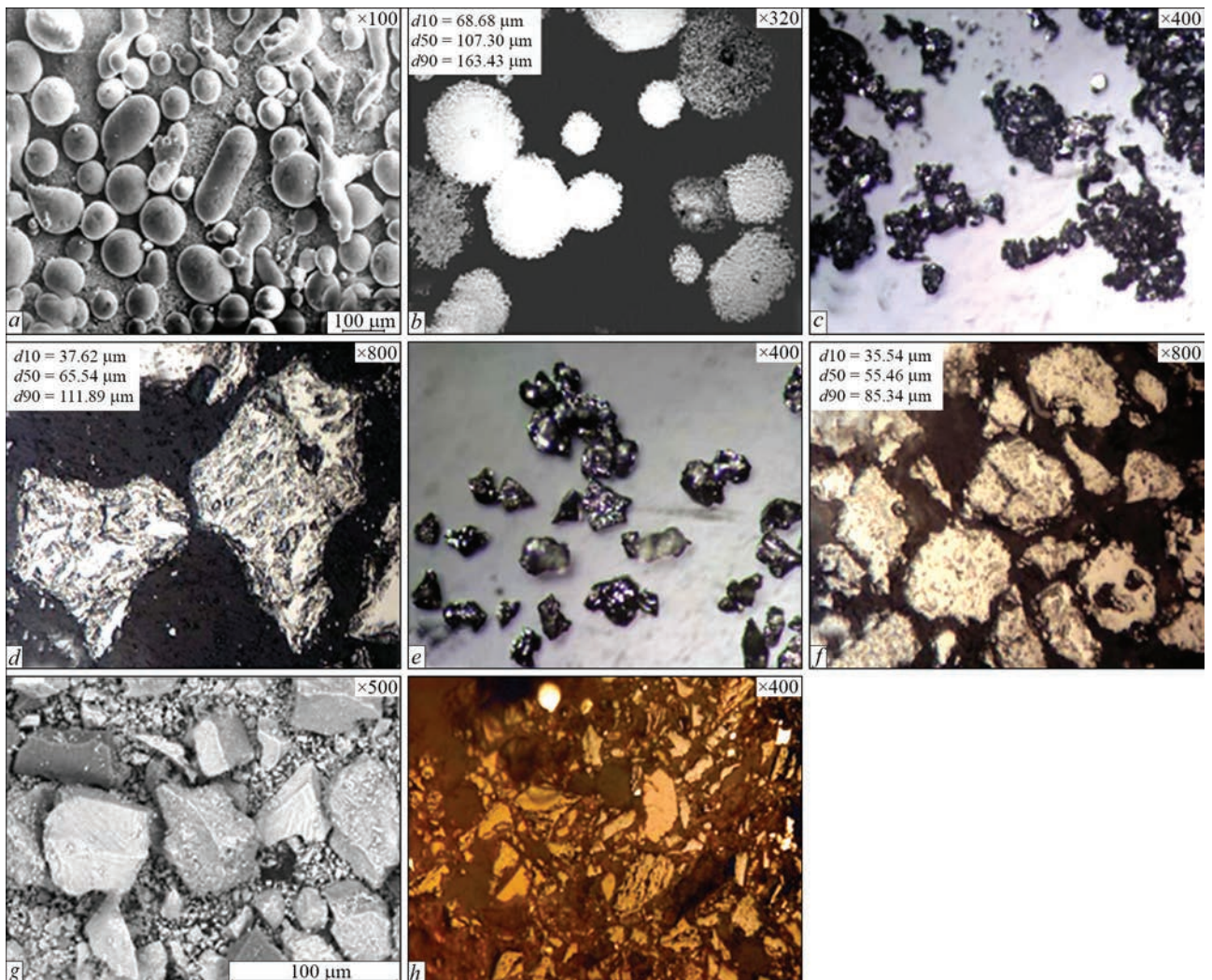


Figure 4. Appearance (*a, c, e, g*) and microstructure (*b, d, f, h*) of the following powders: *a, b* — FeMoNiCrB; *c, d* — ZrB_2 ; *e, f* — (Ti, Cr)C; *g, h* — FeTiO_3

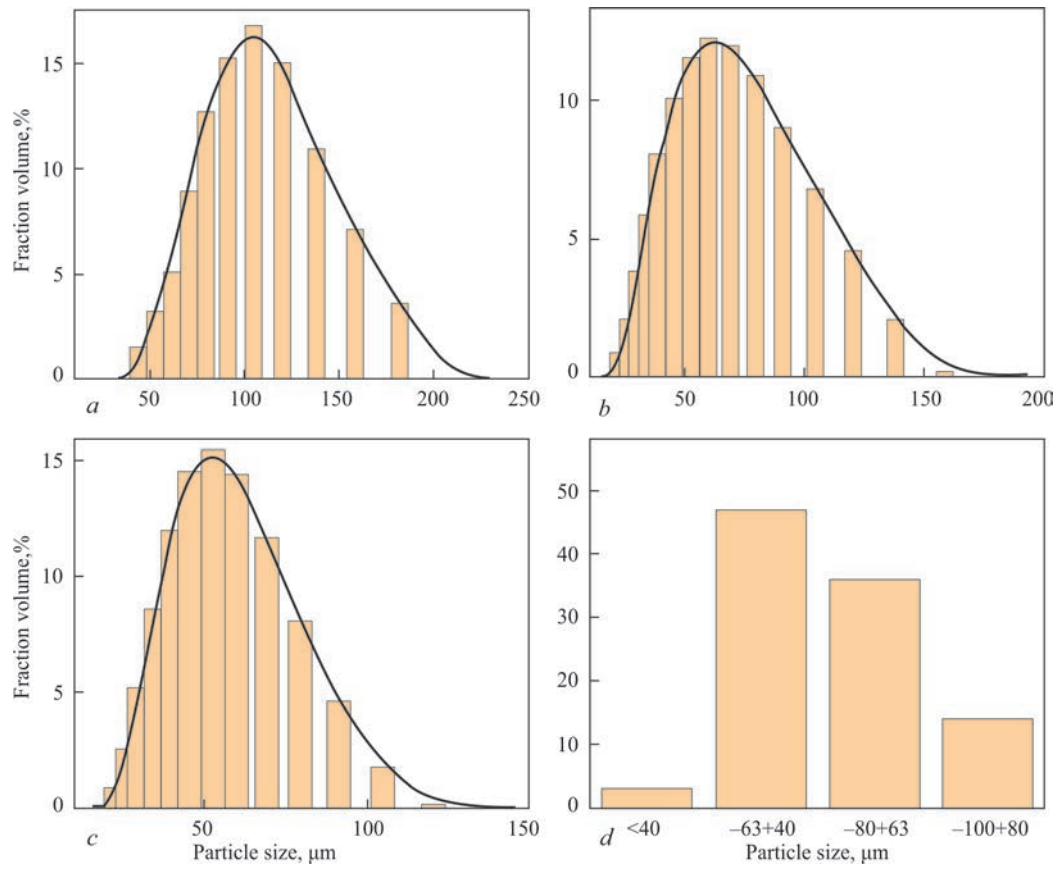


Figure 5. Distribution of initial powder particles by size: *a* — FeMoNiCrB; *b* — ZrB₂; *c* — (Ti, Cr)C; *d* — FeTiO₃ (*a*, *b*, *c* — Master-sizer 2000 analyzer; *d* — sieve analysis)

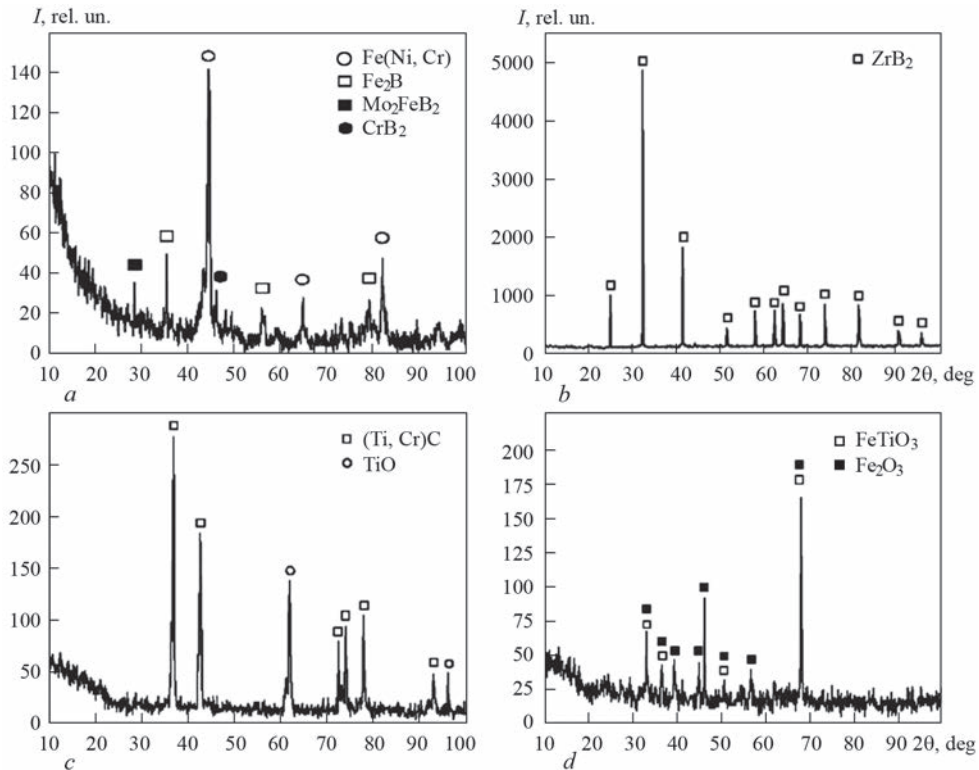


Figure 6. X-ray patterns of initial powders: *a* — FeMoNiCrB; *b* — ZrB₂; *c* — (Ti, Cr)C; *d* — FeTiO₃

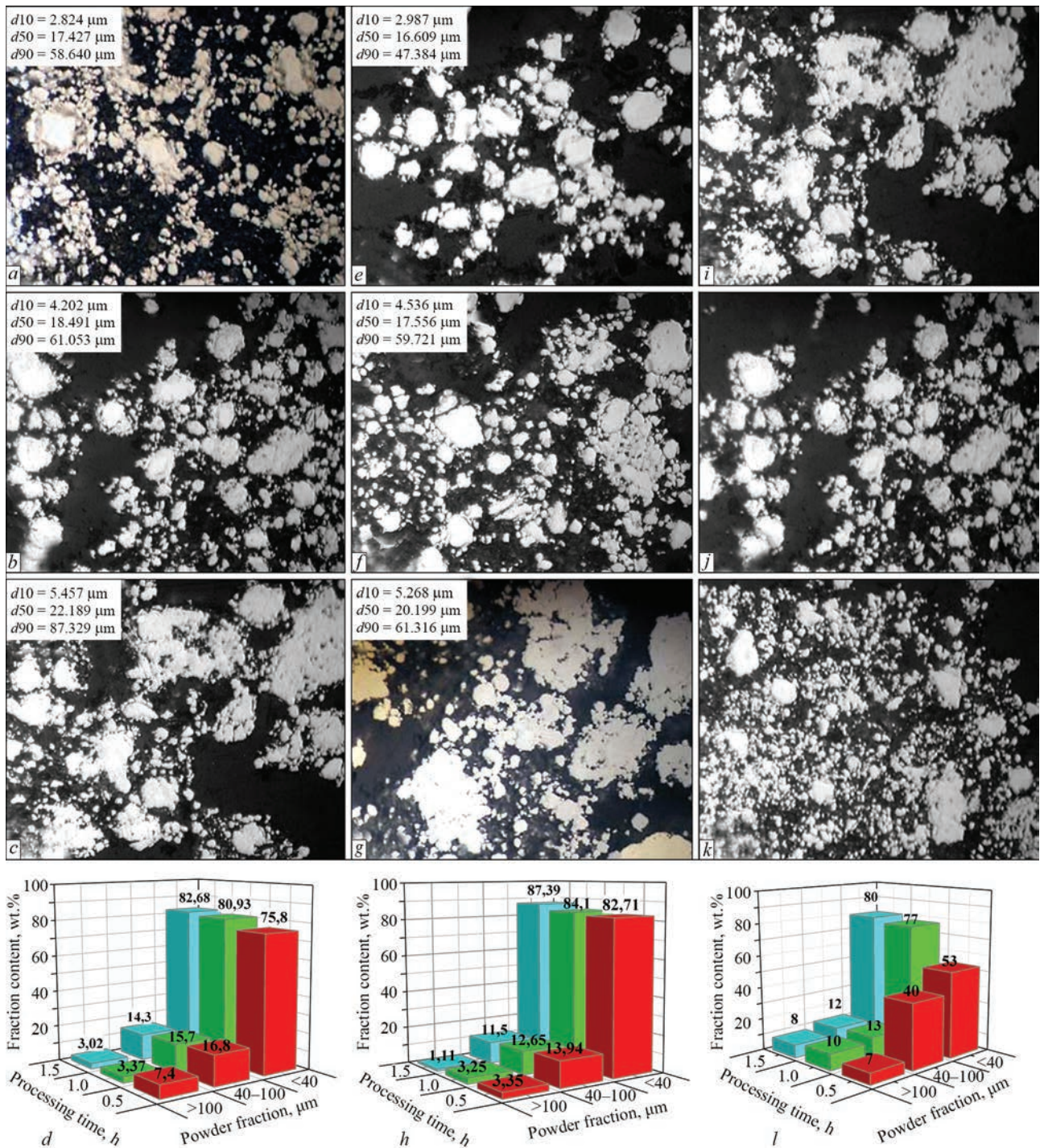


Figure 7. Microstructure ($\times 800$) (a, b, c, e, f, g, h, i, j, k) and histograms of powder particle size distributions (d, h, l) at different MA process duration for the following mixtures: a, b, c, d — FeMoNiCrB + ZrB₂; e, f, g, h — FeMoNiCrB + (Ti, Cr)C; i, j, k, l — FeMoNiCrB + FeTiO₃

Investigation of the structure and size of powder particles during CP formation showed (Figure 7) that at the initial processing stages the refinement processes prevail over those of cold welding. As a result of it, after 0.5 h of processing the size of the main mass of the particles decreases, compared to the initial one to $< 40 \mu\text{m}$, and the average particle size is equal to 16–17 μm . Further processing of the powder mixtures leads to increase of the mass of particles of $< 40 \mu\text{m}$ size (Figure 7, d, h, l). Here, the average particle size

increases up to 20–22 μm (Figure 7, c, g), which is indicative of cold welding of initial powder particles to each other with formation of agglomerates.

Investigation of size distribution of composite powder particles with inclusions of refractory compounds, depending on their processing time (Figure 8), showed that at the initial stages as a result of particle refinement the powder mixtures become bimodal with two most probable modes of 4–5 and 23–26 μm (Figure 8, a). Such a spreading can be re-

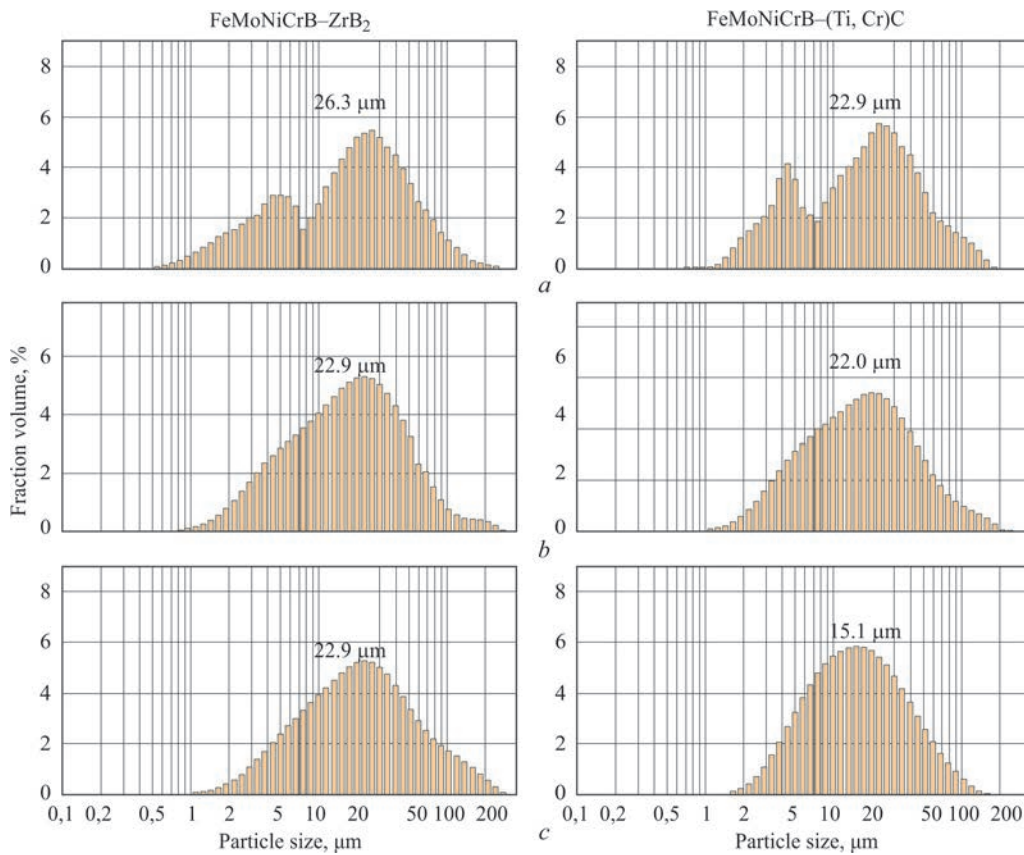


Figure 8. Particle size distribution, depending on mixture processing time: *a* — 0.5; *b* — 1.0; *c* — 1.5 h

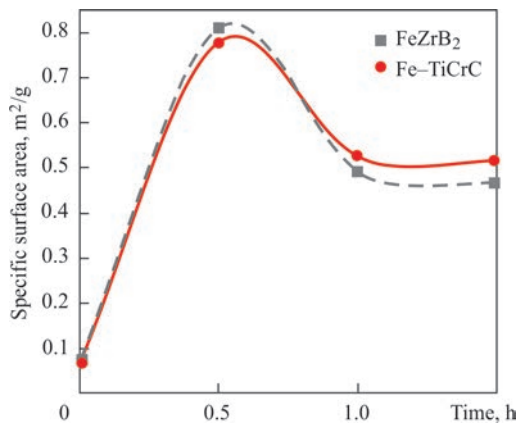


Figure 9. Change of specific surface area of CP particles, depending on their processing time

lated to a more intensive refinement of particles with a higher brittleness value. With the start of agglomerate formation (after 1.0 h of processing) particle size distribution becomes monomodal.

One of the characteristics of powder materials is the specific surface of the particles. Evaluation of the change of the particle specific surface at different stages of powder processing (Figure 9) showed that at the initial stages of processing, when the refinement processes prevail, an increase of the particle specific surface occurs with reaching of the maximum value after 0.5 h. With the start of agglomerate formation, a reduction of the particle specific surface is observed, which goes on until an equilibrium has been reached between the processes of refinement and cold welding of the particles to each other, which is indicated by a

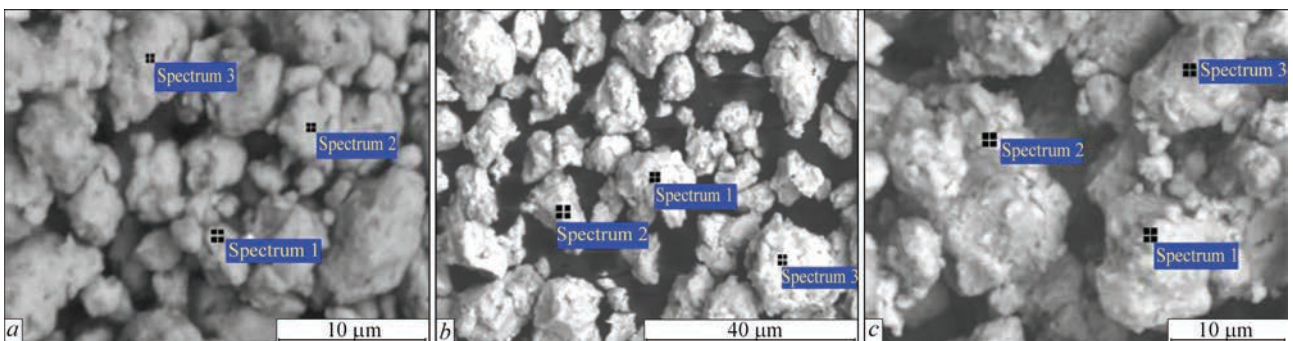


Figure 10. Appearance of particles after processing the following powder mixtures in a planetary mill for 1.5 h: *a* — FeMoNiCrB + ZrB₂; *b* — FeMoNiCrB + (Ti, Cr)C; *c* — FeMoNiCrB + FeTiO₃

Table 2. Averaged values of particle chemical composition after processing the powder mixture for 1.5 h

FeMoNiCrB–ZrB ₂					
Fe	Mo	Ni	Cr	Zr	O
24.18±0.13	22.82±0.26	22.95±0.11	5.55±0.19	17.47±0.19	7.03±0.09
FeMoNiCrB–(Ti,Cr)C					
Fe	Mo	Ni	Cr	Ti	O
23.02±0.10	23.23±0.31	23.79±0.12	11.52±0.93	10.66±0.2	7.78±0.13
FeMoNiCrB–FeTiO ₃					
Fe	Mo	Ni	Cr	Ti	O
30.98±0.52	23.85±0.24	21.23±0.16	7.05±0.51	4.18±0.37	12.71±0.78

practical absence of changes of the specific surface of the processing products.

After processing of the powder mixtures in the planetary mill for 1.5 h, the particles of all the com-

positions take a rounded shape (Figure 10). Here, as shown by EDS analysis, each of them contains all the elements of the initial components: metal (Fe, Mo, Ni, Cr) and refractory compounds (Ti, Zr), i.e. it is a CP

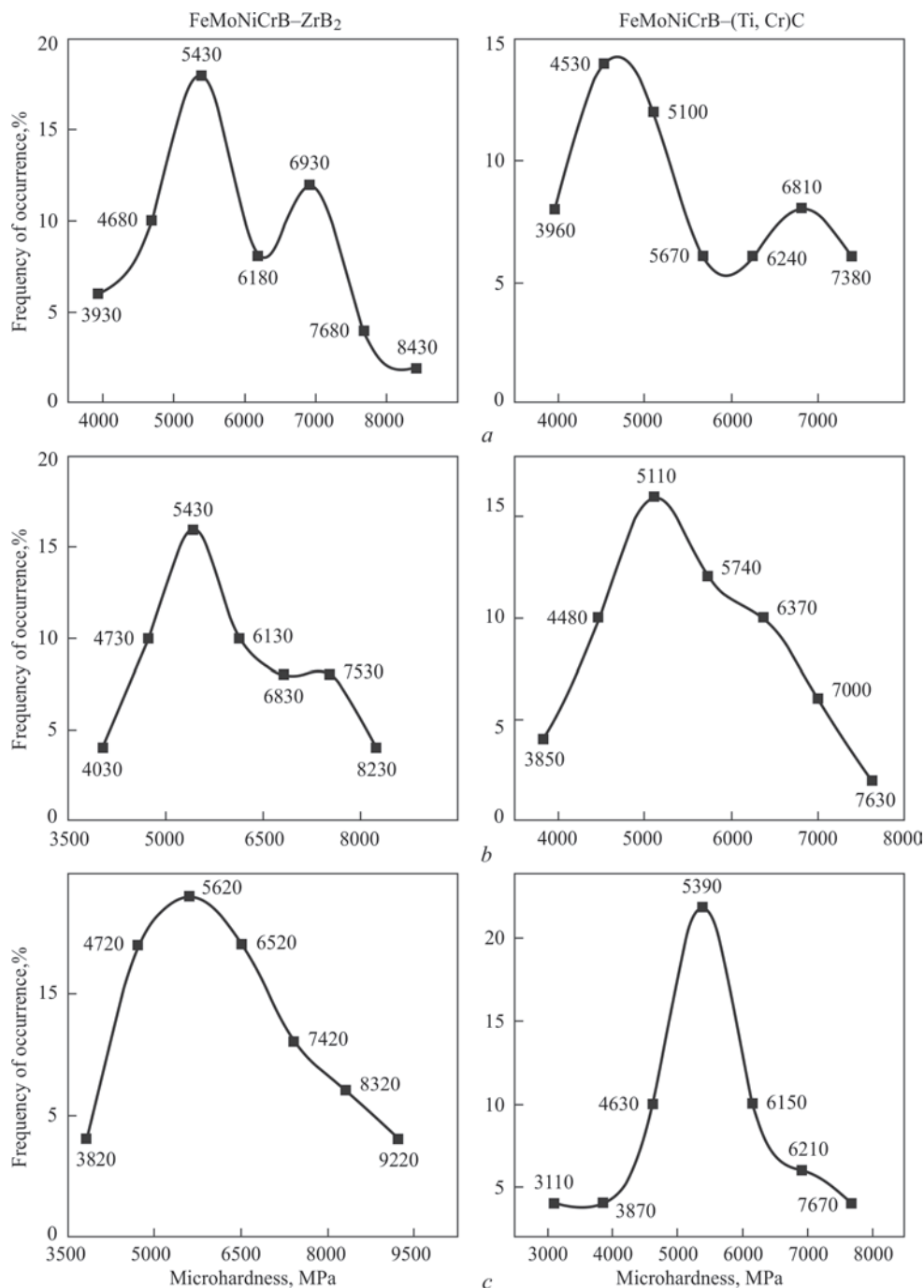


Figure 11. Variation curves of particle microhardness after mixture processing for a — 0.5; b — 1.0; c — 1.5 h

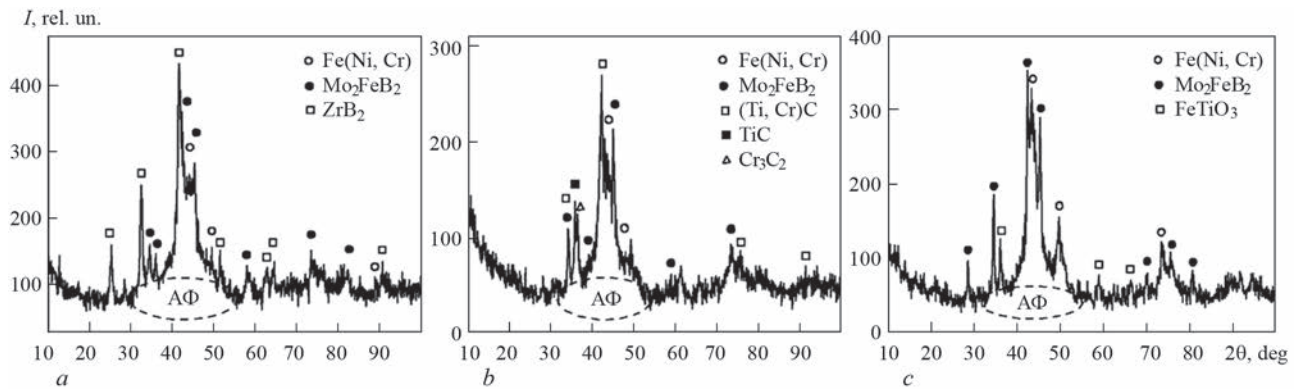


Figure 12. X-ray patterns of the following powders: *a* — FeMoNiCrB–ZrB₂; *b* — FeMoNiCrB–(Ti, Cr)C; *c* — FeMoNiCrB–FeTiO₃

Table 3. Characteristics of MA products, produced after 1.5 h

Composition	Phase composition	Particle size, μm	HV, GPa
FeMoNiCrB–ZrB ₂	Sol. sol Fe(Ni, Cr), Mo ₂ FeB ₂ , ZrB ₂ , amorphous phase	5–87	6.2±1.6
FeMoNiCrB–(Ti, Cr)C	Sol. sol Fe(Ni, Cr), Mo ₂ FeB ₂ , (Ti, Cr)C, TiC, Cr ₃ C ₂ , amorphous phase	5–61	5.5±1.1
FeMoNiCrB–FeTiO ₃	Sol. sol Fe(Ni,Cr), Mo ₂ FeB ₂ , FeTiO ₃ , amorphous phase	<40	5.1±0.7

particle (Table 2). Presence of oxygen in the mixtures with ZrB₂ and (Ti, Cr)C is indicative of oxidation during MA, as the process was conducted in air.

Thus, powder mixture processing for 1.5 h is quite sufficient to produce composite particles with a uniform distribution of the components. Further increase of processing time is pointless, the more so as it will lead only to additional oxidation of the powder and its contamination by the products of destruction of the walls of the drums and grinding bodies.

By the shape of variation curves of powder particle microhardness at different stages of mechanical alloying (Figure 11), the presence of two peaks of microhardness values on the graphs after 30 min of processing can be noted (Figure 11, *a*).

Increase of process duration up to 1.0 h, resulting in formation of agglomerates, consisting from initial ceramic and metal particles, leads to the presence of just one most probable microhardness value being noted on the variation curves (Figure 11, *b, c*). After 1.5 h of processing, the average microhardness is equal to $HV = 6.2 \pm 1.6$ GPa for FeMoNiCrB–ZrB₂, $HV = 5.5 \pm 1.1$ GPa for FeMoNiCrB–(Ti,Cr)C and 5.1 ± 0.7 GPa for FeMoNiCrB–FeTiO₃ compositions.

Method of XRD analysis of composite powder particles obtained after 1.5 h of MA (Figure 12) revealed that all of them had an amorphous-crystalline structure. Broadening of X-ray image lines is indicative of particle refinement to the nanoscale. Evaluation of the coherent scatter regions showed that the size of CSR for ZrB₂ decreased from 128 to 23 nm, for (TiCr)C – from 56 to 17 nm, and for FeMoNiCrB

alloy — from 48 to 12 nm. As regards amorphization of FeMoNiCrB alloy during MA, this is indicated by formation of a “halo” in X-ray patterns in angle ranges of $2\theta = 39.9\text{--}52.8^\circ$ and $68.2\text{--}84.3^\circ$.

No formation of new phases during MA as a result of interaction between FeMoNiCrB alloy elements and refractory compounds was revealed. We can only note merging of the main peaks of X-ray images for Ni, Cr, and Fe solid solutions into one, which may be indicative of formation of an oversaturated iron-based solid solution. More over, a splitting of the diffraction peak is observed at $2\theta = 36.8^\circ$ angle, which corresponds to double titanium-chromium carbide (Ti, Cr)C into two, which correspond to TiC and Cr₃C₂ phases, pointing to decomposition of double titanium-chromium carbide.

Results on phase composition and microhardness of MA products after 1.5 h of processing are shown in Table 3.

Produced during MA amorphous-nanocrystalline cermet powders, which consist of an amorphizing Fe-based matrix with refractory compounds introduced into its volume, can be used in the technology of thermal spraying of composite coatings with an amorphous structure. However, the small particle size (15–22 μm) and high value of specific surface (~0.5 m²/g), resulting in absence of fluidity in powders, complicates their uniform feeding into the flow at TS. In order to increase the particle size of MA products and their fluidity, conglomeration of MA products with 5 % solution of polyvinyl alcohol in water is performed with subsequent drying of the

mixture at the temperature of 80 °C, grinding of the obtained conglomerates and screening of particles of 40–63 µm size.

CONCLUSIONS

1. Studied were the physicochemical processes taking place at formation of composite powders based on FeMoNiCrB under the conditions of mechanical alloying with addition of ZrB₂, (Ti, Cr)C and FeTiO₃ alloying additives.

2. It is found that mechanical alloying results in formation of amorphous-nanocrystalline cermet powders, consisting of an oversaturated Fe(Ni, Cr) solid solution and additives of refractory compounds (ZrB₂, (Ti, Cr)C or FeTiO₃) and having the values of average microhardness of FeMoNiCrB-ZrB₂ cermets of 6.2±1.6 GPa, FeMoNiCrB-(Ti, Cr)C – 5.5±1.1 GPa and FeMoNiCrB-FeTiO₃ – 5.1±0.7 GPa.

3. It was established that stabilization of the size of conglomerate particles during MA of a mixture of FeMoNiCrB + ZrB₂, FeMoNiCrB – (Ti, Cr)C and FeMoNiCrB + FeTiO₃ powders occurs after processing for 1.5 h and the average particle size is as follows: FeMoNiCrB + ZrB₂ – 23 µm; for FeMoNiCrB – (Ti, Cr)C – 15 µm, for FeMoNiCrB – FeTiO₃ – 25 µm.

4. In order to use the obtained MA products for thermal spraying of the composite coatings with an amorphized structure, powders with a conglomerate structure and particle size of 40–63 µm were produced.

REFERENCES

- Suzuki, K., Fujimori, H., Hasimoto, K. (1987) *Amorphous metals*. Ed. by Ya.I. Polyak, B.I. Kekalo. Moscow, Metallurgiya [in Russian].
- Kunitsky, Yu.A., Korzhik, V.N., Borisov, Yu.S. (1988) *Non-crystalline metal materials and coatings in engineering*. Kiev, Tekhnika [in Russian].
- Kalita, V.I., Komlev, D.I. (2008) *Plasma coatings with nanocrystalline and amorphous structure*. Moscow, Lider M [in Russian].
- Yongjiang, H., Yuanzhi, G., Hongbo, F., Jun, S. (2012) Synthesis of Fe–Cr–Mo–C–B amorphous coating with high corrosion resistance. *Materials Letters*, **89**, 229–232. DOI: <https://doi.org/10.1016/j.matlet.2012.08.114>.
- Terajima, T., Takeuchi, F., Nakata, K. et al. (2010) Composite coating containing WC/12Co cermet and Fe-based metallic glass deposited by high-velocity oxygen fuel spraying. *J. of Alloys and Compounds*, **504(1)**, 288–291. DOI: <https://doi.org/10.1016/j.jallcom.2010.03.209>
- Yugeswaran, S., Kobayashi, A., Suresh, K., Subramanian, B. (2013) Characterization of gas tunnel type plasma sprayed TiN reinforced Fe-based metallic glass coatings. *Ibid.*, **551**, 168–175. DOI: <https://doi.org/10.1016/j.jallcom.2012.09.111>
- Movahedi, B. (2018) Mechanical investigation approach to optimize the high-velocity oxygen fuel Fe-based amorphous coatings reinforced by B₄C nanoparticles. *World Academy of Sci., Engineering and Technology Int. J. of Materials and Metallurgical Engineering*, **12(9)**, 460–465. DOI: <https://doi.org/10.5281/zenodo.1474539>
- Korzhik, V.N., Borisova, A.L., Popov, V.V. et al. (2014) Cermet coatings of chromium carbide-nichrome system produced by supersonic plasma gas air spraying. *The Paton Welding J.*, **12**, 23–28. DOI: <https://doi.org/10.15407/tpwj2014.12.05>.
- Borisov, Yu.S., Borisova, A.L., Astakhov, E.A. et al. (2017) Detonation coatings of intermetallic powders of Fe–Al system produced using mechanical alloying. *Ibid.*, **4**, 25–31. DOI: <https://doi.org/10.15407/as2017.04.05>
- Borisov, Yu.S., Borisova, A.L. (1986) *Plasma powder coatings*. Kiev, Tekhnika [in Russian].
- Vityaz, P.A., Lovshenko, F.G., Lovshenko, G.F. (1998) *Mechanically-doped alloys based on aluminium and copper*. Minsk, Belarusskaya Nauka [in Russian].
- Grigorieva, T.F., Barinova, A.P., Lyakhov, N.Z. (2008) *Mechanochemical synthesis in metallic systems*. Ed. by E.G. Avvakumov. Novosibirsk, Parallel [in Russian].
- Lebedeva, S.I. (1977) *Microhardness of minerals*. Ed. by S.A.Yushko. Moscow, Nedra [in Russian].
- Surzhenkov, A., Antonov, M., Goljandin, D. et al. (2013) Sliding wear of TiC–NiMo and Cr₃C₂–Ni cermet particles reinforced FeCrSiB matrix HVOF sprayed coatings. *Estonian J. of Engineering*, **19(3)**, 203–211. DOI: <https://doi.org/10.3176/eng.2013.3.03>.

ORCID

Yu.S. Borysov: 0000-0002-6019-8464,
A.L. Borysova: 0000-0002-7376-3370,
O.M. Burlachenko: 0000-0001-8576-2095,
T.V. Tsymbalista: 0000-0001-9569-7776,
M.A. Vasylykivska: 0000-0001-8311-6428,
E.G. Byba: 0000-0002-1696-300X

CONFLICT OF INTEREST

The Authors declare no conflict of interest

CORRESPONDING AUTHOR

Yu.S. Borysov
E.O. Paton Electric Welding Institute of the NASU
11 Kazymyr Malevych Str., 03150, Kyiv, Ukraine
E-mail: borysov@paton.kiev.ua

SUGGESTED CITATION

Yu.S. Borysov, A.L. Borysova, O.M. Burlachenko, T.V. Tsymbalista, M.A. Vasylykivska, E.G. Byba (2021) Composite powders based on FeMoNiCrB amorphizing alloy with additives of refractory compounds for thermal spraying of coatings. *The Paton Welding J.*, **11**, 38–47. <https://doi.org/10.37434/tpwj2021.11.07>

JOURNAL HOME PAGE

<https://pwj.com.ua/en>

Received 05.08.2021
Accepted: 29.11.2021

<https://doi.org/10.37434/tpwj2021.11.08>

MULTISCALE PROCEDURE OF NUMERICAL EVALUATION OF DAMAGE AND TECHNICAL STATE OF STRUCTURES FROM FIBER COMPOSITE MATERIALS

O.S. Milenin, O.A. Velykoivanenko, G.P. Rozyuka, N.I. Pivtorak

E.O. Paton Electric Welding Institute of the NASU
11 Kazymyr Malevych Str., 03150, Kyiv, Ukraine

ABSTRACT

A multiscale procedure of forecasting of stress-strain, damaged and boundary states of structures from typical fiber composite materials was developed. The procedure is based on the combination of macroscale models of describing the state of structurally inhomogeneous brittle materials and mesoscale approaches of continuing modeling of development of damage under the effect of external load. On the example of large-sized cylindrical pressure vessels from glass and carbon fiber composites, features of external load on the damage to the material and boundary state of the structure were investigated.

KEY WORDS: composite materials, damage, boundary state, mathematical modeling, multiscale procedure

INTRODUCTION

The use of composite materials during manufacture of structures for the needs of the aerospace industry, automotive production and building is an effective method for creating structural elements with unique combinations of operational properties. In particular, fiber composites based on glass and carbon fibers became widespread, which allow achieving a high strength of thin-walled structures at their relatively small weight [1–3]. However, spatial heterogeneity of the structure of such materials leads to objective difficulties in designing, expertise of a technical state and analysis of the serviceability of real structural elements, in particular, large-sized ones. The use of generally accepted approaches, consisting in evaluating the effective properties of a material for its further consideration as a homogeneous significantly limit the scope of solvable practically important problems. In particular, it is known that the process of initiation and propagation of material defects is microscopic as to its scale. Therefore, for the correct evaluation of the degree of damage and account of subcritical damages in the evaluation of the boundary state of the structure under the influence of the design load, it is necessary to take into account the features of the material structure and its resistance to a certain mechanism of fracture [4].

The possibilities of numerical description of composite structures in a heterogeneous statement are limited by the resource capacity of the relevant problems. Therefore, the development of analytical approaches that, on a one hand, allow taking into account the features of the microstructural state of the material in modeling, and on the other, considering specific structural elements without a significant simplification, are relevant. Here, it is advisable to separate the methods

of multiscale modeling based on modern algorithms for finite element modeling of complex multiscale processes [5, 6]. The aim of this work is to develop methodologies and numerical means of multiscale forecasting of stress-strained, damaged and boundary states of structures from typical fiber composite materials.

The main idea of the developed methodology is a progressive finite element realization of monitoring the state of the structure in general in a homogeneous anisotropic approximation (macroscale) and separately of each regular mesoscale region in a heterogeneous approximation (mesoscale). This allows avoiding excessive requirements to resources of computing means by increasing the speed of a separate calculation. In this case, the independence of calculations of certain mesoscale regions provides extensive opportunities for the use of algorithms for parallel calculation of the corresponding boundary problems with the aim of a significant shortening in the time for carrying out numerical experiments [7]. The connection between the levels is realized by transmitting a certain volume of calculated data, namely, a strained state and a subcritical damage (Figure 1).

For computer realization of the mentioned approach, the methods of finite element modeling based on eight-node elements were used, and each finite element of macroproblem was considered as a regular mesoregion, within which the corresponding meso-problem was stated.

Thus, macroscale approximation requires the use of averaged physicomaterial properties of the material, depending on the composition of a two-component composite (bulk content of the material of the matrix V_m and a fiber filler V_f) and the properties of its separate components. Here the most common are those

approaches based on the rule of mixtures. In particular, for the case in a macroscale, the composite material is considered as an elastic orthotropic one, and the value of the Young modulus along and across the fibers is calculated according to the rule of mixtures [8]:

$$\begin{cases} E_T = \frac{E_f E_m}{E_m V_f + E_f (1 - V_f)}; \\ E_L = E_f V_f + E_m (1 - V_f), \end{cases} \quad (1)$$

where E_m, E_f is the Young modulus of the material matrix and fibers, respectively; E_T, E_L is the Young modulus of conventionally homogeneous anisotropic composite along and across the fibers, respectively.

In order to determine the Poisson's ratio, the dependence of Whitney and Riley in the next formulation was used [9]:

$$\begin{cases} \nu_{LT} = \frac{\nu_m - [2(\nu_m - \nu_f)(1 - \nu_m^2)E_f V_f]}{E_m (1 - V_f)(1 - \nu_f - 2\nu_f^2) + E_f [V_f(1 - \nu_m - 2\nu_m^2) + (1 + \nu_m)]}, \\ \nu_{TL} = \nu_m V_m + \nu_f V_f, \end{cases} \quad (2)$$

where ν_{LT}, ν_{TL} is the Poisson's ratio for directions along and across the fiber, respectively; ν_m, ν_f is the Poisson's ratio of the matrix and fibers material, respectively.

The boundary state in a particular finite element of the macroproblem is achieved at an unfavourable combination of longitudinal (relative direction of the fibers) σ_{xx} , transverse σ_{yy} and tangent stresses σ_{xy} , which is mathematically determined, in particular, on the basis of the Hofman formula [10]:

$$\left(\frac{\sigma_{xx}}{X_1}\right)^2 - \frac{\sigma_{xx}\sigma_{yy}}{X_1 X_2} + \left(\frac{\sigma_{yy}}{X_2}\right)^2 + \left(\frac{\sigma_{xy}}{S}\right)^2 > 1, \quad (3)$$

where X_1, X_2, S are the constants of material.

In the case that the axis of the orthotropic composite does not coincide with the direction of the power load, the constants in (3) can be calculated as follows:

$$\begin{aligned} X_1 &= X_s \sin^2 \alpha + X_m \cos^2 \alpha; \\ X_2 &= X_m \sin^2 \alpha + X_s \cos^2 \alpha, \end{aligned} \quad (4)$$

where α is the angle between the vector of force application and the direction of the location of fibers, X_m, X_s are the constants of the material, characterizing the boundary state of the material during loading across and along the fibers, respectively.

The result of the finite element solution of the boundary problem of the stress-strained state (SSS) of a particular structure of a composite material of a certain class is a deformation field used in the analysis of meso-state of each element as boundary states. Calculating mesoprob-

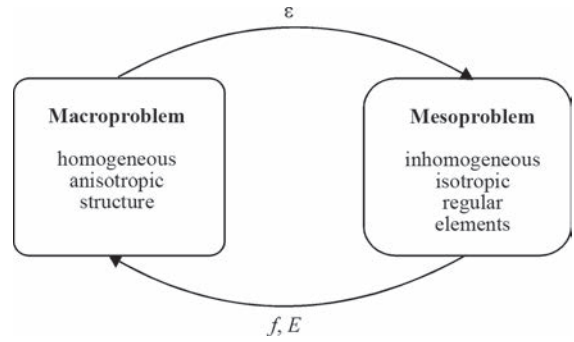


Figure 1. Conditional scheme of statement of multiscale problem of describing stress-strained and damaged state of structures from composite materials for solving typical problems of expertise of technical state

lem, a subcritical damage of the material is evaluated, that affects macroscopic SSS, which is formally taken into account by the transfer of the value of a bulk concentration of damage to the macroproblem.

It is known that the peculiarity of the fracture of composite materials is a significant dispersion of the load limit, which is predetermined by a local heterogeneity of properties, natural deviation of the structure from the ideal, acquired by the damage during manufacture, etc. Therefore, to describe the development of subcritical damage in the matrix of the composite, a statistical approach based on the system of Weibull distribution was used:

$$df = \begin{cases} A f_0 \varepsilon_{\max}^{\eta-1} \exp\left[-\left(\frac{\varepsilon_{\max}}{\varepsilon_0}\right)^\eta\right] d\varepsilon_{\max}, & \varepsilon_{\max} \geq 0; \\ 0, & \varepsilon_{\max} < 0, \end{cases} \quad (5)$$

where df is an increase in volumetric concentration of damage to the matrix of the composite; ε_{\max} is

maximum local deformation; $A = \frac{\eta}{\varepsilon_0^\eta}$, η, ε_0, f_0 are the constants.

In the case if for a particular finite element, the volumetric concentration of damage f exceeds a certain critical value f_{cr} , it was supposed that this element loses its bearing capacity.

Thus, from the mesoscale problem in the macroscale one, the value of the total damage to F is transmitted:

$$F = \frac{\sum f + n_{st}}{N}, \quad (6)$$

where n_{st} is the total number of elements that lost the bearing capacity; N is the number of elements of splitting mesoregion; Σ is the operator of the sum on all finite elements of splitting mesoregion.

This quantitative value F is used to correct the Young modulus in the macroproblem according to the following ratio:

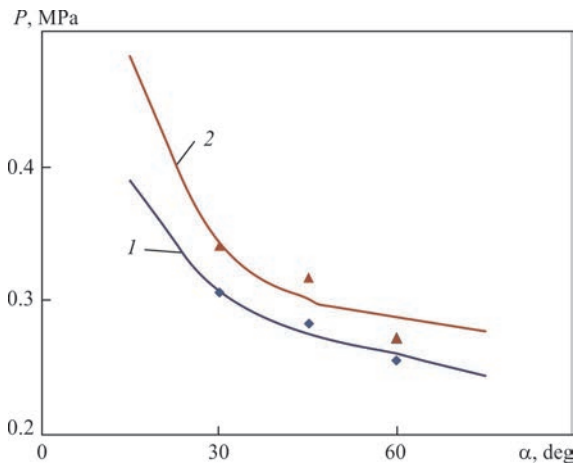


Figure 2. Dependences of fracture stress σ_u of samples of a fiber composite material from an angle of applying force relative to the direction of fibers α as compared to the results of laboratory tests [11]

$$E^f = \frac{E}{1 - F} \quad (7)$$

In addition, initiation and propagation of subcritical damage causes an additional component of the deformation tensor, namely:

$$\varepsilon^f = \Delta F / 3, \quad (8)$$

where ΔF is the increment of F at each step of mechanical load.

Tensors of mechanical stresses σ_{ij} and elastic deformations ε_{ij} are interrelated by the Hooke's law, i.e.:

$$\begin{aligned} \varepsilon_{xx} &= \frac{\sigma_{xx}}{E_x} - \frac{\nu_{xy}}{E_y} \sigma_{yy} + \dots \\ \varepsilon_{yy} &= \frac{1}{E_y} \sigma_{yy} - \frac{\nu_{xy}}{E_x} \sigma_{xx} + \dots; \varepsilon_{xy} = \frac{1}{G_{xy}} \sigma_{xy}. \end{aligned} \quad (9)$$

The proposed algorithm includes a number of constants of the material, which should be determined based on the results of the corresponding laboratory tests. For this purpose, in the work, literary data of experimental studies of the boundary load of fiberglass and carbon fiber composites ($V_m = V_f = 0.5$ for both cases, matrix is epoxy resin) were used with different directions of location of reinforcing fibers. Based on processing of these data, the constants of materials were obtained, namely:

- fiberglass composite: $\eta = 3.2$; $\varepsilon_0 = 0.01$; $f_0 = 10^{-5}$; $X_m = 35$ MPa; $X_s = 350$ MPa; $S = 18$ MPa; $f_{cr} = 0.15$; $E_m = 2$ GPa; $E_f = 70$ MPa;

- carbon fiber composite: $\eta = 4.6$; $\varepsilon_0 = 0.007$; $f_0 = 10^{-5}$; $X_m = 50.2$ MPa; $X_s = 1300$ MPa; $S = 20$ MPa; $f_{cr} = 0.20$; $E_m = 2$ MPa; $E_f = 280$ GPa.

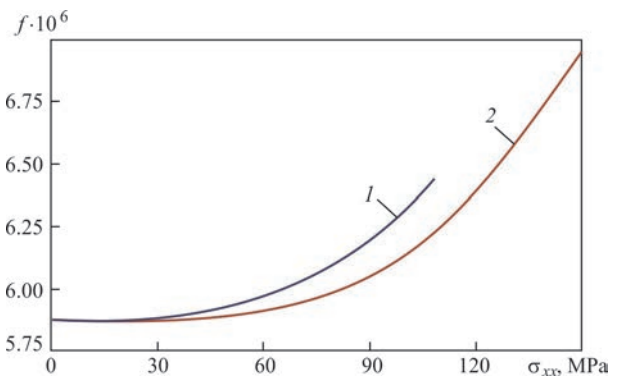


Figure 3. Kinetics of accumulation of bulk concentration f of subcritical damage of composite sample under the action of tensile load σ_{xx} till the boundary state

The calculation was conducted on the basis of a finite element solution of the multiphysical problem in accordance with the abovementioned statement, for macroproblem eight-nodal elements with a linear size of 0.5 mm were used, which sufficiently details a spatially heterogeneous SSS of the material. Detailed software algorithms for solution are given, in particular, in [7].

Figure 2 shows the results of comparing the calculated values of the load limit of samples with experimental results [11]. From these data, it is evident in general the satisfactory accuracy of the results of forecasting the boundary state of the mentioned materials based on the proposed model.

One of the advantages of the developed approach is the possibility of numerical observation of the development of a subcritical damage to individual components of the composite and taking into account the influence of their mesoscale interaction on the boundary state of samples or large-sized structures. Therefore, Figure 3 shows the kinetics of accumulation of a subcritical damage f of the composite samples during loading to the boundary state. Nonlinearity of the development of a bulk concentration of discontinuity in the cross-section as both glass as well as carbon-fiber sample is caused on the one hand, by a gradual weakening of the material and on the other by additional deformation as a result of the appearance and growth of distributed cavities.

An important factor in analyzing the technical state of composite structures is the evaluation of the influence of acquired or long-term operation of damaged material. Within the proposed methodology, the initial damaged state of the material is characterized by a constant f_0 from (5). Figure 4 shows the effect of a particular value f_0 on the value of the boundary load of the sample from the composite material. It is quasilinear, which is predetermined by a relatively small impact of damage to the deformed state at the beginning of the load and elastic deformation. Therefore, the component is additive.

Note. Here and in Figures 3–5: 1 — fiberglass composite; 2 — carbon fiber composite.

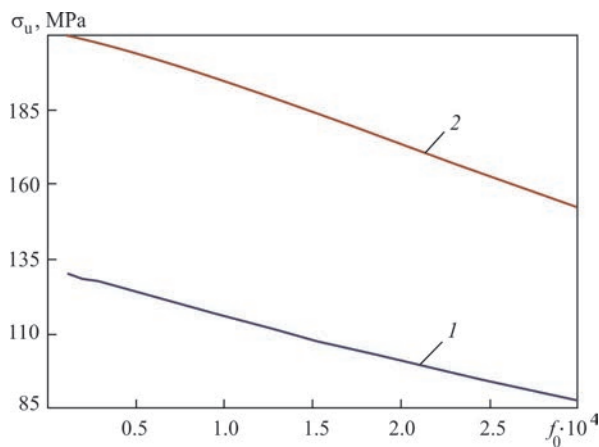


Figure 4. Dependence of ultimate strength σ_u of the fiber composite sample ($V_f = V_m = 0.5$, $\alpha = 45^\circ$) on the initial bulk concentration of subcritical damage to the material f_0

Regarding modeling of the state of large-sized structures, a cylindrical pressure vessel with a diameter $D = 1200$ mm, wall with a thickness $t = 3$ mm under the influence of inner pressure was considered. Here, a characteristic feature is a pronounced biaxility of the stressed state of the structure in the circumferential and axial directions. This does not significantly change the qualitative view of the dependence of the boundary pressure in the structure on the angle of the location of the fibers relative to the pressure vessel axis (Figure 5) as compared to the results of the studies of sample fracture at a one-axial tension (see Figure 2), but changes the corresponding quantitative indices.

CONCLUSIONS

1. A methodology for multiscale forecasting of stress-strained, damaged and boundary states of structures from typical fiber composite materials was developed and software implemented. The proposed approach is based on the finite element realization of monitoring of the state of the structure in general in a homogeneous anisotropic approximation (macroscale) and separately of every regular mesoscale region in a heterogeneous approximation (mesoscale). Comparison of the results of forecasting the boundary state of samples from glass and carbon fiber composites with existing literary data showed a satisfactory accuracy of the developed approach.

2. The peculiarities of the subcritical fracture of the fiber material were investigated at a single load of standard samples. The characteristic nonlinearity of the development of a bulk concentration of discontinuity in the cross-section of a composite sample is shown, which is predetermined by a gradual weakening and additional deformation of the material as a result of arising and growth of distributed cavities. The influence of the initial damaged state of the material on its bearing capacity as an example of applying the developed approach to evaluate the technical state of structures and components from fiber composites was demonstrated.

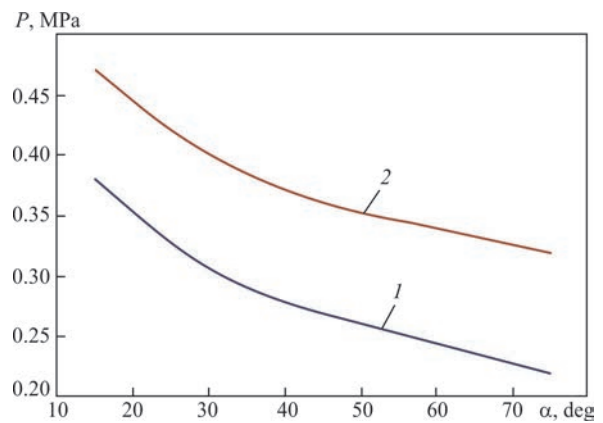


Figure 5. Dependence of ultimate pressure P in a cylindrical vessel (diameter $D = 1200$ mm, wall thickness $t = 3$ mm) from composite material on the angle of fibers α relative to the structure axis

3. The example of a cylindrical pressure vessel shows the peculiarities of the biaxiality of the stressed state to the boundary load of the structure, in particular, when changing the orientation of the fibers relative to its axis, as compared to similar dependencies obtained for standard test samples.

REFERENCES

1. Kiruthika, A.V. (2017) A review on physico-mechanical properties of bast fibre reinforced polymer composites. *J. of Building Engineering*, **9**, 91–99. <https://doi.org/10.1016/j.job.2016.12.003>
2. Yao, S.-S., Jin, F.-L., Rhee, K.Y. et al. (2018) Recent advances in carbon-fiber-reinforced thermoplastic composites: A review. *Composites Pt B: Engineering*, **142**, 241–250. <https://doi.org/10.1016/j.compositesb.2017.12.007>
3. Böer, P., Holliday, L., Kang, T.H.-K. (2013) Independent environmental effects on durability of fiber reinforces polymer wraps in civil applications: A review. *Construction and Building Materials*, **48**, 360–370. <https://doi.org/10.1016/j.conbuildmat.2013.06.077>
4. Kortschot, M.T., Beaumont, P.W.R. (1990) Damage mechanics of composite materials: I — Measurements of damage and strength. *Composites Sci. and Technology*, **39**(4), 289–301. [https://doi.org/10.1016/0266-3538\(90\)90077-1](https://doi.org/10.1016/0266-3538(90)90077-1)
5. Milenin, O.S., Velykoivanenko, O.A., Rosynka G.P., Pivtorak, N.I. (2021) Finite element methods for assessment of the technical condition of large-sized structures from structurally heterogeneous materials (Review). *Tekh. Diagnost. ta Neruiniv. Kontrol*, **2**, 14–19 [in Ukrainian]. <https://doi.org/10.37434/tdnk2021.02.02>
6. Bargmann, S., Klusemann, B., Markmann, J. et al. (2018) Generation of 3D representative volume elements for heterogeneous materials: A review. *Progress in Materials Sci.*, **96**, 322–384. <https://doi.org/10.1016/j.pmatsci.2018.02.003>
7. Velykoivanenko, E.A., Milenin, A.S., Popov, A.V. et al. (2019) Methods of numerical forecasting of the working performance of welded structures on computers of hybrid architecture. *Cybernetics and Systems Analysis*, **55**(1), 117–127. <https://doi.org/10.1007/s10559-019-00117-8>
8. Abdel Ghafaar, M., Mazen, A.A. (2006) Application of the rule of mixtures and Halpin-Tsai equations to woven fabric reinforced epoxy composites. *J. of Engineering Sci.*, **34**(1), 227–236. <https://doi.org/10.21608/jesaun.2006.110251>
9. Buragohain, M.K. (2017) *Micromechanics of a Lamina. Composite Structures. Design, Mechanics, Analysis, Manufacturing, and Testing*. USA CRC Press.
10. Nyambeni, N., Mabuza, B.R. (2018) Considerations of failure analysis in a multi-layered composite structure under ther-

momechanical loading. *Proceedings*, 2(8), 447. <https://doi.org/10.3390/ICEM18-05329>

11. Naresh, K., Shankar, K., Velmurugan, R. (2018) Reliability analysis of tensile strengths using Weibull distribution in glass/epoxy and carbon/epoxy composites. *Composites Pt B: Engineering*, 133, 129–144. <https://doi.org/10.1016/j.compositesb.2017.09.002>

ORCID

O.S. Milenin: 0000-0002-9465-7710

CONFLICT OF INTEREST

The Authors declare no conflict of interest

CORRESPONDING AUTHOR

O.S. Milenin

E.O. Paton Electric Welding Institute of the NASU
11 Kazymyr Malevych Str., 03150, Kyiv, Ukraine
E-mail: asmilenin@ukr.net

SUGGESTED CITATION

O.S. Milenin, O.A. Velykoivanenko, G.P. Rozyuka, N.I. Pivtorak (2021) Multiscale procedure of numerical evaluation of damage and technical state of structures from fiber composite materials. *The Paton Welding J.*, 11, 48–52. <https://doi.org/10.37434/tpwj2021.11.08>

JOURNAL HOME PAGE

<https://pwj.com.ua/en>

Received 13.09.2021

Accepted: 29.11.2021